Christian Carl Weigand

Zinc Oxide Nanostructures and Thin Films Grown by Pulsed Laser Deposition

Thesis for the degree of Philosophiae Doctor

Trondheim, September 2012

Norwegian University of Science and Technology
Faculty of Information Technology, Mathematics and
Electrical Engineering
Department of Electronics and Telecommunications

NTNU – Trondheim
Norwegian University of
Science and Technology

Dedicated to my parents.
For their love and support
throughout my entire life.

In memory of Florian Mumm.

8

Summary

ZnO nanostructures have received great attention during the past decade due to numerous potential applications. In order to enable the fabrication of functional devices, reproducible preparation of such nanostructures is necessary. Therefore, a good understanding of the fundamental processes involved in the formation of ZnO nanostructures is indispensable for improving the controllability of nanostructure growth. This work elucidates various aspects of the essential nucleation and growth mechanisms at work during the growth of ZnO nanostructures by catalyst-assisted pulsed laser deposition (PLD).

ZnO nanowires and triangular nanosheets have been grown on sapphire substrates by Au-assisted PLD. In a first study, the influence of thermal substrate pretreatments on the size and density of the ZnO nanostructures is investigated. It has been found that the presence of surface nucleation sites can compete with nucleation at the Au catalyst and lead to reduced nanostructure sizes and densities. Furthermore, it has been observed that the ZnO morphology switches from nanowires to triangular nanosheets upon increasing oxygen partial pressure in the growth chamber. Electron microscopy results indicates that the catalyst-nanowire growth interface plays an important role in this morphology change. Formation mechanisms of the two different nanostructure types are presented and possible links between oxygen pressure and morphology via growth kinetics and supersaturation considerations are discussed. Additionally, the epitaxial relationships between the two ZnO nanostructure types and sapphire substrates have been investigated in detail by combining x-ray pole figure measurements with both transmission and scanning electron microscope observations. ZnO nanowires growing tilted on c-plane sapphire showed an epitaxial alignment with a buried and inclined substrate plane. Two degenerate configurations have been identified for these tilted wires, promoted by equally low lattice mismatches. On a-plane sapphire, ZnO nanosheets and -wires show distinct differences in the epitaxial relationships with the substrate, indicating a direct correlation to the morphology.

The findings about ZnO nanostructures presented in this thesis help to improve control over catalyst-assisted nanostructure growth techniques and provide a further step towards reproducible nanostructure fabrication.

In a second part of the thesis, the electrical and optical properties of Al-doped ZnO (AZO) thin films grown on GaAs substrates by PLD have been investigated. AZO is a promising candidate for substituting indium tin oxide as transparent electrodes in optoelectronic applications. The aim of the study is to assess the suitability of AZO as a transparent electrode shell around GaAs nanowire solar cells for direct charge carrier pathways. Furthermore, the portability of previously reported results obtained on transparent substrates such as glass or sapphire to the opaque GaAs substrate is discussed.

Preface

This thesis is submitted in partial fulfilment of the requirements for the degree of philosophiae doctor (PhD) at the Norwegian University of Science and Technology (NTNU). The doctoral work has been performed at the Department of Electronics and Telecommunications (IET) from September 2007 to July 2012 with Prof. Helge Weman as main supervisor and co-supervisors Cecile Ladam (SINTEF Materials and Chemistry) and Prof. Jostein Grepstad (IET, NTNU).

Author's contributions

All papers included in this thesis were written by the author. Furthermore, in all papers, the author participated in the nanostructure synthesis, the structural, electrical and chemical characterization as well as data analysis and interpretation. The author carried out all x-ray diffraction pole figure measurements and model calculations in Paper III. The ellipsometry measurements and fitting procedures as well as the acquisition of AFM images in Paper IV were carried out by Ryan Crisp.

During a research stay from January 2009 to June 2009 at the Colorado School of Mines, Golden, Colorado, USA, the author contributed to the following journal article not presented in this thesis:

C. G. Allen, D. J. Baker, T. M. Brenner, C. C. Weigand, J. M. Albin, K. X. Steirer, D. C. Olson, C. Ladam, D. S. Ginley, R. T. Collins, and T. E. Furtak, *Alkyl Surface Treatments of Planar Zinc Oxide in Hybrid Organic/Inorganic Solar Cells*, J. Phys. Chem. C **116**, 8872-8880 (2012)

Acknowledgements

List of Abbreviations

AES   Auger electron spectroscopy

AFM   Atomic force microscopy

AZO   Al-doped zinc oxide

BSE   Back-scattered electrons

CVD   Chemical vapour deposition

DEZn Diethyl zinc

DMZn Dimethyl zinc

EDS   Energy-dispersive spectroscopy

HRTEM High-resolution transmission electron microscopy

ITO   indium tin oxide

LED   Light emitting diode

LS   Liquid-solid

MBE   Molecular beam epitaxy

MOCVD Metal-organic chemical vapour deposition

PEN   The Project on emerging nanotechnologies

PIN   Preferential interface nucleation

PLD   pulsed laser deposition

PVD   Physical vapour deposition

SAED   Selected-area electron diffraction

SEM   Scanning electron microscopy

TEM   Transmission electron microscopy

UV   ultraviolet light

VESTA Visualization of Electronic and STructural Analysis

VLS   Vapour-liquid-solid mechanism

VPT   Vapour-phase transport

VS   Vapour-solid mechanism

VSS   Vapour-solid-solid mechanism

WDS   Wavelength-dispersed spectroscopy

XRD   x-ray diffractometry

ZHNH   Zinc hydroxide nitrate hydrate

Contents

4 The papers   **63**

5 Conclusion and outlook   **99**

Chapter 1

Introduction

Nanostructures have received great attention during the past decades. The number of research publications on some of the most widely studied types of nanostructures, i.e. nanowires and nanorods, has increased from few hundreds in 2001 to more than five thousand in 2011 as shown in Fig. 1.1. One of the reasons for the growing attention are the novel and interesting properties that nanostructures can offer due to the reduction in size, including high surface-to-volume ratios or phenomena based on quantum mechanical effects. Furthermore, nanostructuring can improve the performances of already existing device applications, e.g. by increasing the surface or interface areas while maintaining the same volume [1]. Nanostructures can be fabricated by "top-down" and "bottom-up" approaches, referring to the structuring of bulk material by means of lithographic techniques and self-organized material growth of the desired shape, respectively (cf. section 2.2).

With the critical dimensions and half pitches of todays integrated circuit components, e.g. in central processing units (CPUs), reaching deep into the nanometer-regime, the "top-down" nanostructuring approach is routinely applied in state-of-the-art semiconductor industry [2]. In the "bottom-up" approach, however, novel nanostructure types of both simple and complex morphologies are feasible due to the self-organized growth of the material [3–5]. In order to fabricate these morphologies, a variety of growth techniques can be used, including physical and chemical vapour deposition as well as wet chemical synthesis methods [5–9]. Some of the morphologies made available by "bottom-up" approaches are already used in device applications today, e.g. carbon nanotubes as transparent electrode films on displays, or Ag nanoparticles as antibacterial agents for odor-reduction in clothes [10]. Since its foundation in 2005, the "Project on emerging nanotechnologies" (PEN) registered a significant increase in the number of nanostructure-based consumer products available (cf. Fig. 1.2).

1
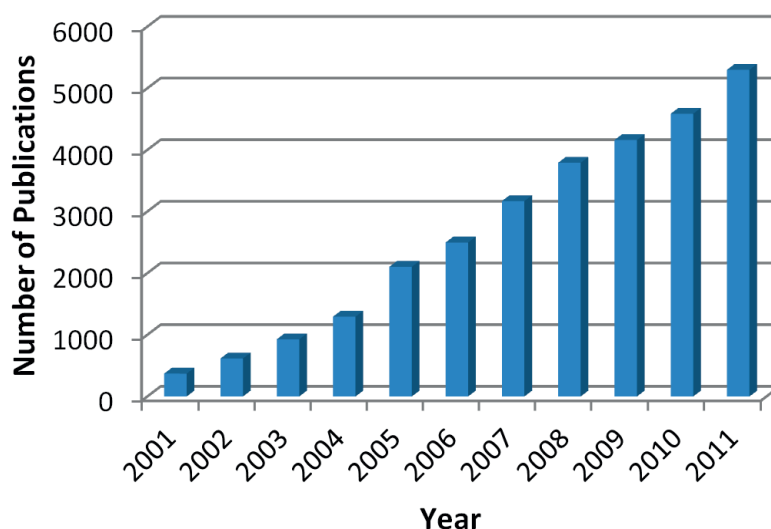
Figure 1.1: Number of scientific papers published on nanowires and nanorods during the last decade. *Source: www.scopus.com, title search with the keywords: "nanowire*" OR "nanorod*".*

Among these are also products based on the light scattering and catalytic effects by ZnO nanoparticles, resulting in products such as sunscreens and self-cleaning coatings, respectively [10]. In fact, white ZnO powder has been used in skin lotions, ointments and other cosmetics products for quite a long time, dating back even beyond the Roman empire [11]. Today, ZnO is not only used in cosmetics, but also paints, tyres, ceramics, plastics and food supplements to name just a few [11, 12]. In its crystalline state, ZnO has a large direct band gap of 3.37eV and a high exciton binding energy of 60 meV at room temperature [13]. ZnO is therefore transparent in the visible wavelength range and a promising candidate for optoelectronic applications such as light emitting diodes (LEDs), transparent electrodes and ultraviolet (UV) lasers [12–14].

While nanostructuring can improve the performances of existing device concepts as mentioned above, the broad spectrum of ZnO nanostructure morphologies that can be fabricated by todays synthesis methods ("bottom-up") offers great potential for novel and unique applications of ZnO, e.g. nanosprings, field emitters, nanocantilevers or nanogenerators that utilize the piezoelectricity of ZnO [5, 15–17]. In section 2.3 of this thesis, a more detailed review on applications, properties and synthesis methods of various ZnO nanostructure morphologies is given. For transferring such novel device concepts based on "bottom-up" nanostructures into market-ready products, reproducible fabrication of the main ingredient, i.e. ZnO nanostructures is vital. In order to achieve

2
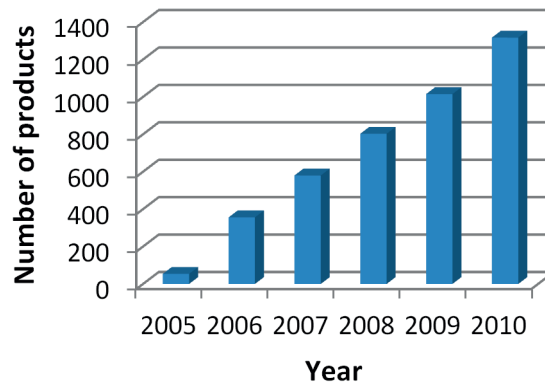
Figure 1.2: Chronical evolution of the number of products based on nanotechnology registered in the *consumer products inventory* of the "Project on Emerging Nanotechnologies" (founded in 2005) [10].

this goal and gain control over morphology, density and orientation of the grown nanostructures, the essential processes of ZnO nanostructure formation need to be understood.

The work presented in this thesis provides insight into the fundamental processes of nanostructures prepared by the "bottom-up" approach. Nucleation and growth processes are investigated for ZnO nanostructures grown by catalyst-assisted pulsed laser deposition (PLD). The influence of substrate surface properties on the catalyst-assisted nucleation of ZnO nanostructures is revealed and a method to improve control over the nanostructure density via substrate pretreatment is presented. Moreover, the growth mechanisms of ZnO nanowires and nanosheets are explained in detail and the role of oxygen for determining the final nanostructure morphology is discussed on the basis of growth kinetics. Additionally, the epitaxial relationships of ZnO nanowires and nanosheets with widely-used sapphire substrates are revealed by x-ray diffractometry (XRD) and the driving forces for the observed nanostructure growth orientations are examined.

As a second aspect, the electrical and optical properties of Al-doped ZnO (AZO) thin films on opaque GaAs substrates have been investigated in this thesis. When doped with Al or Ga, ZnO is highly conductive while retaining its transparency in the visible wavelength range [18]. This renders doped ZnO a potential alternative to indium tin oxide (ITO) in device applications requiring a transparent electrode such as thin film solar cells or flat-panel displays [18, 19]. For future devices based on nanowires such as GaAs nanowire solar cells, transparent electrodes could even be applied directly as a doped ZnO shell around the GaAs nanowire core. This might lead to reduced path lengths of free charge carriers created within the active GaAs nanowire core and therewith improve
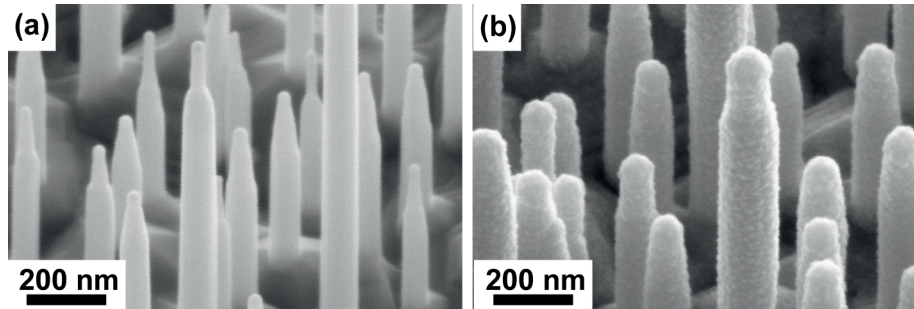
Figure 1.3: Scanning electron microscopy (SEM) images of GaAs nanowires grown by Au-assisted molecular beam epitaxy (a) and the same GaAs nanowires with a PLD-grown Al-doped ZnO shell. Samples grown in Prof. Helge Weman's group at NTNU.

collection efficiencies. The study presented in this thesis serves as preliminary work to assess the suitability of AZO shells as transparent electrodes on GaAs nanowire solar cell devices. First AZO shells have already been prepared around GaAs nanowires as shown in Fig. 1.3 and electrical contacts to single GaAs/AZO core-shell structures have been successfully realized. However, this topic is not included in the present thesis due to the incompleteness of the available experimental data at this preliminary stage of the project.

The present thesis is structured in the following manner: In the first part, a brief introduction to the material system ZnO and its doping mechanisms is given. Subsequently, some fundamental aspects of nucleation and growth are presented, followed by an overview over the most commonly employed "bottom-up" growth mechanisms of nanostructures. Chapter 2 concludes by reviewing the properties, synthesis techniques and applications of selected ZnO nanostructures. In chapter 3, the experimental methods used to synthesize and characterize the ZnO nanostructures and thin films presented here are briefly explained. The published papers and manuscripts prepared in the course of this thesis are reprinted in Chapter 4, followed by a summary and future outlook of the work in Chapter 5.

Chapter 2

Material system

In this section, the fundamental physical properties of the ZnO material system employed in this work are introduced. It provides some theoretical background on the microscopic processes involved during nanostructure and thin film growth. Furthermore, a brief overview is presented over different growth mechanisms utilized for the fabrication of ZnO nanostructures. In the last part of this section, selected ZnO nanostructure morphologies and various approaches to their synthesis are discussed in detail.

2.1 ZnO crystal structure

ZnO can adapt three different types of crystal structures, i.e. rocksalt, zinc blende and wurtzite-type phases. The rocksalt and zinc blende structures can only be stabilized at high pressures or by growth on appropriate cubic substrates, respectively [12, 20]. Therefore, the wurtzite crystal structure represents the most commonly observed phase in ZnO thin films and nanostructures. A schematic illustration of the ZnO wurtzite crystal structure is given in Fig. 2.1a. It can be described by a hexagonal Bravais lattice with constants $a = b = 3.2494$ Å and $c = 5.2038$ Å [21]. While the lattice vector c is perpendicular to both a and b, the latter two vectors include an angle of $\gamma = 120°$. Each atom of the element A (zinc or oxygen) in the crystal is surrounded by four tetrahedrally coordinated atoms of the other element B (oxygen or zinc, respectively).

It should be noted that in hexagonal systems, the crystallographic planes and directions are often given as four-digit miller indices (h k i l). Examples of the most common low-index lattice planes and vectors are illustrated in Fig. 2.1b. This four-digit system is over-determined and for the description of lattice planes, the index i can be calculated
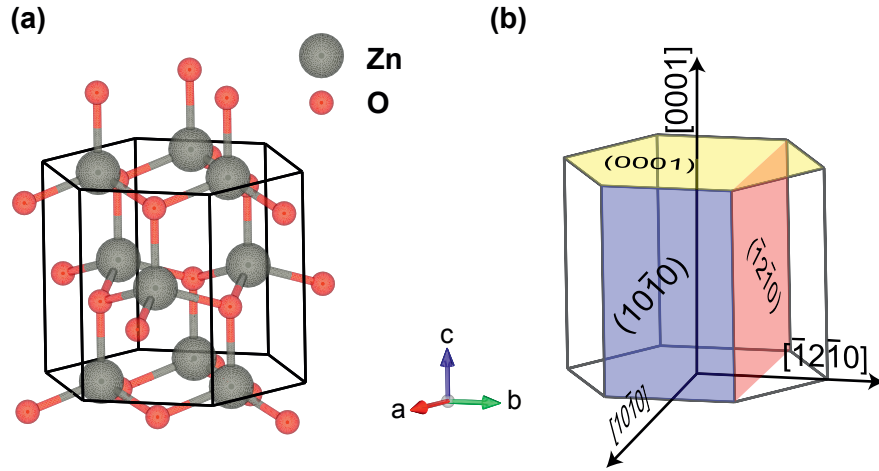
Figure 2.1: Schematic illustration of (a) the ZnO wurtzite crystal structure (created using the VESTA software [22]) and (b) the most common low-index lattice planes and vectors.

Table 2.1: Surface energy values calculated by first principles methods using the local-density approximation [26]

Crystal planes	Surface energy (J/m^2)
$(10\bar{1}0)$	2.3
$(11\bar{2}0)$	2.5
$(0001)/(000\bar{1})$	4.3

from the common three-digit system (h k l) via $i = -(h + k)$ [23].

Due to the positions of the zinc and oxygen ions in the ZnO unit cell and the asymmetry of the hexagonal lattice around the unit cell center, the wurtzite phase of ZnO exhibits a finite dipole moment along the hexagonal c-axis. ZnO is thus a piezoelectric material with potential device applications as actuators, sensors, piezotronics or nano-generators [16, 24]. Due to this dipole moment the ZnO {0001} surfaces become "polar surfaces" and according to Tasker's rule [25] should be unstable. Nevertheless, the observation of ZnO {0001} surfaces is nothing unusual in ZnO thin film and nanostructure growth. In general, the stabilization of such polar surfaces can occur via various mechanisms, e.g. surface reconstruction, adsorption of charged atoms/molecules or internal charge transfer [26–29]. The exact mechanisms involved for the stabilization of ZnO {0001} faces are still controversial and combinations of different mechanisms such as surface reconstruction and hydrogen adsorption have been suggested [30].

Furthermore, caused by this dipole moment, the ZnO{0001} planes have the highest surface energy of all low-index planes of the wurtzite ZnO crystal as shown by ab-initio calculations [26]. The corresponding values are summarized in Table 2.1. Surface energies play an important role in the nucleation and growth processes as will be discussed later in this chapter. They have key influence on the diffusion and adsorption rates of material on a crystal facet. As the facet with the highest surface energy, the ZnO(0001) plane is typically the surface with the highest growth rate during ZnO deposition [31]. However, Wang et al. observed distinct differences in the chemical activity and growth rates of the different terminations of the ZnO{0001} surfaces. While the Zn-terminated (0001) surface showed high growth rates, the O-terminated (000$\bar{1}$) facet was nearly chemically inert [15].

2.1.1 Doped ZnO

In this subsection, a brief introduction is given to the most common ways of doping in ZnO, providing fundamental background for the understanding of paper IV. For a more comprehensive discussion of this topic, the reader is referred to corresponding reviews in the literature [18,19]. Even without any type of doping, ZnO shows intrinsic n-type conductivity, i.e. excess electrons act as majority charge carriers, transporting electric currents through the crystal lattice. This phenomenon is attributed to the presence of native defects such as oxygen vacancies and Zn interstitials in the ZnO crystal lattice [18,32,33]. However, the exact origin of this n-type conductivity, i.e. the exact species of electron donors, are yet to be identified. Ab-initio calculations as well as electron paramagnetic resonance experiments indicate that oxygen vacancies are deep level rather than shallow donors and have high formation energies [33–35]. Furthermore, first-principles investigations deduce instability of Zn interstitials from the high formation energies calculated and the low migration barriers enabling fast diffusion [36]. Even though other possible explanations have been advanced, including intrinsic impurity-doping by hydrogen, the exact donor species responsible for n-type conductivity in intrinsic ZnO is still controversial [18].

Due its large band gap, ZnO is a potential candidate for use as transparent electrodes in optoelectronic applications [18, 19]. The resistivity of intrinsic ZnO thin films, however, is typically on the order of 10^{-2} Ωcm and are therefore too high for the use as transparent electrodes [37, 38]. In order to increase its n-type conductivity, ZnO can be doped with various group V elements acting as electron donors, e.g. B [39, 40], Al [41–43], Ga [40, 44] and In [45, 46] as well as elements from other groups, including F [47]. Among these, the most frequently employed dopants are In, Al and Ga. Resistivities on the order of 10^{-4} Ωcm have been achieved with Al- or Ga-doped ZnO thin films [40, 48, 49], which are comparable to the electrical properties of indium tin oxide

(ITO) layers - the standard material used for transparent electrodes in device applications today [19]. Alternatives to ITO - such as ZnO - are highly desirable due to the scarceness and high costs of indium [19].

In general, the resistivity ρ of a material with electrons as majority charge carriers is given by the relation $\rho = 1/(ne\mu)$. Here, n is the carrier concentration, e the elemental charge and μ the mobility of electrons in the solid. Hence, the resistivity can be reduced by increasing the carrier concentration and/or electron mobility in the material. Thereby, the concentration n of charge carriers is mainly determined by the concentration of active electron donors (dopants), whereas the mobility μ of electrons is constrained by scattering events during charge transport. Such scattering can occur at different sites in a crystal lattice, for example at grain boundaries, impurities or phonons [50, 51]. Typically, scattering at grain boundaries as well as ionized impurities are considered as the dominant mechanisms in transparent conducting ZnO thin films [52–54]. However, scattering at intragrain clusters or additional phases present in the films have also been discussed as important scattering mechanisms limiting the electron mobility in doped ZnO thin films [51, 55].

For the case of the most commonly employed n-type dopants Al and Ga, doping is generally believed to occur via the incorporation of dopant atoms at substitutional Zn sites, i.e. a Zn atom is replaced by a Ga or Al atom [56–58]. Thereby, the dopant atom releases one of its electrons into the conduction band, essentially increasing the concentration of charge carriers. Those dopant atoms located elsewhere in the crystal lattice, e.g. at interstitial sites, are considered inactive and do not contribute to increased conductivity. Besides this doping mechanism, it is often believed that native defects such as oxygen vacancies and Zn interstitials contribute to the electrical conductivity also in doped ZnO films [48–50]. The introductory arguments on the role of native defects for intrinsic n-type conductivity, however, are also valid for the case of doped ZnO.

As described above, n-type conductivity in ZnO is easily achieved - even without any intentional, extrinsic doping. The reproducible preparation of p-type conductivity in ZnO, however, is not straight-forward [18, 59]. In the past decade, various approaches have been pursued utilizing group V elements such as P [60, 61], As [62, 63] and nitrogen [64–66] as well as group I elements including Li [67] and Na [68]. The issues with achieving p-type doping in ZnO can be manyfold, including high activation energies of many potential dopants as well as precipitate formation and low solubilities [59, 69–71]. One of the major problems is the compensation of p-type dopants by defects such as oxygen vacancies or impurities [18, 33, 72], which can result in conductivity inversion back to n-type behaviour after some days [66]. Long-term stability of the p-type conductivity is therefore a major issue which needs to be overcome before commercial use of

ZnO homojunctions in optoelectronic device applications such as LEDs can be realized.

2.2   Synthesis of nanostructures

The prefix "nano" describes structures with at least one dimension on the order of 10^{-9} m, i.e. in the nanoscale. These structures can be classified by the number of dimensions *exceeding* the nanoscale. One-dimensional nanostructures, for example, are elongated in a single direction, i.e. exceed the nanoscale only along one axis, whereas two-dimensional nanostructures exhibit only one dimension in the nanoscale, thus exceeding it along the two other dimensions. The term zero-dimensional nanostructures refers to quantum dots with all dimensions on the order of 10^{-9} m.

In this section, the basic concepts for the fabrication of nanostructures are presented. In general, all nanostructure fabrication methods can be classified in two main categories, namely the "top-down" and "bottom-up" approaches. The "top-down" method describes all fabrication processes in which a layer of the desired nanostructure material already exists either as bulk or as a thin film deposited on a substrate. During the fabrication process, the layer material is "machined" into the desired shape via various techniques including photo- and electron beam lithography in conjunction with wet chemical or reactive ion etching processes. These techniques are similar to the methods employed in the semiconductor industry for patterning thin material layers into market-ready devices. Nanostructures fabricated by the "top-down" approach can be deliberately positioned on the substrate with high accuracy, limited mainly by the resolution of the patterning lithography technique. However, the preparation of nanostructures by lithography can be time-consuming, especially if high resolution morphologies are required and electron beam lithography techniques need to be utilized which only allow for serial pattern writing compared to the parallel processing of entire wafers with lower-resolution photolithography methods. Additionally, top-down fabricated nanostructures may suffer from crystal defects, impurities and/or contamination due to the chemistries or ion interactions of the processes involved.

The second category "bottom-up" includes all methods in which the nanostructure grows or self-assembles on a suitable substrate by utilizing thermodynamic processes and/or properties of the involved materials. The employed techniques often consist of one or several different material sources (e.g. one for each element of the desired compound, or precursors that need to undergo a chemical reaction in order to "free" the desired nanostructure material), a container that allows for the intermixing of the different sources

(e.g. vacuum chamber, beaker with chemical solution) and a heat supply (e.g. heated substrate mount or a hot plate). In general, the formation of nanostructures hereby proceeds in gaseous or liquid media with source materials supplied in solid, liquid or gaseous phases. If processed under optimum conditions, the "bottom-up" techniques typically allow for very high crystal qualities of the grown nanostructures since it nucleates and grows as a single crystal from the substrate. Accurate positioning of the nanostructures on a substrate, however, is often feasible only via additional efforts such as patterning of a nucleation or catalyst layer prior to the actual nanostructure fabrication or the use of suitable templates [73–76].

2.2.1 Fundamental aspects of crystal growth

In general, the deposition and growth of thin films and nanostructures proceeds by several consecutive steps. In the first step, the growth species adsorb on the substrate surface via forming weak bonds due to oscillating (van-der-Waals) or permanent dipole moments. This weak bonding state is referred to as *physisorption* [77]. Due to the weak interaction forces, the potential well, in which the physisorbed molecules are trapped, is shallow and the low energy barriers at the walls of the well can allow growth species with sufficient energy to escape and "hop" to adjacent sites (wells). The physisorbed molecule at the surface therefore retains some mobility and can move finite distances on the substrate via *surface diffusion* (step two). The mobile molecule can now either desorb (e.g. re-evaporate) from the surface or - and this is the third step - form chemical bonds with the substrate or the growing film/nanostructure, a process referred to as *chemisorption*. In step four, adsorbed growth species accumulate and initiate film/nanostructure growth by *nucleation*. Subsequently, the formed nucleus grows in size and in the case of thin film deposition coalesces with nearby nuclei to form a layer. For nanostructure growth, however, the nucleus expands by uni-directional growth which can be imposed by different mechanisms as discussed in section 2.2.2.

The fundamental nucleation and growth processes described in the following subsections are based on the discussions in the book by Smith [77]. For a more detailed discussion, the reader is referred to this or other books on thin film deposition such as the works by Adams or Markov [78, 79].

Surface diffusion

The mobility of growth species adsorbed on the substrate surface is very important in thin film and nanostructure growth [77]. Via surface diffusion, adsorbed molecules can reach

10
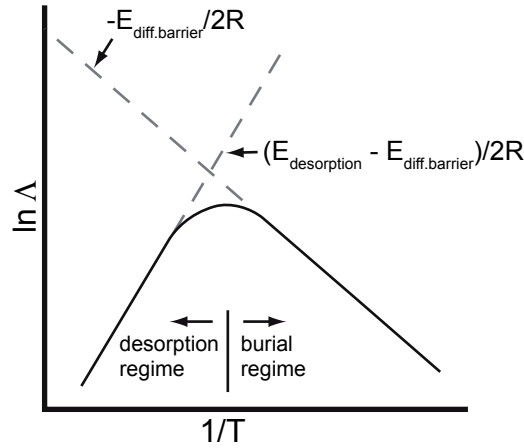
Figure 2.2: Qualitative Arrhenius plot of the diffusion length Λ vs. temperature (energy) of the growth species. When the temperature is above the energy threshold for desorption $E_{desorption}$, Λ is limited by re-evaporation (desorption regime). In the burial regime, the diffusion length is constrained by the impinging material flux burying the diffusing atoms during growth. $E_{diff.barrier}$ denotes the energy barrier for surface diffusion and R is the universal gas constant. *Adapted from [77].*

the nanostructure growth fronts/interfaces and find low-energy active sites that facilitate chemisorption. Surface diffusion can therefore significantly influence the crystallinity and morphology of the grown thin films and nanostructures. The distance an adsorbed molecule can travel on the substrate surface is the "diffusion length Λ". Its value is significantly different (up to several orders of magnitude) for chemisorbed and physisorbed molecules due to the different strengths in attractive forces and the corresponding depths of the potential wells. Furthermore, the energy barriers $E_{diff.barrier}$ the diffusing adsorbate needs to overcome also depend on the surface energy of the crystal facet the species travels along. In general, the diffusion length increases with rising growth temperature or, more precisely, with the energy of the adsorbate, since energy barriers for diffusion are more easily overcome. If the diffusion length becomes sufficiently high, the majority of adsorbates can find a low-energy site and chemisorb, thus resulting in crystalline nanostructure or thin film growth. However, as the energy of the adsorbate increases further, more and more diffusing growth species will be lost by desorption from the substrate surface before incorporation in the growing structure. Thus, the diffusion length shortens with increasing growth temperature as soon as the adsorbate energy increases above the activation level of desorption $E_{desorption}$. This corresponds to the desorption-limited regime of the diffusion length Λ as illustrated qualitatively in Fig. 2.2. Hence, the optimum growth conditions allowing for maximum surface diffusion there-

11
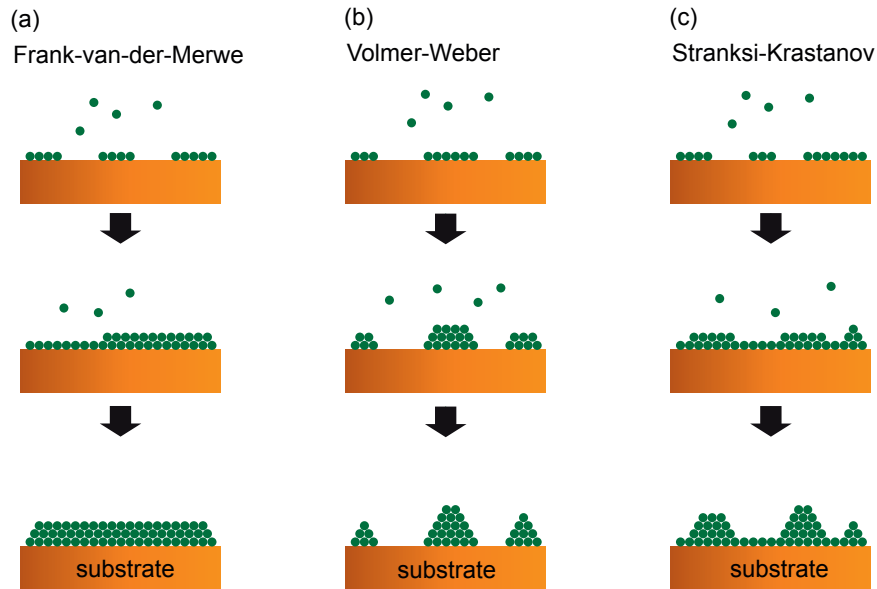
Figure 2.3: Schematic illustration of the three different growth modes Frank-van-der-Merwe or layer-by-layer growth (a), Volmer-Weber or island growth (b) and Stranski-Krastanov (c).

fore involve substrate temperatures just below the critical value for desorption. On the other hand, the diffusion length can also be limited by high fluxes of impinging growth species, essentially burying diffusing adsorbates by the next layer of deposited material. In Fig. 2.2, this is denoted as the burial regime. The buried molecules still contribute to the growth of the structure, but are likely to be incorporated as defects, thus resulting in reduced crystallinity of the final product. A more detailed discussion with derivations of the mentioned dependences of surface diffusion can be found in chapter 5 of the book by Smith [77].

Nucleation

After the adsorption of growth species on the substrate surface, crystal growth can proceed in different ways depending on the surface energies of the substrate γ_{sub} and the growing crystal γ_c as well as the interface energy between the two, γ_i. In general, three growth modes are identified [80] which are shown schematically in Fig. 2.3. In the first case, the sum of surface and interface energies of the growing crystal is lower than the substrate surface energy $\gamma_c + \gamma_i \leq \gamma_{sub}$. Correspondingly, minimization of surface energy drives the deposited material to cover or "wet" the substrate surface completely, thus

12

resulting in layer-by-layer or Frank-van der Merwe growth illustrated in Fig. 2.3a. In the opposite case, i.e. the surface energy of the substrate is the lowest with $\gamma_c + \gamma_i \geq \gamma_{sub}$, the total energy of the system is minimized by agglomeration of deposited species and subsequent nucleation of three-dimensional islands as schematically shown in Fig. 2.3b. This is the Volmer-Weber growth mode. In the third case, island formation begins not before one or few monolayers of deposited material cover the substrate surface (cf. Fig. 2.3c). This growth mode is induced by stress due to lattice mismatch between substrate and growth material and is referred to as Stranski-Krastanov growth.

The surface energies involved in the growth process therefore play an important role in determining, whether growth occurs in a two-dimensional layer mode or by the formation of three-dimensional islands. Nanostructure growth often proceeds by the three-dimensional growth mode [81–83]. In the following paragraph, the discussion therefore focuses primarily on this type of nucleation.

In the three-dimensional growth mode, impinging and diffusing atoms accumulate and initiate crystal growth by the formation of a nucleus. The driving force for such nucleation and growth of a crystal is the so-called *supersaturation*. This term refers to the chemical potential difference between the supply phase and the condensed phase $\mu_s - \mu_c$. For growth from a vapour phase source, it can also be written as the ratio of the total pressure p to the equilibrium vapour pressure p_v [77]:

$$\Delta\mu = \mu_v - \mu_c = RT \ln \frac{p}{p_v} \tag{2.1}$$

When a nucleus forms, it gains in volume V and simultaneously in surface area A_c of surface energy γ_c. Since such creation of surface area requires energy, there is another driving force counteracting the supersaturation and, hence, nucleus formation. The corresponding change in Gibbs free energy per nucleus is therefore a balance between supersaturation and surface energy. Under the simplifying assumptions of a homogeneous substrate surface (i.e. the absence of active nucleation sites), negligible wetting of the substrate (three-dimensional island growth mode) and sufficient surface diffusion to ensure equilibrium, this free energy change can be written as

$$\Delta G = -(\mu_v - \mu_c)V/V_{mc} + \gamma_c A_c \tag{2.2}$$

where V_{mc} is the molar volume of the condensate. If a spherical shape of the nucleus is considered, equation 2.2 becomes

$$\Delta G = -RT \ln\left(\frac{p}{p_v}\right)\frac{(4/3)\pi r^3}{V_{mc}} + \gamma_c 4\pi r^2 \tag{2.3}$$

If ΔG for a given radius r of the nucleus is positive, nucleation is suppressed since the spontaneous dissociation of the nucleus is energetically more favourable than its growth. For negative values of ΔG, on the other hand, the nucleus is stable and continues to grow due to the reduction in Gibbs free energy with increasing size. Following equation 2.3 $\Delta G(r)$ reaches its maximum at a critical nucleus size r^* above which the nucleus becomes stable:

$$r^* = r(d(\Delta G)/dr = 0) = \frac{2\gamma_f}{\frac{RT}{V_{mc}}\ln\left(\frac{p}{p_v}\right)} \tag{2.4}$$

The corresponding change in Gibbs free energy at r^* is then given as

$$\Delta G^* = \frac{(16/3)\pi\gamma_f^3}{\left[\frac{RT}{V_{mc}}\ln\left(\frac{p}{p_v}\right)\right]^2} \tag{2.5}$$

and is often referred to as the *energy barrier for nucleation*. It can be seen from equations 2.4 and 2.5 that the critical nucleus size and the energy barrier for nucleation depend on the supersaturation ratio $ln(p/p_v)$ and the substrate temperature. While for high ratios p/p_v, stable nuclei of small radii can be readily formed because of a low energy barrier, many growth species need to agglomerate in order to stabilize a nucleus at low supersaturation ratios. Furthermore, both the critical radius and the energy barrier for nucleation decrease with rising substrate temperature.

It should be noted that in the previous discussion of nucleation, the effect of active nucleation sites has been neglected. In reality, however, such active sites are present on the substrate in most cases and will facilitate nucleation by lowering the corresponding energy barrier. Furthermore, it has been assumed that there is no interaction between the substrate and the growing crystal, i.e. $\gamma_i = \gamma_c$. For deposition on a substrate, however, such interaction cannot be neglected and in many cases $\gamma_i < \gamma_c$, essentially reducing the surface energy term in equation 2.2 and lowering the energy barrier for nucleation. Moreover, γ_c has been considered constant for all nucleus sizes. Due to increased curvature, however, the number of dangling bonds at the surface of small nuclei is higher than at surfaces of large ones. Accordingly, γ_c for small nuclei will be larger than the surface energy of a bulk single crystal and will approach the latter value as the nucleus size increases.

In the case of two-dimensional nucleation (layer-by-layer growth), the wetting of the substrate is complete, i.e. the energy sum of the growing crystal surface and the interface between the substrate and the nucleus $\gamma_c + \gamma_i$ are lower than the surface energy of the substrate γ_{sub}. The system therefore gains in energy as the coverage of the substrate surface increases. However, edges with high numbers of dangling bonds and, thus, high energy are created during the formation of a two-dimensional nucleus on a homogeneous substrate. Therefore, an energy barrier for nucleation and a critical nucleus size exist also in the case of two-dimensional film growth and both parameters depend on super-saturation [77]. Once a stable nucleus is formed, it grows until it coalesces with other 2D nuclei and a full monolayer is completed. Also in this case, the presence of active nucleation sites on the substrate, such as steps of atomic terraces or surface defects, will aid the nucleation and growth of the thin film due to a reduced energy barrier for nucleation. For a more detailed description of 2D nucleation the reader is referred to the book by Smith [77].

To conclude this section, it should be noted that for the above discussion of nucleation, it has been assumed that the system is in equilibrium, i.e. surface diffusion is sufficiently high and adatom desorption is low, therewith the "reaction time" for finding and forming a nucleus is ensured. In some cases, however, the nucleation or growth processes might be limited by the speed of the reactions or processes involved rather than the balance of free energies. Such growth is often referred to as "kinetically inhibited" and occurs, for example, when surface diffusion is suppressed by high deposition fluxes or low growth temperatures with growth species chemisorbing instantly upon impinging on the substrate. Whether or not a growth process is dominated by kinetics strongly depends on the chosen growth conditions during deposition.

2.2.2 Nanostructure growth mechanisms

In this section, various mechanisms for the growth of nanostructures with and without the use of catalysts are presented for precursor and material sources of different phases. The first subsections deal with catalyst-assisted growth mechanisms including the vapour-liquid-solid (VLS) and vapour-solid-solid (VSS) mechanisms. The major difference between these two mechanisms is the phase of the catalyst particle during growth (i.e. liquid or solid). Subsequently, the preferential interface nucleation mechanism is described, which attempts to give a more generalized description of all catalyst-assisted growth mechanisms, including VLS and VSS. In the last part of the section, catalyst-free approaches to the formation of nanostructures are discussed, mainly focusing on the vapour-solid (VS) mechanism since the growth technique employed in this work employs a vapour phase source. Finally, solution- and template-based growth mechanisms
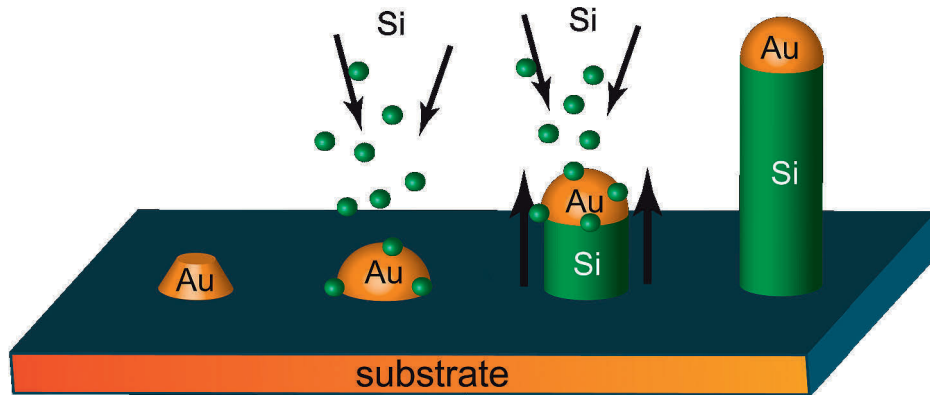
Figure 2.4: Schematic illustration of the vapour-liquid-solid (VLS) mechanism for a Au-assisted Si nanowire. *Adapted from [92].*

are briefly presented.

The Vapour-Liquid-Solid (VLS) mechanism

This mechanism was first described by Wagner and Ellis in 1964 for the fabrication of Si whiskers with diameters of several hundred nanometers to a few micrometers and with a Au catalyst guiding the whisker growth [84]. Since then it has been applied to various material systems with diameters as thin as a few nanometers [85–88]. Especially during the last decade, this mechanism has received great attention and is one of the most widely employed mechanisms for semiconductor nanostructure growth. Its relevance has been expanded from growth of elemental whiskers by a Au catalyst to the fabrication of compound and oxide semiconductor nanostructures using a wide variety of catalyst metals [89–91].

A schematic illustration of the basic VLS mechanism for growth of an elemental Si whisker or nanowire is shown in Fig. 2.4 with Au as a catalyst metal. In the initial stage of VLS growth, catalyst metal is deposited on the substrate in the form of a thin layer or colloidal particles. It is then heated to sufficiently high temperatures and the metal layer or particles begin to alloy with the substrate material and form droplets. When the temperature reaches a value above the metal-substrate eutectic point, the particles become liquid due to a significant reduction in melting point at the eutectic composition. The vapour phase source material (**VLS**) is then streamed into the reactor and the cata-

16

lyst droplet acts like a "sink", collecting the growth species impinging on the substrate. These enter the metal-substrate alloy droplet and adapt the liquid phase (V**L**S). With time, the concentration of source material in the droplet rises beyond its solubility limit and the catalyst particle becomes supersaturated. As a consequence, the material starts to precipitate beneath the metal catalyst particle, nucleating the whisker or nanowire in the solid phase (VL**S**). With continuous supply of source vapour, the metal catalyst particle is raised as the growing structure underneath it gains in length. Under ideal VLS growth conditions, the diameter of the grown structure corresponds to the size of the metal catalyst droplets and the structures' length is directly proportional to the deposition duration. Non-ideal conditions, however, might lead to, for example, diffusion of the catalyst metal away from the nanostructure tip or additional material deposition on the whisker sidewalls, resulting in short nanostructures due to early growth termination or tapered, needle-like morphologies, respectively [93, 94].

The Vapour-Solid-Solid (VSS) mechanism

In the VLS mechanism, the catalyst droplet is assumed to be in the liquid state due to its reduced melting point at the eutectic composition. However, it has been reported for different material systems - including ZnO - that nanostructures can also be grown by the same method, even if the growth temperature is below the critical eutectic value [87, 95–98]. In this case, the phase of the alloy droplet is solid and the growth mechanism is therefore termed V**SS**. Kodambaka et al. have been able to show by in-situ transmission electron microscopy (TEM) imaging of Ge nanowire formation that growth by the VSS mechanism proceeds significantly slower (by about 10 - 100 times) than growth from a liquid catalyst droplet (VLS) [99]. Furthermore, due to the solid phase of the catalyst, growth species now reach the growth front via diffusion along the catalyst surface rather than the bulk particle [100].

Preferential interface nucleation (PIN)

Inspired by the idea to find a single growth mechanism that is able to explain all catalyst-assisted nanostructure growth, regardless of the phases of material source and catalyst involved, Wacaser et al. proposed a more general scheme for the formation of nanostructures from a catalyst particle [101]. Therein, the formation of a nanostructure is considered independent of the phase diagram or the eutectic temperatures of the involved materials and proceeds only by nucleation at one of the interfaces between the catalyst droplet and the growing nanostructure, i.e. the catalyst-nanostructure interface or the triple-phase boundary (cf. Fig. 2.5). Once a nucleus is formed, it grows in the
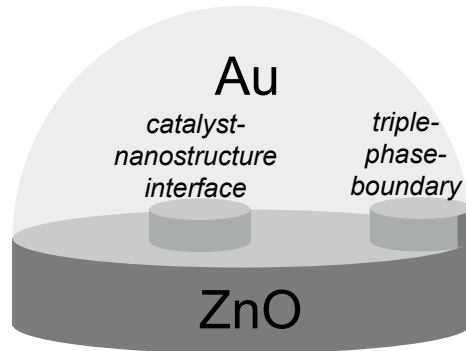
Figure 2.5: Schematic illustration of the nuclei initiated by preferred nucleation at the catalyst(Au)-nanostructure(ZnO) interface and triple-phase-boundary as described in the PIN mechanism [101].

lateral directions via step propagation until a full monolayer is completed at the catalyst-nanostructure interface. When the next nucleus forms at the interface, the growth cycle is repeated until the deposition flux is terminated. The step propagation mechanism is also referred to as "ledge-flow" mechanism and has been observed experimentally by *in-situ* TEM imaging of Ge and Si nanowire growths from solid Pd and Au catalyst particles [98, 102]. Even though the same mechanism is assumed also for liquid catalyst droplets, it proceeds too fast to be detectable by *in-situ* TEM [103]. Contrary to the classic VLS mechanism, the PIN approach takes into account both the supersaturation *inside* and *outside* (i.e. the supply phase) the liquid catalyst droplet

The benefits from catalyst-assisted growth mechanisms include good control over the nanostructure dimensions, since the diameter of a grown nanowire is directly correlated with the size of the metal catalyst particle. Furthermore, if additional processes such as lithography steps are employed, the position and densities of the catalyst - and therewith the nanostructures - can be controlled, allowing for the preparation of ordered nano-structure arrays [74, 104]. However, if not removed by additional processing steps, the metal catalyst particle resides at the nanostructure tips also after the growth. Moreover, diffusion and incorporation of the catalyst metal atoms into the growing nanostructure have been reported [105], possibly impose impurity and therewith performance issues in potential device applications. In order to avoid these problems, recent research efforts have been directed towards self-catalyzed nanostructure growth in which one element of the compound semiconductor nanostructure is utilized as a catalyst particle instead of a foreign metal [106, 107]. The reported dimensions and crystal properties of the self-catalyzed nanostructures are comparable to the ones fabricated from a metal cata-lyst, rendering self-catalysis a promising candidate for well-controlled and impurity-free
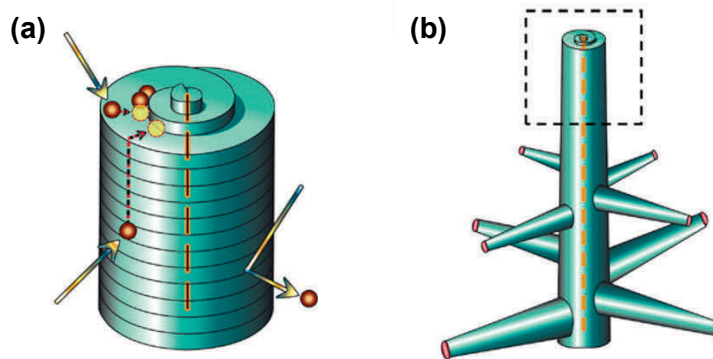
Figure 2.6: Schematic illustration of the preferential growth at a screw dislocation (a) resulting in the formation of a uni-axial nanowire stem for a hierarchical nanostructure (b). *Adapted with permission from [108]. Copyright 2008 American Association for the Advancement of Science.*

nanostructure growth.

The Vapour-Solid (VS) mechanism

In the catalyst-assisted mechanisms described above, the one-dimensionality of the nanostructure was introduced via the preferential precipitation/nucleation beneath a catalyst particle, which guided the growth in a single direction. If the growth was carried out under identical growth conditions but without the use of a catalyst (VS growth), in many cases the deposited species would agglomerate into two-dimensional islands and subsequently coalesce to form a thin film rather than a nanostructure. However, under optimized growth conditions, many materials exhibit intrinsic differences in the growth rates of the crystal planes, i.e. the crystal grows the fastest along a single crystal direction compared to other directions. In these cases, uni-directional growth can indeed be achieved by direct condensation of the vapour phase source material (**VS**) on a substrate. The (0001) plane of the ZnO wurtzite crystal, for example, is the facet with the highest surface energy and therefore the highest growth rate of all low-index planes as mentioned above. Thus, the fabrication of one-dimensional nanostructures of wurtzite ZnO is possible at conditions that allow for fast growth along [0001] and negligible growth on all other ZnO facets.

Another approach to the growth of one-dimensional whisker structures is the utilization of screw dislocations. If an axial screw dislocation is present in a growing crystal, im-

19

pinging growth species are preferrably incorporated at the steps of the defect as schematically illustrated in Fig. 2.6a. As the crystal grows, the dislocation steps propagate in spiral-like motion resulting in uni-directional whisker growth along the dislocation axis (cf. Fig. 2.6b) [109, 110]. Originally invoked to explain the formation of whiskers with diameters in the micrometer range, the validity of this mechanism for the formation of nanoscale whiskers has also been demonstrated [108, 111, 112].

Besides achieving uni-directional growth, poor nucleation of nanostructures can also be an issue in catalyst-free VS growth resulting in low yields, e.g. for growth on atomically flat surfaces as seen in Paper I. It was explained in section 2.2.1 that nucleation occurs preferentially at low-energy sites on the surface. This can be exploited in different approaches for facilitating the nucleation of nanostructures. Dedicated seed or "nucleation" layers of the desired nanostructure material or buffer layers with high surface roughness can be deposited prior to growth in order to promote nucleation via homoepitaxy or surface nucleation sites, respectively [113–117]. Furthermore, surface defects such as impurities or etch pits can be utilized as nucleation centers on the substrate [118, 119]. Even the metal catalyst particles employed in VLS and VSS growth mechanisms can aid the nucleation of VS-grown nanostructures: at suitable growth conditions, the catalyst particle acts only as nucleation site for the nanostructure and remains at the bottom during growth [118, 120]. In PLD, nanostructure growth via the VS mechanism can also be initiated by the gas-phase formation of nanoparticles at high pressures within the ablation plume. Once deposited on the substrate, these nanoparticles act as nucleation centers and promote subsequent nanostructure growth [121].

In general, VS-grown nanostructures are catalyst-free and therefore - except for the cases of impurity-enhanced nucleation - usually also impurity-free. Additionally, no additional steps for the removal of catalyst particles at the tips of nanostructures are necessary in order to fabricate full devices. The dimensions of the grown nanostructures, however, depend only on the growth conditions and - if employed - the properties of the buffer or nucleation layer. Therefore, the growth of nanostructures by the VS mechanism as well as their positions and densities are often more difficult to control than nanostructure formation guided by a catalyst.

The Liquid-Solid (LS) mechanism

The VS growth mechanism can be adapted to material sources/precursors in the liquid phase (**LS**), i.e. solution-based growth methods. The above considerations for achieving one-dimensionality and nucleation of nanostructures can be directly transferred to the liquid phase. For overcoming the problem of nucleation, the utilization of seed layers is the
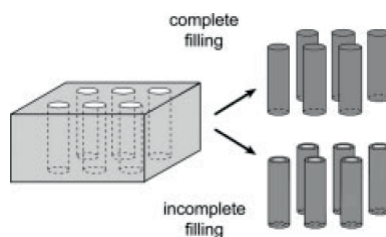
Figure 2.7: Schematic illustration of a template-assiste approach for the growth of nano-rods and nanotubes. *Reprinted with permission from [92]. Copyright 2003 John Wiley and Sons.*

most commonly used approach for promoting nanostructure nucleation from the liquid phase [122–124]. In many cases, uni-directional growth can be achieved without further efforts due to intrinsic differences in surface energies of the facets present during crystal growth. However, due to the liquid medium, solution-based methods allow for additional ways of guiding the growth into only a single direction. If the chemical reaction is carried out in a suitable solvent or if appropriate capping reagents are added, distinct surfaces of the growing crystal can be selectively passivated essentially inhibiting further attachment of atoms on these facets and reducing their growth rates [92, 125]. This effect is utilized in the fabrication of planar ZnO nanodisks as will be discussed in section 2.3.7.

Solution-based growth techniques are especially attractive for industrial fabrication of nanostructures. Since no vacuum chambers are required and no high temperatures are necessary for the growth of nanostructures, they provide low-cost alternatives to the vapour-phase deposition techniques described in the previous subsections. Furthermore, the isotropy of the liquid media offers high potential for industrial scale-up compared to the often directed and spacially confined material fluxes in vapour-phase techniques.

Template-based nanostructure growth

In another approach for overcoming the issue of uni-directional growth discussed above or for creating nanostructures with unusual, "unnatural" morphologies, a sacrificial template can be utilized to force a material into a desired shape. Thin films with cylindrical hollow pores such as anodic alumina membranes can be exploited as a template layer for the growth of nanorods or nanotubes [92]. During deposition, the rod-like voids are filled with the desired nanostructure material and, subsequently, the template is removed by thermal or chemical treatments as illustrated in Fig. 2.7 [126]. In another example, nanotube-like morphologies are achieved by the overgrowth of nanowire arrays with the material of choice. Subsequently, the core nanowires are removed by a thermally activated reduction process resulting in free-standing nanotubes on the substrate

21

surface [127]. In a different approach, nanotubes can be fabricated from compound semiconductur nanorods by simple oxidation of the outer nanorod shell and subsequent removal of the core nanorods by thermal treatments [128]. Since the shape of the resulting nanostructure is not governed by the properties of the grown material or the exact growth conditions in the template-based growth mechanism, nanostructures of virtually any morphology can be fabricated by this technique, only limited by the availability of suitable templates.

One of the drawbacks of template-assisted nanostructure growth is that full template removal is not always an easy task. Template or process chemical residues might impede the performance of devices based on this synthesis technique. Furthermore, the grown nanostructures are not necessarily of high crystal quality since the template can transfer its shape also to materials deposited in the amorphous or polycrystalline phase. If high crystal qualities are desired, additional post-deposition annealing treatments are often required [129–131].

For a more detailed discussion of these and additional template-based approaches to nanostructure growth, the reader is referred to reviews on this topic available in the literature (cf. Xia et al. or Cao and Liu [92, 132]).

2.3 ZnO nanostructures

In this section, various ZnO nanostructure morphologies are presented which have been demonstrated by a wide variety of growth techniques. Additionally, their individual growth mechanisms are discussed together with applications of the individual morphologies. Due to the immense number of publications on ZnO nanostructures, a comprehensive overview of all reported morphology types and fabrication techniques is beyond the scope of this chapter. The following subsections therefore focus on selected nanostructure types and growth techniques including the ones commonly encountered in the literature as well as those most relevant to this work.

2.3.1 Nanowires and Nanorods

The group of ZnO nanowires and nanorods - sometimes also referred to as nanofibres, -pillars or -whiskers - is the most widely studied type of ZnO nanostructure morphology [88, 89, 133, 134]. They commonly grow along the hexagonal c-axis, i.e. the ZnO[0001] direction of the ZnO crystal. The term "nanowires" describes high aspect-ratio morphologies with diameters in the range of several nanometers and lengths of up
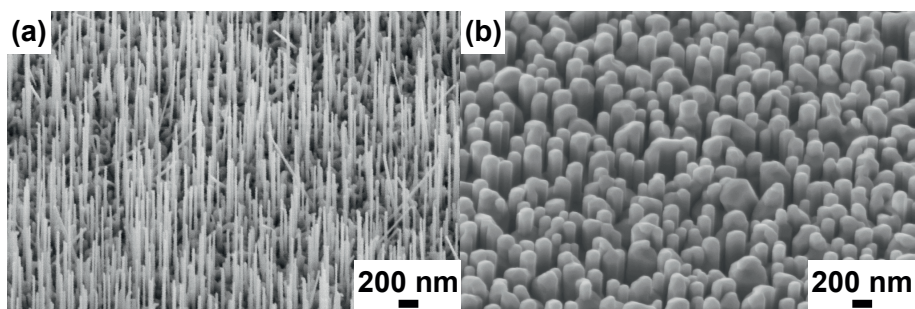
Figure 2.8: SEM images of ZnO nanowires (a) and nanorods (b) grown by pulsed laser deposition in the course of this work with and without the use of a metal catalyst, respectively.

to several tens of microns as shown in Fig. 2.8a. On the other hand, the word "nanorods" refers to straight, thicker structures with often lower aspect ratios and diameters of up to several hundreds of nanometers (cf. Fig. 2.8b). It should be noted, however, that both terms are often used interchangeably in the literature [135].

A common route to fabricating ZnO nanorods is the vapour phase transport (VPT) method, in which pure Zn or ZnO powders as well as ZnO:graphite mixtures are thermally evaporated from an alumina boat or a small quartz tube in a horizontal tube furnace. A schematic illustration of a basic VPT setup is given in Fig. 2.9. The evaporation boats are placed in the maximum temperature zone within the center of the furnace. Ar or N_2 gases are streamed into the furnace to help transporting the evaporated source material to a substrate (often placed downstream). The distance of the substrate to the evaporation source as well as the throughput and direction of the gas flows are directly related to the vapour supersaturation at the growth surface. Furthermore, since the evaporation source is located in the maximum temperature zone of the furnace, the distance between source and substrate also determines the growth temperature. By mixing small amounts of O_2 in the gas flow, additional oxygen can be provided to aid the ZnO nanostructure growth. The absolute pressures in the VPT tube furnace range from one to several tens of mbar during nanostructure growth.

The VPT method can be employed for the growth of ZnO nanorods and nanowires with and without the use of a metal catalyst particle [106, 136–140]. Huang et al. showed that the fabrication of ZnO nanowire arrays with diameters of 40-70 nm, up to 10 μm long is feasible with this method by growth from liquid Au droplets [141]. Furthermore, the authors demonstrated room-temperature lasing in the ultraviolet wavelength range from these wires [142]. Nikoobakht et al. observed a transition from standing to horizontal

tube furnace

Heater elements

gas flow

Exhaust

Ar or N$_2$ + O$_2$ gas inlet

powder source
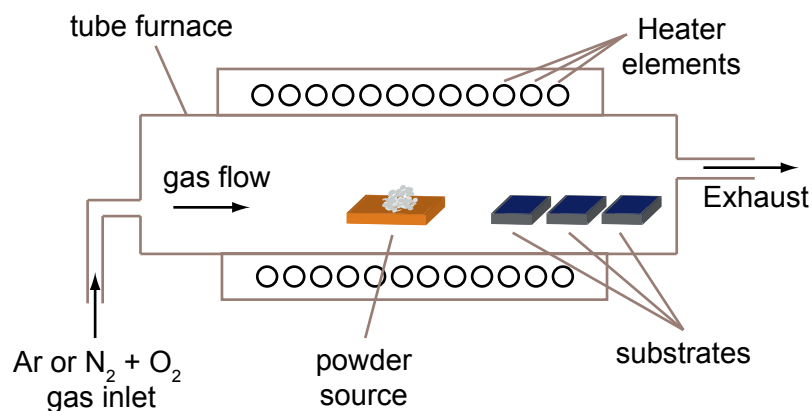
substrates

Figure 2.9: Schematic illustration of a typical setup for vapour phase transport growth of ZnO nanostructures. *Adapted from [5].*

nanowires on a-plane sapphire substrates upon reduction of the Au droplet size and attribute these findings to the different relaxation mechanisms of strain at the ZnO/sapphire interface. Below a critical Au droplet size of ∼25 nm, the wires grow horizontally on the substrate along the ZnO[11$\bar{2}$0] direction [143]. Even though the catalyst particles are often considered to be in the liquid phase during VPT growth, successful formation of ZnO nanowires has also been reported from solid Au droplets by this growth technique [97].

The presence of a catalyst is, however, not necessary for nanowires or nanorods to form in a VPT tube furnace reactor. In order to facilitate ZnO nanostructure growth, ZnO seed or nucleation layers are often deposited on the substrate prior to VPT growth as mentioned earlier [113, 116, 144]. Li et al. reported that the structural properties of the ZnO seed layer as well as the employed deposition technique play important roles for the characteristics of the resulting ZnO nanostructures, i.e. diameter, length, growth orientation and yield [116]. However, ZnO nanorod growth directly on a silicon substrate without the use of a nucleation layer has also been demonstrated. In these cases, the growth proceeds by a self-catalytic mechanism in which metallic zinc or zinc suboxides act as catalyst particles during growth [106, 145].

ZnO nanowires and nanorods can also be fabricated via the utilization of a pulsed laser to ablate material from a solid Zn or ZnO target (PLD). The basic principles and setup for this reactor type will be described in more detail in section 3.1. Liu et al. demonstrated ZnO nanowire fabrication from a Au catalyst by PLD with diameters of about 20 nm and lengths of up to 10 µm [146]. Rahm et al. fabricated ordered arrays of vertical ZnO nanorods by controlling the position and density of Au particles on the substrate

Main flow of reactant gases

Gaseous
by-products

Boundary
layer

Interface (negligible
thickness)

Substrate

Process steps involved:

1. Diffusion in of reactants through boundary layer

2. Adsorption of reactants on substrate

3. Chemical reaction takes place

4. Desorption of adsorbed species

5. Diffusion out of by-products
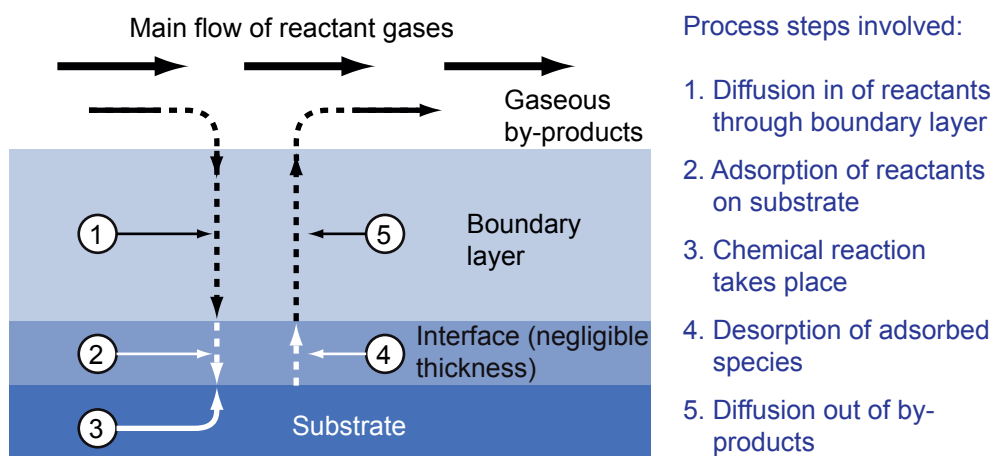
Figure 2.10: Schematic illustration of the processes involved during chemical vapour deposition. *Adapted with permission from [156].*

surface [74]. ZnO nanorod growth with the metal catalyst particle residing at the bottom of the nanowire has also been demonstrated in PLD. Depending on the Zn supersaturation in the chamber, the growth mode switched from VLS to VS growth with the Au particle only promoting the initial nucleation of the nanowire [118]. Moreover, ZnO nanorod and nanowire growth by PLD has been demonstrated in the absence of a metal catalyst particle [147–151]. Thereby, a ZnO seed layer can be employed to facilitate the nucleation of the ZnO nanowires and -rods [147, 152]. In an alternative approach, ZnO nanostructures are nucleated on a substrate by ZnO nanoparticles formed already in the ablation plume at high background pressures [121, 153, 154]. However, growth directly on a suitable substrate is also feasible as demonstrated by Park and co-workers who directly compared the growth of ZnO nanorods with and without the use of Au as catalyst on the substrate [155]. While ZnO nanorods grown directly on the Si substrate showed diameters of several hundred nanometers, the ZnO wires grown from the Au catalyst were only 30-100 nm thin and could be achieved in a wider window of growth conditions as the catalyst-free grown rods.

Besides the afore-mentioned physical vapour deposition techniques, ZnO nanowires and nanorods have been successfully fabricated using chemical vapour deposition (CVD) with metal-organic precursors (MOCVD). In CVD techniques, the desired growth materials are usually bound to a more complex precursor molecule, which must be cracked at the substrate surface in order to release the enclosed Zn atoms and enable ZnO growth. A schematic illustration of the processes involved during chemical vapour deposition is shown in Fig. 2.10. The precursors are usually supplied to the reaction chamber as

a vapour or elemental gas. For the growth of ZnO nanostructures by MOCVD, suitable precursor molecules include diethyl zinc (DEZn), dimethyl zinc (DMZn) and other Zn-containing metal-organic compounds [6, 114, 157, 158]. Since these molecules are typically in the liquid state under standard conditions, a precursor vapour needs to be generated first by streaming a carrier gas (usually hydrogen or nitrogen) through a heatable reservoir - a so-called "bubbler" - of the liquid precursors. The carrier gas transports the vapour through gas inlets into the reaction chamber, where it meets with a flow of molecular oxygen. The precursor molecules adsorb on the substrate surface and undergo a chemical reaction in which the metallic Zn is released. As ZnO begins to grow on the substrate, the organic waste products generated by the precursor cracking desorb from the surface and are pumped out of the chamber through appropriate exhaust lines. In cases, where the reactants or the resulting waste products are toxic, the exhaust lines need to be modified for proper waste treatment and disposal.

MOCVD growth of ZnO nanowires and -rods is typically carried out at relatively low substrate temperatures of about 500°C to 600°C without the use of a metal catalyst [114, 115, 159–161]. Although ZnO nanostructure fabrication has been demonstrated for MOCVD growth directly on silicon or sapphire substrates [158, 159, 162], a thin ZnO buffer or seed layer is often employed to facilitate the nucleation of ZnO nanowires [114, 115, 160, 161]. Park et al. reported direct influence of this buffer layer on the growth direction and orientation of ZnO nanowires [115]. While ZnO buffer layers grown above 200°C led to vertical nanowires along the common ZnO[0001] direction, tilted wires with a $[10\bar{1}0]$ growth direction were observed when the substrate temperature for buffer deposition was kept below 200°C. Similarly, Kim et al. reported changes in ZnO nanowire growth orientations for different thicknesses of the ZnO buffer layer [160]. Liu et al. reported that control over the growth orientation of ZnO nanowires could also be achieved by the application of an electric field [163]. When a plasma is generated in the reaction chamber, the resulting bias between plasma and substrate guides the charged adatoms to the growth front at the polar ZnO(0001) surface and forces the wires to grow vertically from the substrate.

Even though ZnO nanostructure growth by MOCVD is usually carried out without a metal catalyst, few reports exist that demonstrate the feasibility of catalyst-assisted nanowire growth. Thereby, the metal can act either as an active site on the surface initiating the nanowire growth [164, 165] or as a particle guiding the growth at the nanostructure tip as in the VLS mechanism [157]. Substrate temperatures of 900°C and higher seem to be necessary for ZnO nanostructure synthesis to occur by the latter growth mode [157, 165].

All of the fabrication routes for ZnO nanostructures discussed above involve the use

of high temperatures and/or high vacuum systems. For MOCVD, the proper treatment of waste products from the precursor cracking imposes additional technical efforts and costs. As a low-cost and scalable alternative to these techniques, solution-based processes have received great attention for the synthesis of ZnO nanostructures in the past decade [166]. In hydro- and solvothermal[1] synthesis routes, zinc salts such as zinc nitrate are mixed with hexamethylenetetramine, ammonium carbonate or other capping agents and stirred vigorously for several hours at temperatures between 40°C and 200°C [8, 168, 169]. The diameters of the fabricated nanowires range from few tens of nanometers to micron-sized rods and can be controlled by different parameters such as reactant concentrations (i.e. supersaturation) and growth temperature [123, 168, 170, 171]. While in the first reports on solution-based synthesis of ZnO microrods the growth was carried out directly on a substrate [172], Greene and co-workers showed that the use of a textured ZnO seed layer facilitates control over the orientation of the grown ZnO nanorods with respect to the substrate surface [123]. In the same year, Greene, Law and co-workers demonstrated a functional dye-sensitized solar cell on the basis of ZnO nanowires grown by this method [173]. Textured ZnO layers for use as seeds in ZnO nanowire growth can be easily prepared by virtually any high-vacuum thin film deposition technique [158, 170], but also by low-cost methods such as repeated spin-coating or dripping of a diluted zinc salt solution and subsequent annealing at temperatures above 300°C [123, 133, 174]. The structural properties of this seed layer (e.g. degree of texture, thickness and surface roughness) have great influence on the orientation, diameter and density of the hydrothermally grown ZnO nanorods [122, 124, 150, 174–176].

ZnO nanorods can also be fabricated in liquid media by electrochemical processes referred to as electrodeposition. This technique employs an electric bias to direct the growth of ZnO from dissolved zinc salts on the cathode (substrate) of the electrochemical cell. Two different approaches have been utilized in literature for the electrochemical growth of ZnO nanorods: in the template-based approach, porous alumina anode membranes are utilized to deposit Zn or ZnO into nanosize channels of the alumina template [75, 177]. The filled pores are subsequently annealed at temperatures of up to 400°C to oxidize the Zn in the channels and improve the crystallinity of the rods. In the second approach, growth is performed directly on the cathode substrate without the use of a seed layer or template membrane [178, 179]. Various zinc-containing salts can be employed and an additional capping agent can also be added to aid the formation of uni-directional ZnO nanostructures [179–182].

Various potential applications have been presented for ZnO nanorods and -wires during

---

[1]Strictly speaking, the term "hydrothermal" (or "solvothermal") refers to reactions of aqueous (or solvent) mixtures in sealed autoclaves involving elevated temperatures and pressures. In literature, however, this terms is often used also for aqueous solution growth of nanowires in open beakers and is thus not differentiated in the present discussion [167].

the past decades. By growth of ZnO nanowires on a conductive bottom layer and the subsequent application of an organic dye or active polymer, excitonic solar cells can be fabricated as denoted earlier [133, 167, 173, 183–186]. The integration of nanostructures in such solar cells offers increased interface areas important for charge carrier collection and direct electron pathways to the electrode [187]. Furthermore, single ZnO nanowire transistors have been fabricated from ZnO nanowires in surround- or top-gated configurations utilizing different working principles such as field-effect or piezopotential-gated transistors [188–191]. Such nanowire transistor configurations can be employed as sensors for gases such as H_2, O_2, NO_2 or ethanol, for biomolecular interactions, vacuum pressures or strain [191–197].

Furthermore, ZnO nanowires can be applied in optoelectronic devices. As already mentioned earlier, lasing in the ultraviolet wavelength range has been demonstrated for ZnO nanowires even at room-temperature [142, 198, 199]. Moreover, ZnO nanowires can be utilized as LEDs [200–202]. Due to the persisting difficulties of reproducible p-type ZnO preparation [203], these devices are usually prepared as hybrids with n-type ZnO nanowires grown on a p-type substrate such as p-GaN [14]. However, first reports exist on all ZnO nanowire LEDs and lasers, involving the growth of p-type ZnO nanowires on n-type ZnO films [14, 204].

Other interesting applications of ZnO nanowires are based on the piezoelectricity of ZnO. Wang et al. demonstrated that polar ZnO nanobelts could be used as nanogenerators, providing a novel approach to mobile power supplies [16]. Upon mechanical shocks or vibrations, the piezoelectric effect generates an electrical current in the nanowire. Due to the small size of the wires, the power supply could be activated by the mechanical strain induced by a walking human. Furthermore, The piezoelectric effect of ZnO nanowires opens up several other potential applications such as piezotronics and piezo-phototronics [16].

2.3.2 Nanobelts

Another common type of ZnO nanostructures is the so-called nanobelt. As the term already indicates, this structure is described by a belt-like morphology with several tens to few hundreds of nanometers in width and only 10 - 50 nm thin [205]. The widths and thicknesses are maintained throughout the entire length of the structure, which can be in the millimeter range [206]. The first nanobelts have been demonstrated by the VPT method in Wang's group during the early years of the new millennium [207]. TEM images of these nanobelts are shown in Fig. 2.11. The authors achieved the nanobelt morphology by evaporating the ZnO source material in a horizontal tube furnace at extremely high temperatures of 1400°C without employing any metal catalyst.
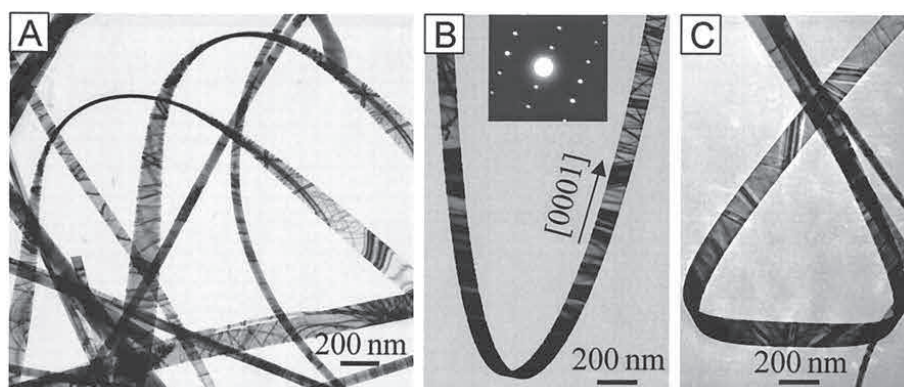
Figure 2.11: TEM images of various ZnO nanobelts showing their characteristic shapes. *Reprinted with permission from [207]. Copyright 2001 American Association for the Advancement of Science.*

Z.L. Wang defines three different types of ZnO nanobelts that can be fabricated by the VPT method [5]. Type I grows along the ZnO[0001] direction and is enclosed by the $(2\bar{1}\bar{1}0)$ plane as main facet and the $(01\bar{1}0)$ surface (cf. Fig.2.12a). In type II, the $(01\bar{1}0)$ facet acts as growth front with the ZnO(0001) and ZnO$(2\bar{1}\bar{1}0)$ planes constituting the small and wide side facets, respectively (Fig. 2.12b). A characteristic feature of this nanobelt type is the planar stacking fault in the ZnO(0001) plane which can be observed along the entire length of the belt [207]. The last type of ZnO nanobelts is depicted in Fig. 2.12c. It has either a $(2\bar{1}\bar{1}0)$ or $(01\bar{1}0)$ plane as growth front with the ZnO(0001) plane being exposed at the large-area flat surface, while the $(01\bar{1}0)$ or $(2\bar{1}\bar{1}0)$ facets, respectively, are found at the small-area side facets. Due to the large surface area of the polar ZnO(0001) plane, this type is also referred to as a "polar" nanobelt [5].

Compared to the growth of ZnO nanowires by the VPT method, the nanobelt morphology can be achieved by the same technique, if the substrate is located closer to the source material in the tube furnace [208]. This corresponds to an increase in ZnO supersaturation and substrate temperature, which are important parameters for determining the morphology of the ZnO nanostructure [136]. Although a metal catalyst is generally not necessary for the fabrication of belt-like morphologies [209], catalyst-assisted ZnO nanobelt growth has been demonstrated with the VPT method using Au, Ag or Sn as a catalyst [210–212]. Ding et al. observed the growth of polar as well as type II nanobelts with the Sn catalyst [211]. Contrary to the catalyst-free fabrication, the type II nanobelts were single-crystalline without any stacking fault along the length of the belt. Further-

29

(a) Nanobelt type I   **(b)** Nanobelt type II   **(c)** Polar nanobelt

(0001) $(01\bar{1}0)$ $(2\bar{1}\bar{1}0)$ or $(01\bar{1}0)$

$(01\bar{1}0)$

Planar defect (0001)

(polar surface) $(01\bar{1}0)$ or $(2\bar{1}\bar{1}0)$

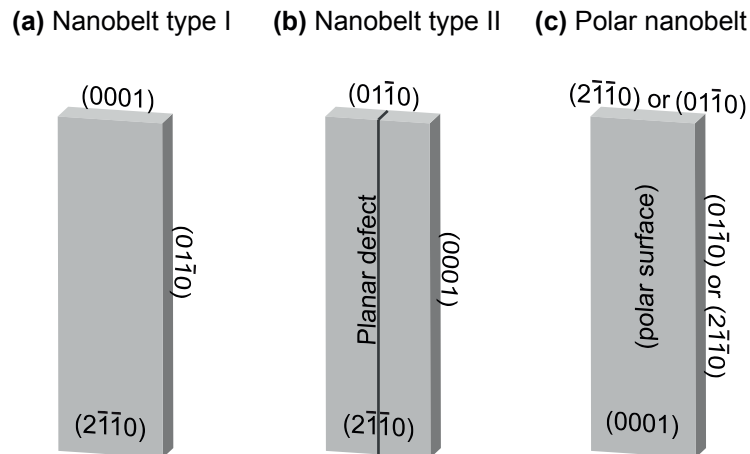$(2\bar{1}\bar{1}0)$ $(2\bar{1}\bar{1}0)$ (0001)

Figure 2.12:   Three different types of ZnO nanobelts with their characteristic growth fronts and side facets. *Adapted from [5].*

more, a close correlation between the nanostructure morphology and the catalyst/ZnO epitaxial relationships were found. Xing et al. reported the growth of single-crystalline ZnO nanobelts by the VPT method utilizing Ag as catalyst metal [212]. The belts were ultra-thin with thicknesses as small as few monolayers of ZnO ($\sim$ 2 nm). In most of the above reports, the formation of ZnO nanobelts from a catalyst is attributed to the VLS mechanism, i.e. the catalyst resides at the growth front of the belt. However, Sun et al. report on the formation of ZnO nanobelt arrays from nano-sized Sn/SnO$_2$ catalysts acting only as seed particles [213].

In order to fabricate the third ZnO nanobelt type - the "polar nanobelt" - the introduction of In as a dopant has been identified as a key ingredient [24,214,215]. Fan et al. observed a switching in nanostructure morphology from c-axis oriented ZnO nanowires to polar nanobelts growing along the ZnO a-axis upon inserting an additional In$_2$O$_3$ source in the tube furnace [215]. Wang et al. confirmed that the introduction of In- or Li-dopants plays a key role for the fabrication of polar ZnO nanobelts at high yields [24]. The dopants introduce planar defects (inversion domain boundaries) which seem to be responsible for the stabilization of the polar ZnO nanobelt configuration.

Besides the widely used VPT method, other growth techniques have been successfully employed for the growth of ZnO nanobelts. Via a simple oxidation of Zn metal plates in a tube furnace at relatively low temperatures (400-500°C) ZnO nanobelts of type I have been fabricated [216–218]. Zhang et al. reported on the hydrothermal synthesis of single-crystalline ZnO nanobelts with thicknesses of 10-20 nm and 20-200 nm in

width [219]. Zinc sulfate, urea and ethanol were mixed in an alkaline solution (pH = 14) and heated to 160°C in a sealed autoclave for 16 hours. As reaction products, the authors observed not only the nanobelt type depicted in Fig. 2.12a, but also an alternative type I of ZnO nanobelts with the ZnO(01$\bar{1}$0) plane forming the flat surface and the ZnO(2$\bar{1}\bar{1}$0) plane at the side facets. Hattori et al. combined nanoimprint lithography with grazing incidence PLD to fabricate ordered arrays of ZnO nanobelts standing on a substrate with the thin side facet aligned parallel to the substrate surface [220]. Furthermore, RF sputtering and electrochemical synthesis as well as less common approaches such as microwave-assisted techniques or electron beam irradiation of polyhedral Zn nanoparticles have been employed [221–224].

ZnO nanobelts offer a wide range of potential applications partly overlapping with those of ZnO nanowires, e.g. field effect transistors, field emitters, Schottky diodes, dye-sensitized solar cells as well as stimulated emission and lasing [212, 225–230]. Gas sensing properties of ZnO nanobelts have been demonstrated for various organic as well as inorganic substances including H_2, O_2, NO_2, NH_3, hydrocarbons and ethanol [218, 222, 231–233]. Due to their flat morphology, ZnO nanobelts show potential as nanocantilevers for use in scanning probe microscopes and other techniques involving the use of cantilevers [234]. Furthermore, photosensors and UV detectors consisting of single ZnO nanobelts have been demonstrated [235, 236]. Upon illumination with UV light, the electrical conductance through the nanobelt is drastically increased, which can be exploited for photosensitive switches in integrated circuits [235]. When the belt surface is functionalized by a polymer, UV photodetection can be further enhanced by several orders of magnitude [236]. The optical properties of ZnO nanobelts can also be utilized for photocatalytic reduction of toxic organic pollutants in wastewater to less harmful species such as CO_2 and water [213]. Furthermore, Ahmad et al. proposed that Al-doped ZnO nanobelts could be used for hydrogen storage [237]. They report on an H_2 storage capacity of 2.94wt % in a nanobelt. About 80 % of the stored hydrogen was released again upon heating the nanobelts to 370K. Other promising applications of ZnO nanobelts are offered by the piezoelectric properties of the polar type of nanobelts. Zhao et al. could show that the piezoelectric coefficient of polar ZnO nanobelts exceeds the value of bulk ZnO [238]. Similar to ZnO nanowires, it is proposed that ZnO nanobelts could be utilized as nanogenerators or as building blocks in piezotronics or piezo-phototronics [16].

2.3.3 Nanorings, -springs and -helices

When the growth conditions in the tube furnace of the VPT reactor are optimized for high yields of polar ZnO nanobelts (cf. Fig. 2.12c), for example by doping with In or

Li [24], novel uncommon ZnO nanostructure morphologies can be fabricated as reported by Kong et al. [239]. Closed ZnO nanoring shapes as well as spring-like morphologies (cf. Fig. 2.13b and d) have been observed under these conditions [24, 239, 240]. The nanosprings have radii of about 500-800 nm and reach several microns in length. For the closed ZnO nanorings, two different types with diameters of up to several microns have been found by Kong and co-workers [240]. In type I, the ZnO[0001] direction is the nanoring axis and ZnO[1$\bar{2}$10] is the radial direction. For type II, ZnO(1$\bar{2}$12) is the plane of the nanoring and ZnO[1$\bar{2}$13] constitutes the radial direction. A third type of ZnO nanorings has been observed by Wu et al. using thermal evaporation of ZnS and carbon powders [241]. The radial direction of the rings is ZnO[0001] and the ring plane is formed by ZnO(2$\bar{1}\bar{1}$0) face. Both ZnO nanorings as well as the nanosprings are made up of ZnO nanobelts that are "rolled over" to form the described shapes as depicted in Fig. 2.13. The belts are about 5 - 20 nm thick and have polarization charges located on the polar ZnO{0001} surfaces, thus creating electrostatic energy. The structures therefore attempt to neutralize these electrostatic charges by rolling over into an enclosed ring structure or spiral shapes. However, the bending of the nanobelt creates elastic energy. The total structure is therefore determined by balancing electrostatic and elastic energies [24].

Besides the spring- and ring-like structures, a nanohelix shape depicted in Fig. 2.14b has also been observed under these conditions. These helices are considerably smaller than the nanosprings ($\sim$ 50 nm radius) [24, 206] and their growth mechanism is based upon periodic changes in the structures' growth direction rather than the curling of ZnO nanobelts. Even though the overall axis of the nanohelix is the ZnO[0001] direction, the microscopic growth occurs along the $\langle 01\bar{1}1 \rangle$ directions. Thereby, the growth direction cycles periodically through the six equivalent ZnO $\langle 01\bar{1}1 \rangle$ directions as depicted in Fig. 2.14c [24, 206]. These ZnO nanohelices showed high elastic properties with a "shape memory" effect [206]. After stretching the helix to a straight wire, it returned to its original shape upon relaxation of the pulling force.

2.3.4 Nanotetrapods

It is known for a long time that ZnO crystals can adapt tetrapod-like shapes. Already in 1944, M. L. Fuller observed ZnO "fourlings" through a stereoscopic microscope [243]. When the research community began to focus on the fabrication of ZnO nanostructures during the past decade, such tetrapod structures have also been observed on the nanoscale. Dai et al. reported on the growth of ZnO nanotetrapods by oxidation of Zn powder using the VPT method [244]. The legs of the tetrapods were about 2-3 μm long
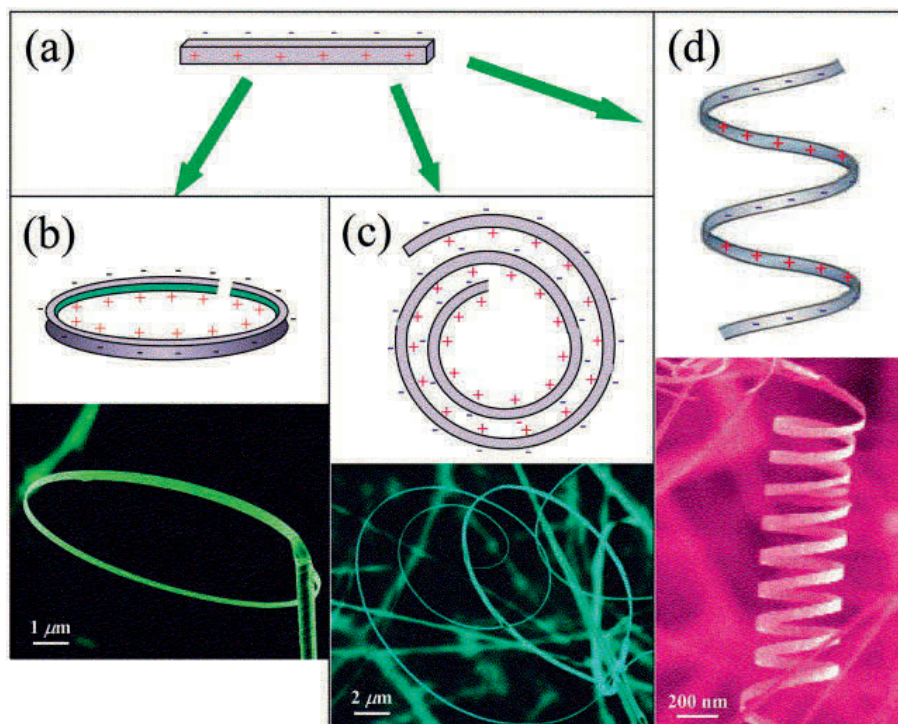
Figure 2.13: Schematic illustration of the formation of ZnO nanorings and -springs. Electrostatic forces cause a polar ZnO nanobelt (a) to "rolled over" and form a nanoring (b), a nanospiral (c) or a nanospring (d). *Reprinted with permission from [242]. Copyright 2004 Elsevier Ltd.*
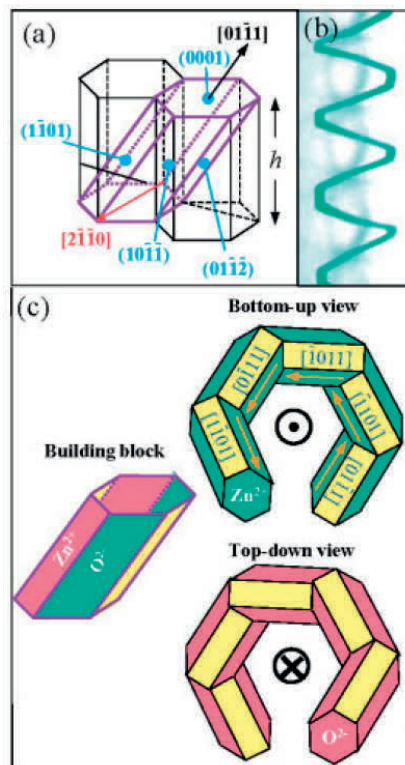
Figure 2.14: Structure model of a ZnO nanohelix. (a) Schematic illustration of a building block for the ZnO nanohelix. (b) A model of a ZnO nanohelix structure. (c) Bottom-up and top-down views of the nanohelix model indicating the stacking of building blocks resulting in the final structure. *Reprinted with permission from [24]. Copyright 2004 John Wiley and Sons.*
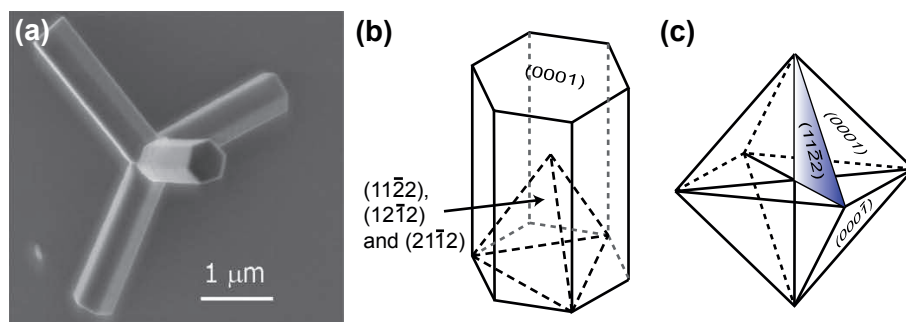
Figure 2.15: SEM image of a ZnO nanotetrapod (a) and schematic illustration of the tetrahedral building blocks (b) that are joined to an octa-twin nucleus initiating the nano-tetrapod formation. *Reprinted (a) and adapted (b and c) with permission from [245].* *Copyright 2007 Elsevier Ltd.*

and the central nucleus had diameters of about 70-150 nm.

A typical tetrapod morphology is shown in Fig. 2.15a. It is believed that the basis for the formation of tetrapod ZnO crystals is a so-called octa-twin nucleus formed in the gas-phase during growth in oxygen-rich environments [24, 245, 246]. This nucleus consists of eight tetrahedral crystals with $\{11\bar{2}2\}$ pyramid facets and $\{0001\}$ basal planes as depicted in Fig. 2.15b. These eight crystals are joined together at the $\{11\bar{2}2\}$ pyramid facets to form an octahedron so that all facets of the resulting nucleus are $\{0001\}$ basal planes (cf. 2.15c) [247]. Four of the octahedron facets consist of O-terminated $ZnO(000\bar{1})$, while the other four are Zn-terminated (0001) planes [24, 245]. As mentioned earlier, the $ZnO(0001)$ surface is chemically more active than the $ZnO(000\bar{1})$ plane. Therefore, wurtzite ZnO grows along the $ZnO[0001]$ direction only on the four active Zn-terminated $ZnO(0001)$ basal planes of the octa-twin, leading to the four legs of the tetrapod.

The VPT technique is probably the most frequently used method for the fabrication of ZnO nanotetrapods [24, 245, 248, 249]. By controlling the growth conditions such as the oxygen partial pressure in the reactor, the morphologies of the ZnO tetrapods can be slightly varied [246]. Pearl-necklace-shaped legs of the tetrapod, for example, can be achieved by mixing Zn, ZnO and carbon powder as a source material [250]. Besides VPT, other methods have been successfully employed to fabricate ZnO nanotetrapods. Lin et al. utilized a DC plasma reactor to form ZnO nanotetrapods at high yields of up to half a kg per hour [251]. In their setup, metal Zn powder is oxidized in a flame of DC plasma generated with input powers of up to 90kW and the resulting nanopowder is subsequently collected in a filter bag. In a similar approach, a Zn melt is sent through a
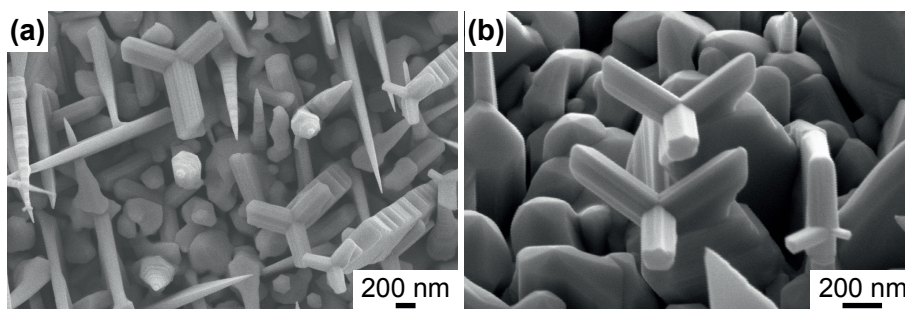
Figure 2.16:   SEM images of ZnO tetrapod-like shapes grown by PLD in the course of this work.

nozzle and ignited by a welding torch using oxygen and acetylene gas [252]. The synthesized ZnO nanotetrapods are then collected on a cooling plate. Solution-based synthesis methods have also been successfully employed for the fabrication of tetrapod-like ZnO nanostructures [253, 254]. Lupan et al. mixed a solution of zinc sulfate and ammonia in a hydrothermal reactor heated to 90-98°C for 15 minutes and collected the resulting ZnO nanotetrapods on a glass substrate [253]. During the preliminary work for this thesis, tetrapod-like shapes have also been observed by pulsed laser deposition of ZnO nanostructures as shown in Fig. 2.16.

Similar to the other ZnO nanostructures described above, nanotetrapods have a wide variety of potential applications, such as dye-sensitized solar cells or gas sensors [228, 255, 256]. It has also been shown that ZnO nanotetrapods have excellent field emission properties [257, 258] and a field emission display with a 72 x 72 pixel array based on ZnO nanotetrapods has been demonstrated [259].

2.3.5   Nanotubes

Since the discovery of carbon nanotubes in the early 1990's [260], tubular structures have received increased attention by the research community. As of today, the fabrication of ZnO nanotubes has been demonstrated using a variety of approaches. A typical ZnO nanotube structure is shown in Fig. 2.17. The cross-section of the tubes usually resembles the hexagonal shape of the ZnO lattice with ZnO[0001] as the growth direction of the tubes.

One method for achieving tubular structures on the nanoscale is the employment of suitable template structures. For this purpose, ZnO is often deposited into the pores of anodic
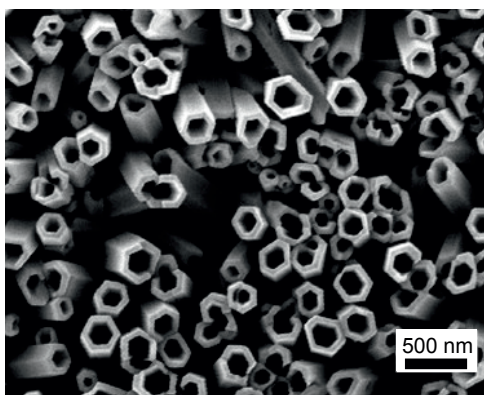
Figure 2.17: SEM image of an as-synthesized ZnO nanotube array. *Reprinted with permission from [261]. Copyright 2009 Elsevier Ltd.*

alumina membranes, which have diameters on the order of several tens to few hundreds of nanometers. In order for nanotubes to grow inside these pores, the ZnO material must be deposited preferrably at the walls of the membrane before the pores are filled up, otherwise ZnO nanowires would be formed [129]. This preferential deposition can be achieved by isotropic ZnO growth facilitated by, for example, sol-gel methods or atomic layer deposition [129, 130]. Electrodeposition can also be used, if a thin Au layer is deposited on the back surface of the membrane, reaching only slightly over the pore edges and guiding the subsequent ZnO growth onto the overlapping Au film [131]. The as-deposited ZnO nanotubes are amorphous or polycrystalline and are often annealed at elevated temperatures to achieve crystallinity [129–131]. In another template-assisted approach, Zn nanowires are fabricated first and subsequently oxidized in a suitable atmosphere/chemical environment [195, 262]. During this oxidation process, a ZnO sheath is formed around the Zn nanowire core. In the final step, the template is removed via the sublimation/evaporation of the Zn core by thermal treatments. The diameter of the resulting ZnO nanotubes is determined by the corresponding diameter of the initial Zn nanowires. As an alternative to nanowire templates, Zn-ZnO core-shell nanobelts can also be utilized for the fabrication of ZnO nanotubes [263].

A further variation of template-based preparation is the etching of ZnO nanorods by potassium or sodium hydroxide or hydrochloric acid [261, 264, 265]. Since the ZnO(0001) has the highest surface energy, its etching rate is the fastest, leaving behind only the sidewalls consisting of the more stable and low-energy $(10\bar{1}0)$ facets. This process has been observed experimentally by recording SEM images at different etch times (cf. Fig. 2.18). Sufficiently high defect densities in the ZnO nanorod crystal are required for successful etching of the nanotube structure [265]. Besides these techniques, ZnO nanotubes can also be fabricated by hydrothermal growth of ZnO on PLD-grown buffer
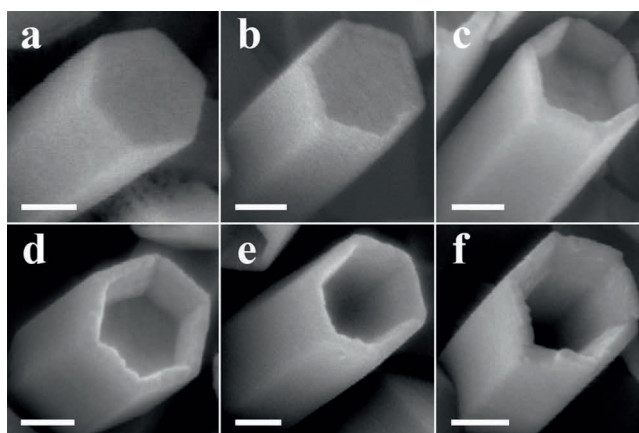
Figure 2.18: The different stages of ZnO nanotube formation by the etching of hexagonal ZnO nanorods visualized by SEM images. *Reprinted with permission from [264]. Copyright 2008 American Institute of Physics.*

layers [266, 267], direct electrodeposition on ITO [268], VPT growth directly onto the substrate (catalyst-free as well as catalyst-assisted) [269–271] as well as MOCVD [272].

Potential applications of ZnO nanotubes include ethanol or hydrogen sensors [195, 273], photocatalysis [265], dye-sensitized solar cells [130, 274], white light emitting diodes [275] as well as field emitters [276]. Kong et al. reported superior sensitivity of ZnO nanotubes as glucose biodetectors over ZnO nanorod or planar devices [261].

2.3.6 Nanocombs

The morphologies of typical comb-like nanostructures are shown in Fig. 2.19. The basis of a ZnO nanocomb is a nanobelt or nanowire structure as backbone with ZnO nanowires growing as dendritic sidebranches or teeth from the sides of the stem. The structure is single-crystalline and, typically, the backbone grows along the $[01\bar{1}0]$ or $[2\bar{1}\bar{1}0]$ direction of the ZnO crystal. While the growth of the stem can be achieved with and without the use of a metal catalyst [15, 278–280], the branched nanowires grow in the ZnO[0001] via a VS or self-catalyzed growth mechanism [15, 281]. Thereby, the branches can be evenly spaced with distances ranging from 0.3 μm to 2 μm [277, 282].

The most commonly observed nanocomb structure is a single-sided comb with teeth growing only from one edge of the backbone, namely the Zn-terminated (0001) face. This can be explained by the differences in chemical activity of the ±(0001) planes as

38

Figure 2.19: SEM images of ZnO nanocomb structures at different magnifications (a-c). The higher magnification images show nanocomb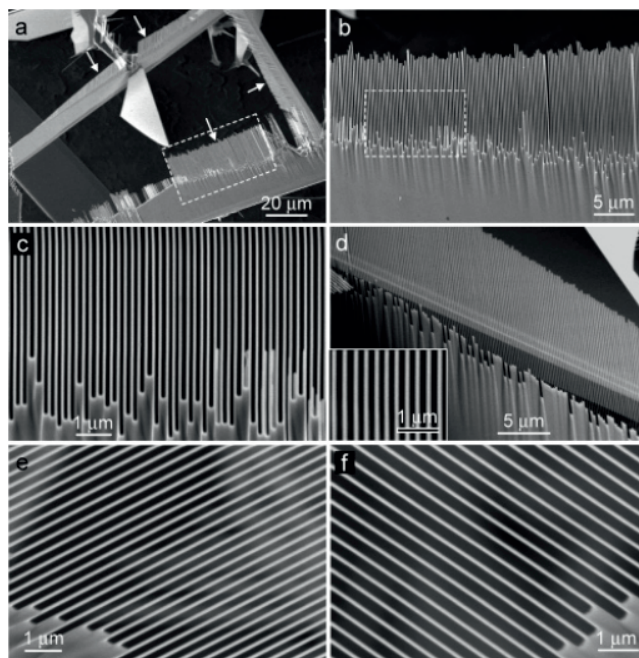s with various dimensions and spacings of the periodic nanowire branches. *Reprinted with permission from [277]. Copyright 2005 American Chemical Society.*

already mentioned in section 2.1. Furthermore, Wang et al. identified tiny Zn clusters at the nanowire tips suggesting a self-catalyzed growth mechanism of the branches [15]. However, double-sided as well as three-sided ZnO nanocombs have also been reported in literature with a ZnO $\langle 0001 \rangle$ and a $\langle 2\bar{1}\bar{1}0 \rangle$ direction as the second and third branching directions, respectively [280, 281, 283, 284]. Different origins have been identified for the formation of double-sided combs. While Lao et al. observed symmetric combs with both sides of the branches growing along the Zn-terminated [0001] direction due to an inversion domain boundary [283], Zhang et al. also reported the growth of nanowire branches from the O-terminated $(000\bar{1})$ plane [281].

The most common growth technique for the fabrication of ZnO nanocomb structures is the VPT method. Pure Zn, ZnS and ZnO powders can be used as source materials [282, 284, 285], often mixed with carbon powders such as graphite, black carbon powder or single-wall carbon nanotubes [278, 286, 287]. The growth conditions for successful fabrication of ZnO nanocombs vary significantly and seem to depend largely on the individual instrumental setup employed. For instance, nanocombs have been observed for evaporation at temperatures between 440°C and 1400°C in flows of typically Ar or Ar/O_2 gas mixtures [281, 283]. Furthermore, depending on the setup, ZnO nanocombs grow on substrates kept in temperature zones of the tube furnace ranging from 440°C to above 900°C [281, 286]. The fabrication of In-doped nanocombs by introduction of a In/In_2S_3 source into the tube furnace has also been demonstrated [4].

Besides the VPT method, ZnO nanocomb structures can be fabricated from and on a brass ($Cu_{0.66}\,Zn_{0.34}$) foil by oxidizing the material in a tube furnace [288]. Chen et al. demonstrated the fabrication of ZnO nanocombs by a two-step process [289]. First, ZnO nanowires are hydrothermally grown on one half of the substrate. In a second step, ZnO growth is carried out by the VPT method on the same substrate, leading to the formation of ZnO nanowires on the uncoated half of the substrate as well as ZnO nanocombs at the interface between the hydrothermally and VPT-grown wires.

The potential applications of comb-like ZnO nanostructures include many of those previously mentioned for the other ZnO nanostructure types, e.g. field emitters, dye-sensitized solar cells, ethanol and biosensors [290–293]. However, nanocombs may offer unique possibilities due to the ordered array and periodicity of the nanowire branches. Pan et al. realized a diffraction grating for integrated optics from a ZnO nanocomb structure, showing distinct diffraction maxima upon monochromatic laser illumination [277]. ZnO nanocombs are also suitable candidates for UV nanowire laser arrays due to the presence of Fabry-Perot optical cavities induced by the ZnO/air interfaces on both ends of the nanowire branches [282, 289]. Furthermore, nanocantilever arrays based upon nano-
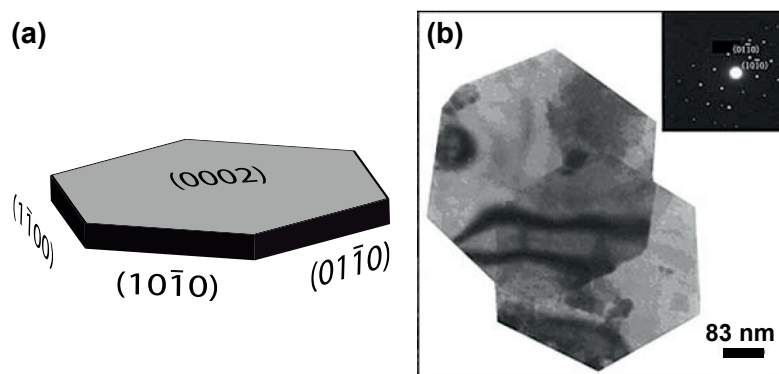
Figure 2.20: Schematic illustration (a) of a hexagonal nanodisk denoting the different facets. Corresponding TEM image (b) and selected-area diffraction pattern of a hexagonal nanodisk. *(b) is reprinted with permission from [294]. Copyright 2006 Springer Science and Business Media.*

combs have been proposed for utilization in scanning probe techniques [15].

2.3.7 Nanosheets

ZnO can crystallize in a flat and two-dimensional morphology which we refer to here as "nanosheets". Even though these structures are often expanded in two dimensions up to several tens of micrometers in width and length, the prefix "nano" is justified by the small thickness of these sheet-like shapes which is typically in the range of several tens to few hundreds of nanometers. Nanosheets are therefore often characterized by high aspect ratios with respect to the relation between thickness and width/length of the structures. Besides "nanosheets", alternative terms such as "nanodisks" or "nanoplatelets" are frequently used to describe these morphologies [136, 294–296]. Different profiles of ZnO nanosheets have been reported, including rectangular sheets [297], round [298, 299] or hexagonal disks [294, 300–302] as well as triangular [303–305] and disordered [136, 306, 307] structures.

Contrary to the previously described ZnO nanostructures, the most frequently employed methods for the synthesis of ZnO nanosheets are solution-based growth techniques such as hydrothermal synthesis and electrodeposition [180, 181, 300, 301, 308–310]. The nanosheets prepared by these methods often (but not exclusively) exhibit disk-like shapes with a hexagonal perimeter resembling the basal plane of the ZnO crystal structure [180, 295, 300, 301, 308, 311]. Such a hexagonal ZnO nanodisk is shown schematically in Fig. 2.20a. It has been shown by TEM investigations that the large-area

surfaces of these hexagonal nanodisks consist of ZnO$\{0001\}$ facets while the hexagonal perimeter is formed by $\{01\bar{1}0\}$ surfaces form (cf. Fig. 2.20b) [294, 300]. Since the thickness of the sheets is typically orders of magnitude smaller than their two-dimensional expansion, this implies that the low-energy $\{01\bar{1}0\}$ facets must have higher growth rates than the high-energy ZnO$\{0001\}$ surfaces during the synthesis process. This is in conflict with the relative growth rates commonly observed for the growth of wurtzite ZnO, where the ZnO$\{0001\}$ facets have the highest surface energy of all low-index ZnO planes and thus grow the fastest in order to minimize the areas of high energy [31]. The formation of hexagonal ZnO nanodisks is therefore often explained by the suppression of ZnO growth on the (0001) surface. This can be achieved by adding suitable surfactants or capping agents to the growth mixture, for example, negatively charged ions such as chlorides and phosphates which adsorb on the Zn-terminated (0001) growth facet and inhibit the adsorption of ZnO growth species on this surface [181, 299, 310, 312, 313].

In the solvothermal and electrochemical growth techniques, $ZnCl_2$ [295, 314], $Zn(NO_3)_2$ [300, 306], zinc sulfate [315] or zinc acetate [299, 316] are typically employed as Zn source. Reagants such as hydroxides [314–316] as well as suitable capping agents, e.g. citric acid, chlorides or phosphates [299, 312, 313], are then added in order to guide the growth of the nanostructure into the sheet-like shapes. The electrolyte or growth mixture can be kept at room temperature or may be heated to temperatures of up to 200°C. Depending on the individual setup (e.g. utilization of a sealed autoclave), various growth parameters such as temperature, growth duration, pH as well as molar concentrations (supersaturation) can have key influence on the morphology of the synthesized nanosheets [180, 294, 309]. Furthermore, ZnO nanoparticles or thin films can be utilized as seeds to facilitate nucleation and initiate the nanostructure growth [295, 310, 316]. Besides the mentioned growth parameters, the current density can play an important role for the final nanostructure morphology during electrodeposition [308]. While in solvothermal methods ZnO nanosheets can form - in principle - on virtually any substrate material, electrodeposition is only feasible on conductive substrates, e.g. indium tin oxide (ITO) on glass [295, 302, 306].

In an alternative solution-based approach, pure Zn substrates or foils are directly oxidized in solution to form ZnO nanosheets [294, 301, 311]. In this case, all Zn atoms are supplied by the substrate and oxidized via dedicated oxidation agents such as ethanol or direct bubbling of oxygen gas through the growth solution. Similar to the previous growth techniques, nanosheet formation is often guided by the presence of surfactants as described above [294].

Besides these wet chemical growth methods, ZnO nanosheets have also been fabri-
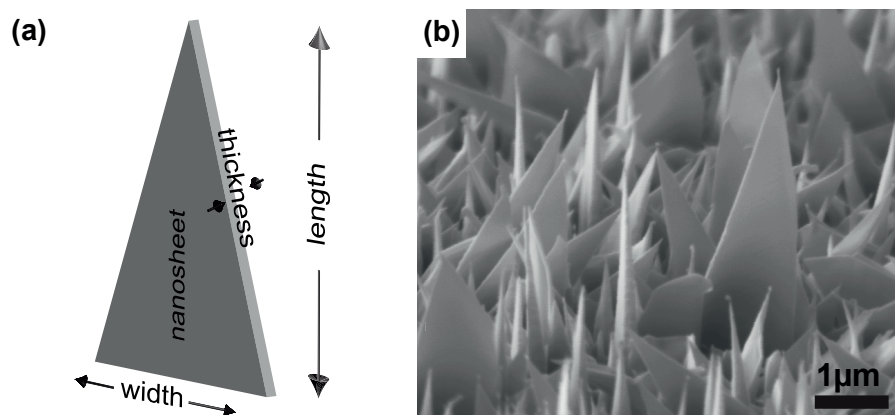
Figure 2.21: Schematic illustration (a) of a triangular ZnO nanosheet denoting its dimensions. SEM image of ZnO nanosheets grown by PLD in the course of this work.

cated by physical vapour deposition (PVD) techniques, including VPT [136, 137, 303, 304, 317–319], PLD [118, 305] and molecular beam epitaxy [320] with and without the use of a metal catalyst. Although hexagonal nanodisk shapes have been demonstrated [321], the PVD-grown nanosheets usually show different morphologies, e.g. triangular shapes [303, 304, 317, 318]. In contrast to the hexagonal nanodisks, the large exposed surface of these structures is not the ZnO(0001) facet, but a low-energy plane such as $\{2\bar{1}\bar{1}0\}$ or $\{01\bar{1}0\}$. The ZnO[0001] direction is often perpendicular to the sheet edges and growth proceeds via an initial formation of ZnO nanocombs with dendritic sidebranches (cf. the previous subsection). When ZnO growth is then continued beyond the formation of nanocombs, the spaces between the branches are filled up with impinging material and the comb side of the structure is smoothened out to form a nanosheet [317]. Zhang et al. could directly observe this type of nanosheet formation by an *in-situ* environmental SEM growth technique [319]. However, the formation of ZnO nanosheets has also been observed without the presence of nanocombs during the initial stage of ZnO growth as is the case in this work [118, 318, 320].

ZnO nanosheets can also be fabricated by a combination of the growth techniques mentioned above. In a first step, precursor nanosheets of pure Zn or Zn-containing material are synthesized in the desired shapes by, for example, VPT or hydrothermal methods [297, 322–324]. Subsequently, the nanostructures are oxidized via thermal annealing in oxygen or air, thus transforming the precursor structures to ZnO nanosheets of nearly identical shapes. Moreover, porous ZnO nanosheets have been fabricated using this approach [307, 323]. In a template-assisted method, nanosheets of zinc hydroxide nitrate hydrate (ZHNH) have been first prepared by electrodepositing the precursor material in

the spaces between polystyrene colloids [325]. Then, the polystyrene template has been removed under calcination at 600°C, simultaneously transforming the ZHNH to porous ZnO nanosheets via oxidation.

Potential applications of ZnO nanosheets include the common areas of ZnO nanostructures such as field emitters [303, 309], biosensors (e.g. for the detection of superoxides) [302, 326, 327] and dye-sensitized solar cells [314, 328, 329]. For the latter type of application, the average conversion efficiency of dye-sensitized solar cells prepared with ZnO nanosheets has been reported superior to devices based on ZnO nanowires [167]. ZnO nanosheets can also be utilized as anodes in lithium ion batteries showing improved performances compared to commercial ZnO powders [307]. Moreover, enhanced photocatalytic properties have been demonstrated for ZnO nanosheets, accelerating the degradation of organic dyes such as Rhodamine B or methyl orange [296, 298, 307, 330]. Thereby, the performance of ZnO nanosheets has been found superior to the photocatalytic degradation properties of ZnO nanorods [331]. Furthermore, ZnO nanosheets have been shown to emit light in the UV wavelength range, similar to the previously described ZnO nanostructure morphologies [300]. However, due to the ordered hexagonal perimeter of disk-like ZnO nanosheets, whispering gallery modes can be excited in the structure, leading to increased emission of UV light at the edges of the nanodisks [303, 321].

2.3.8 Other nanostructures

In the previous subsections a selection of ZnO nanostructures including the most common morphologies has been discussed in detail. However, additional, less common and hierarchical nanostructures have been reported in the literature, including "nano-aeroplanes" [249], 'nano-sleeve fishes" [290],"nano-propellers" [24],"nano-bowling pins" [4] and others. A detailed discussion of all these different types of ZnO nanostructures is beyond the scope of this work. For further information on less common or as well as hierarchical types of ZnO nanostructures, the reader is referred to various reviews and articles available in the literature [3–5, 278].

Chapter 3

Experimental techniques

In this chapter, the experimental techniques employed for the fabrication and characterization of the ZnO nanostructures and thin films discussed in this work are briefly described.

3.1 Pulsed laser deposition

This energy-enhanced growth technique belongs to the group of PVD methods and is widely used for the deposition of thin films. A pulsed laser beam evaporates the desired growth material from a target which then condenses on a substrate placed opposite of the target. Due to the high energy of the focused laser beam, material ablation is nearly congruent, i.e. the evaporated species exhibit almost the same stoichiometry as the bulk target material [332]. This renders PLD a versatile growth technique which can be used to deposit films of various materials including metals, semiconductors and polymers [332, 333]. Due to possibility for controlled streaming of oxygen gas into the growth chamber, PLD is especially suitable for the deposition of high-quality oxide films [334,335]. For further reading on the fundamental principles as well as applications of PLD, the reader is referred to the books by Chrisey or Eason [335, 336].

Besides thin film growth, the fabrication of various nanostructures has been demonstrated by PLD [337–341]. For these applications, the setup of the PLD system is often slightly modified, for example, by enabling higher pressures within the 1 - 100 mbar range [337, 342] or by utilizing indirect heating via a hot-wall deposition chamber similar to a tube furnace [155, 341]. However, when appropriate growth conditions are chosen, nanostructure fabrication is also feasible in conventional PLD systems designed
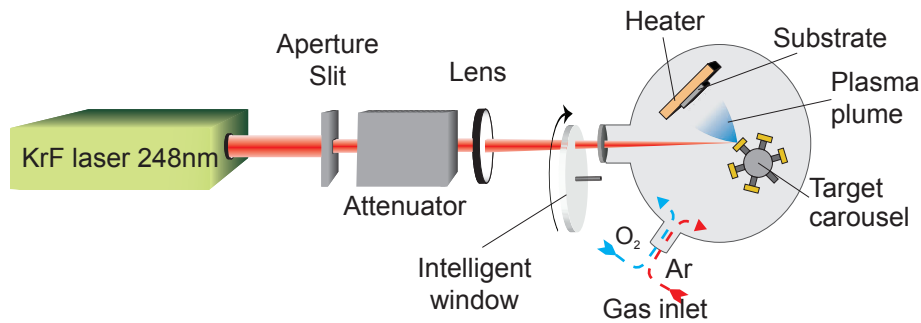
Figure 3.1: Schematic diagram of the PLD setup used in this work.

for thin film deposition [343].

The PLD setup used for the growth of ZnO nanostructures and AZO thin films in this work is a conventional thin film deposition system shown schematically in Fig. 3.1. A pulsed laser beam is generated in a KrF excimer laser (Lamda Physik 210i) operating at a wavelength of 248 nm. In this type of lasers, stimulated emission is achieved by the formation of temporary bonds between inert krypton and fluorine in an excited state via electrical discharge at voltages between 16 kV and 24 kV. Within nanoseconds, the molecule dissociates again into its elemental atoms under the emission of a photon. The generated laser beam is guided by a set of mirrors through a rectangular aperture which controls the size and shape of the laser spot on the target. Further down the path, the beam passes through an attenuator enabling the adjustment of the laser energy at a constant discharge voltage. Thereby, the energy of the beam can be controlled without changing the spot size of the laser beam on the target as has been observed for voltage-controlled laser energy adjustments [344]. Subsequently, the beam is focussed by a lens through a set of viewport windows onto a target situated in an ultra-high vacuum chamber. The viewport window system ("Intelligent window", PVD Products Inc.) consists of an outer fixed window coated with an anti-reflection layer and an inner rotatable fused silica disc. The latter part is denoted schematically in Fig. 3.1. During extensive material ablation, the inner disc is coated unintentionally with evaporated target material, essentially attenuating the laser energy inside the chamber. When the energy reduction reaches a critical value, the inner disc can be rotated to a clean spot, allowing for longer maintenance intervals of the viewport. In order to minimize deviations in the laser energy between deposition runs, energy readings both before and after entrance of the beam into the growth chamber have been recorded, serving as an energy reference.

As the laser hits the target, material is rapidly evaporated with a net motion normal to the

46
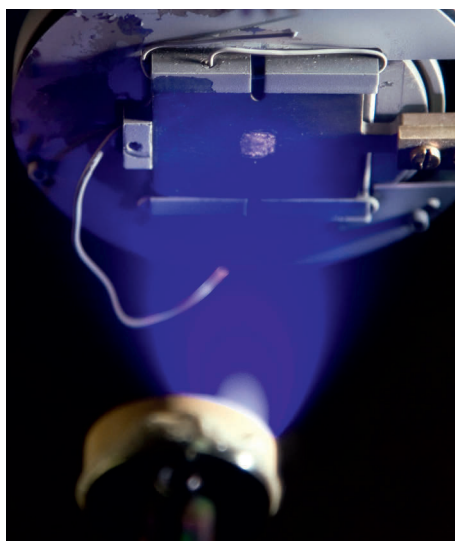
Figure 3.2: Plasma plume during laser ablation of a ZnO target in the PLD system employed in this work.

target surface. Subsequently, the ablated atoms are ionized by the incident laser beam, generating a bright blue plasma plume as shown in Fig. 3.2. For the case of ablation from a ZnO target, this plume consists of neutral ZnO, Zn and O atoms as well as ions, ZnO clusters and zinc suboxides [345–348]. At a given distance opposite to the target - the so-called target-to-substrate distance - a substrate is mounted on a heater block in an *on-axis* configuration, i.e. facing the target surface. As the ablated species impinge on the heated substrate surface, condensation occurs and ZnO crystal growth is nucleated. In order to avoid instabilities in the material flux due to the formation of ablation cones on the target surface [349], the target is raster-scanned in a circular area of 15 mm diameter during deposition. Furthermore, the target is pre-ablated extensively prior to deposition for contamination removal imposed by the polishing of the target surface usually performed before every other deposition run.

The deposition chamber is equipped with two independent gas inlets and mass flow controllers, allowing for controlled gas flows into the chamber at distinct ratios of argon and oxygen. A stable absolute pressure in the range of 0.001 mbar to 0.5 mbar inside the reaction chamber is then reached by adjusting the valve opening to the vacuum pumps.

For the growth of ZnO nanostructures, a pure ZnO target was used and the energy of the laser was adjusted to 1-2 J/cm^2 at discharge voltages between 16-24 kV. The substrates

were heated to temperatures between 700°C and 800°C with ramp rates of 10-15°C/min in 0.5 mbar of 95% Ar: 5% O_2 or pure oxygen ambient gas.

For the deposition of AZO thin films, a ZnO target containing 2 wt% Al was ablated with laser energies of 1-1.6 J/cm^2. Pure Ar and oxygen ambients at pressures between 0.001 and 0.5 mbar are maintained in the chamber during deposition. Substrate temperatures are varied from room temperature up to 500°C. The target-to-substrate distance was kept at 45 mm for all depositions.

3.2 Electron Microscopy

For the structural characterization of nanostructures, electron microscopy is one of the most important tools as it provides direct imaging of the nanostructures' morphology. The resolution of electron microscopy techniques reaches far beyond the resolution limit of optical microscopes due to the shorter (de-Broglie) wavelengths of electrons compared to those of photons [350]. In an electron microscope, a beam of electrons is directed towards a specimen, where it interacts with the sample material in multiple ways as illustrated in Fig. 3.4. In scanning electron microscopy (SEM), secondary electrons are mainly exploited to create an image of the specimens' surface topography, while in transmission electron microscopy (TEM), primary electrons transmitted through a thin sample slice are responsible for image contrast. For further reading on electron microscopy techniques, various comprehensive textbooks are available [350–352]

3.2.1 Scanning Electron Microscopy

In a typical SEM setup shown schematically in Fig. 3.3, electrons are first generated within an appropriate electron source such as a tungsten filament or a field emission gun. The electrons are accelerated towards the sample by large electric fields (in SEM typically about 10 kV). It governs the momentum of the electrons and is therefore directly related to their de-Broglie wavelength $\lambda = h/p$ which is an important factor for determining the resolution of the microscope. The accelerated electrons pass through a set of electromagnetic lenses and scan coils which focus and deflect the beam across the surface of the specimen. The impinging electrons are scattered by the atoms and molecules in the sample, resulting in several interaction "products" as mentioned above (cf. Fig. 3.4). The secondary electrons (SE) produced via inelastic scattering at the sample surface are the main signal source in SEM. By scanning the electron beam across the specimen, the number of secondary electrons collected in a detector is recorded at
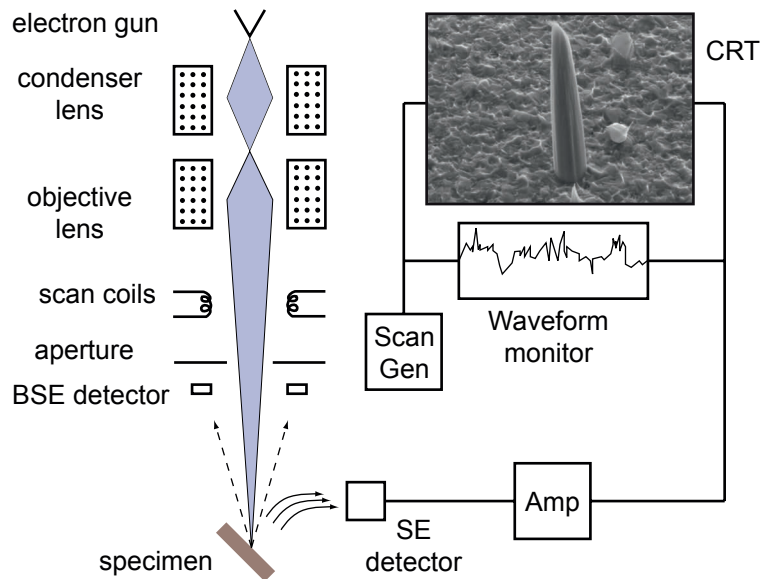
Figure 3.3: Schematic illustration showing the main components of a basic SEM setup. *Adapted from [350].*

each position (pixel) and, subsequently, assembled into a full image of the sample surface. Thereby, the emission and detection efficiencies of secondary electrons are directly correlated with the surface morphology of the sample.

Besides secondary electrons, characteristic x-rays and Auger electrons are generated by interaction between electron beam and sample as illustrated in Fig. 3.4. The incident electrons can transfer some of their energy to an atom in the specimen and knock out an electron from an inner shell. Subsequently, an electron from an outer shell can relax into the empty low-energy state and release the energy difference via the emission of an x-ray or Auger electron. Since the energies of these x-rays or Auger electrons are characteristic for the atomic species and electron transitions involved, additional information about the chemical composition of the specimen can be gathered by energy-resolved detection of these x-rays or Auger electrons. These characterization techniques are called energy- or wavelength-dispersed x-ray spectrometry (EDS or WDS) and Auger Electron spectroscopy (AES), respectively.

In addition to the processes described above, electrons can also be "backscattered" from the sample surface (cf. 3.4). Thereby, the number of back-scattered electrons (BSE) depends on the scattering cross-section and the atomic number Z of the species in the
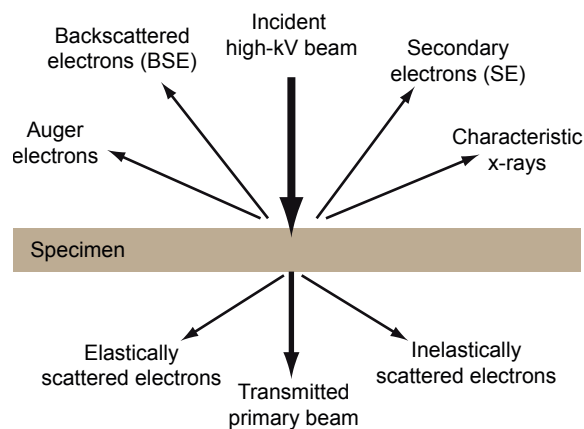
Figure 3.4: Various interaction mechanisms of an electron beam with a specimen. *Adapted from [352].*

sample. When collected in a detector and overlaid with secondary electron images, backscattered electrons can give additional Z contrast to the images, revealing the positions of heavy and light atoms in the sample surface.

Specimen under SEM investigation are subject to heavy electron bombardment. If not dissipated properly, e.g. on insulating samples, electrons may therefore accumulate and cause charging at the surface. The resulting electric field interferes with the incident and secondary electrons and distorts the recorded image. In order to avoid this issue, samples are generally mounted to a grounded sample stage with conductive carbon or copper tape. As an additional measure, the charge dissipation of insulating samples can be enhanced by coating the surface with thin Au or carbon films on the order of a few nanometers. These coatings allow for sufficient charge dissipation while the surface features of interest are retained.

The SEM work during this study was carried out at a Zeiss Ultra 55 Limited Edition, a Zeiss Supra 55 VP and a Hitachi S-5500 in-lens system, operating at acceleration voltages of 5 - 15 kV.

3.2.2 Transmission Electron Microscopy

While SEM is a widely used method for relatively fast and easy assessment of a specimens' surface morphology, TEM allows for a more detailed characterization with resolutions down to the atomic level. Information on the local crystal structure, crystal
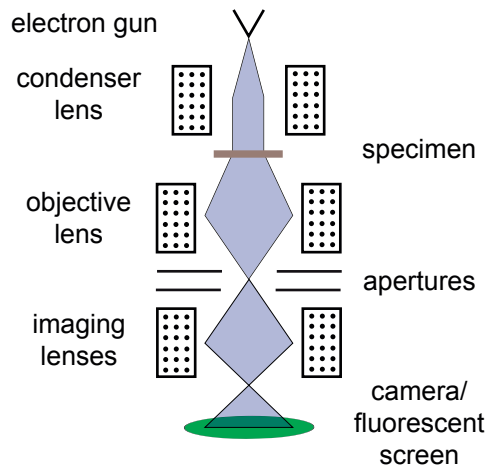
Figure 3.5: Schematic illustration showing the main components of a basic TEM setup. *Adapted from [350–352].*

orientation as well as lattice defects can be gathered.

As mentioned above, a beam of primary electrons transmitted through the specimen is utilized for image formation in TEM rather than the secondary electrons used in SEM. Nevertheless, the basic setup of a TEM shows similarities to SEM (cf. Fig. 3.5). At the top of the columns, electrons are generated within a suitable source and guided towards the specimen by electromagnetic condenser lenses. Contrary to SEM, the electrons are not focussed on the sample, but penetrate the specimen as a parallel beam. Sets of apertures and electromagnetic objective and projector lenses guide the transmitted electrons onto a fluorescent screen or a CCD detector for image recording. In order to ensure the transmission of electrons through the specimen, acceleration voltages on the order of few hundred kV and sample thicknesses of typically less than 100 nm are necessary. Therefore, sample preparation for TEM studies can be a difficult task with numerous processing steps including focused ion beam processing or sputter etching. Nanostructure specimen, however, can be easier to prepare since nanoscale dimensions are - by definition - immanent to nanostructures. Therefore, a simple dispersion of the nanostructures on a conductive carbon or copper mesh may often be sufficient for basic TEM studies.

Transmission electron microscopes can be operated in different modes, revealing distinct properties of the specimen. A typical image recorded in bright-field mode is shown in Fig. 3.6a. The image contrast is formed by absorption and scattering of electrons in the sample and is therefore sensitive to local variations in specimen thickness and/or atomic number Z. Furthermore, the "Bragg" scattering of electrons caused by atoms in a periodic crystal lattice can be exploited for image formation. As will be described in
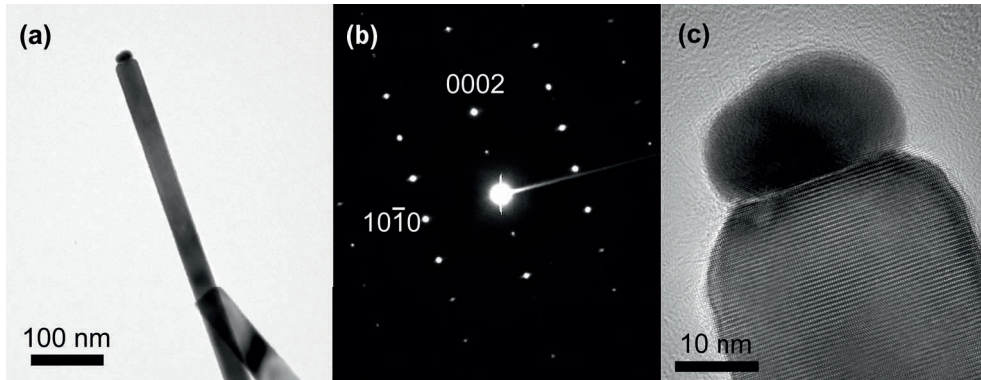
Figure 3.6: Example images of a ZnO nanowire recorded in the course of this work with different imaging modes of TEM. (a) Bright-field image, (b) selected-area diffraction pattern and (c) HRTEM image.

more detail for the case of x-rays in section 3.4, an incident electromagnetic wave with wavelength λ is diffracted at crystal lattice planes if the so-called "Bragg condition" (cf. equation 3.1) is satisfied. By spatially-resolved detection of the diffraction maxima, i.e. by recording a diffraction pattern (cf. Fig. 3.6b), information on the specimens' crystal lattice and phase as well as growth directions (of nanostructures) can be revealed. By inserting an aperture in the transmitted beam path, such diffraction patterns can be recorded only from a selected area of the specimen (selected-area electron diffraction, SAED).

The resolution of TEM can be improved even down to the atomic level when operated in high-resolution mode (HRTEM). In this mode, image contrast is created through the phase shift between an electron wave transmitted directly through the specimen ("forward-scattered" wave) and a diffracted electron wave [351]. While the former serves as a reference phase, the diffracted wave contains information about the atom arrangement in the specimen. A HRTEM image can therefore be considered as an interference pattern of diffracted and incident electron waves. In the resulting image individual atomic columns within the specimen can be visualized as shown in Fig. 3.6c, enabling detailed studies of local variations in the crystal structure, revealing lattice defects such as stacking faults and allowing for investigations of nanostructure growth directions and interfaces.

In this work, a JEOL 2010F TEM operating at 200kV was used to study the structural details of individual ZnO nanostructures. Corresponding specimen were prepared by scraping the nanostructures off the as-grown substrate and dispersing them on a conductive carbon mesh by dripping ethanol over the scalpel tip.
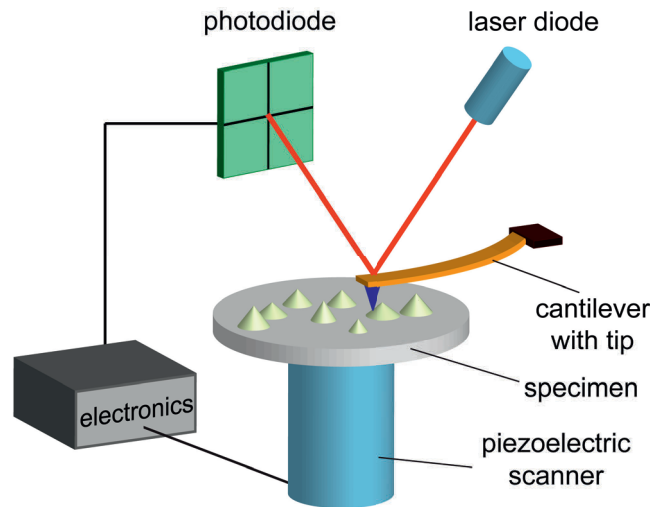
Figure 3.7: Schematic illustration of a basic AFM setup. *Adapted from [353].*

3.3 Atomic Force Microscopy

As a member of the family of scanning probe microscopes, the atomic force microscope (AFM) is used to reveal information about the surface of a specimen. In the typical application of AFM, the topography of a specimen surface is imaged. However, various other characteristics such as magnetic, frictional or electrical forces can also be probed if the AFM setup is modified appropriately and suitable probe tips are used [353]. In this work, the acquisition of surface topography images was the primary use of AFM. Detailed information on AFM can be found in various reviews and textbooks [353–355]

In Fig. 3.7 a typical AFM setup is illustrated schematically. The operation principle of an AFM is based on the raster scanning of a sample surface with an atomically sharp probe tip, which is mounted to the end of a flexible cantilever. As the tip approaches the specimen, the sample surface interacts with the probe tip via attractive or repulsive forces, leading to a deflection of the cantilever from its rest position. This deflection is monitored by the displacement of a laser beam reflected off the cantilever using a photodiode. From the recorded data, the forces acting on the tip can be determined and converted to the parameters of interest (e.g. topography). Typically, the probe tip is scanned across the sample surface by moving the sample stage with a piezoelectric scanner. In principle, an AFM can operate in two feedback modes: the constant height and the constant force mode. In the former, the distance between tip and sample is kept constant and information about the forces exerted on the tip and the surface topography

is contained in the measured deflection of the cantilever. In contrast, a feedback loop is used in the constant force mode to adjust the height of the sample by the piezoelectric stage, thereby maintaining the forces acting on the tip. Information on the surface topography is then directly given by the vertical positions of the piezoelement at each measurement point (pixel).

Images of the sample surface topography can be recorded in different AFM operation modes. In the *non-contact* mode, the tip and cantilever are driven in a vertical oscillatory motion close to the resonance frequency of the cantilever. As the probe tip approaches the sample surface, the phase and amplitude of the cantilever oscillation are slightly changed due to the tip-sample interaction forces and these shifts can then be converted into a force value. In this operation mode almost no damage is inflicted to the sample surface as it is nearly contact-free. In the second operation mode - the *contact* mode - the probe tip is continuously in contact with the sample surface during image scanning and the interaction forces are directly measured by the deflection of the cantilever. The sample surface might therefore be damaged as the tip is "dragged" across the sample. Additionally, the increased wear of the probe tip reduces its lifetime and requires frequent replacement intervals.

The AFM images presented in this work have been acquired using a Veeco Multimode AFM operating in non-contact mode and controlled by a Nanoscope V unit.

3.4   X-Ray Diffractometry

The distances between atoms periodically arranged in a solid crystal are typically on the order of few Ångström. In order to probe such a crystal by electromagnetic radiation, wavelengths on the same order of magnitude or lower are necessary. In 1913, W.H. Bragg and his son discovered that x-rays reflected off a crystalline solid showed distinct intensity maxima at particular angles and attributed their observations to the constructive interference of x-rays diffracted by sets of parallel crystal lattice planes separated by a distance d [356]. For radiation to interfere constructively, the difference in path lengths of the individual rays reflected off the lattice planes must be an integer multiple of the wavelength λ as shown in Fig. 3.8. In the case of two adjacent lattice planes, this difference is equal to $2dsin\theta$ with θ being the incidence angle of the x-rays. Merging these considerations, the condition for the observation of intensity maxima in x-ray diffraction can be written as

$$n\lambda = 2dsin\theta \tag{3.1}$$

$$\Delta_1 + \Delta_2 = 2d\ \sin\theta = n\lambda$$
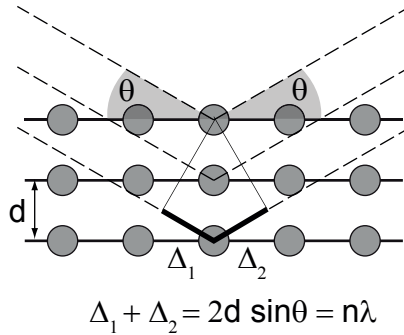
Figure 3.8: Schematic illustration of the Bragg condition. *Adapted from [357].*

which is known as Bragg's law. X-ray diffraction techniques can therefore be used to reveal information about various different properties of crystalline samples, e.g. chemical composition, crystal structure, lattice parameters as well as lattice stress and crystal grain sizes. A detailed and thorough discussion of x-ray diffraction can be found in the book by Birkholz [357].

In this work, a Bruker AXS D8 Discover high-resolution XRD system was used for all x-ray diffraction measurements. It consists of a fixed Cu K_α x-ray source with a monochromator, a goniometer and sample stage with in total six degrees of freedom as well as a movable x-ray scintillation detector arm with a set of collimating and anti-scattering slits. The goniometer is free to move by an azimuthal rotation around its axis corresponding to the angle θ, and by a vertical tilt of angle ψ (cf. Fig. 3.9a). The height and lateral positions of the specimen are controlled by electrical drives on the sample stage, which can also be rotated azimuthally around its center axis by an angle ϕ.

The specimen is mounted directly to the sample stage of the goniometer and held in position using either a vacuum chuck or double-sided tape. In both cases, the sample is unlikely to lie flat on the stage and a corresponding θ offset correction is necessary during the alignment steps of the measurement procedure.

In an XRD measurement, the angle θ of the incident x-ray beam is controlled by the azimuthal rotation of the goniometer. In order to detect x-rays reflected off a lattice plane, the detector arm is rotated around the goniometer axis to the angle 2θ. In general, an x-ray diffraction measurement can be set up in various ways, revealing various properties of the crystalline sample. The two measurement modes employed in this work are briefly introduced in the following sections.
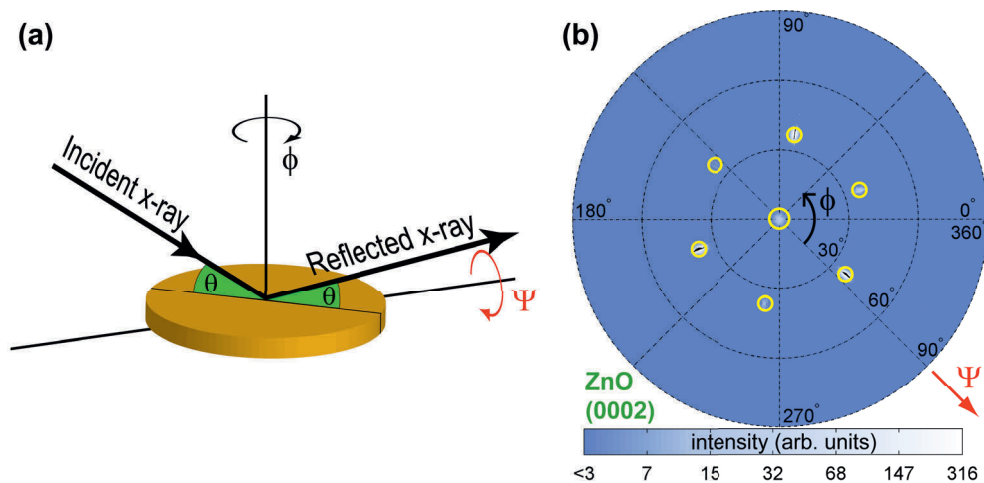
Figure 3.9: (a) Schematic illustration of the available rotational degrees of freedom for the goniometer/sample stage in a XRD measurement setup. (b) XRD pole figure of a sample with tilted ZnO nanowires growing along the ZnO[0001] direction. During the pole figure measurement, the sample is azimuthally rotated by $360°\,\phi$ for each step in the vertical tilt ψ. The angle θ is fixed at the position corresponding to reflections at the ZnO(0002) planes. The intensity at each measurement position is given by the color index below the figure (the peaks in the plot are denoted by yellow circles). For clarity, the font colors of the corresponding angles are matched in parts (a) and (b).

θ - 2*θ* **measurements**

This mode is one of the basic and most common measurement types in x-ray diffraction. After initial alignment and positioning of the sample for optimized collection efficiencies, the stage drives remain fixed. Intensities of reflected x-radiation are recorded for a desired range of *θ* and 2*θ* angles while the relationship between *θ* and 2*θ* is maintained. Each observed peak corresponds to the reflection of x-rays at a set of planes perpendicular to the sample surface. The resulting spectra therefore reveal information about the crystal structure, thin film texture and grain size as well as the lattice constant/interplanar spacing *d*.

Pole figure measurements

The aim of this measurement mode is to study the orientations of a single set of lattice planes within the specimen. Thus, fixed values for *θ* and 2*θ* are chosen that satisfy the Bragg condition for the desired crystal planes, e.g. the ZnO(0002) planes. After the initial alignment procedures, the reflected intensity is recorded for changes in the vertical tilt ψ and the azimuthal rotation of the sample stage ϕ. In a typical experiment, one of the two parameters, e.g. ψ, is fixed as the other one (ϕ) is cycled through its full range. The process is then repeated for the next step in ψ until the full range of desired ψ data points is reached. The acquired intensity data can then be plotted as a "pole figure" vs. the tilt and rotation angles ψ and ϕ as illustrated in Fig. 3.9b. Applying this measurement mode to thin films, information about the degree of texture, the distribution of crystal phases and - if appropriate film and substrate lattice planes are studied - the epitaxial relationship between the substrate and the thin film can be obtained from the recorded data. When combined with imaging techniques such as SEM, pole figures are a powerful tool for revealing the orientation and epitaxial relationships of nanostructures with a substrate as will be demonstrated in Paper III.

3.5 Electrical characterization of thin films

The potential of a thin film for use as a transparent electrode clearly depends on its electrical properties, i.e. its resistivity, mobility and carrier concentration. For semiconductors, these properties can be measured by utilizing the Hall effect, i.e. the generation of a transverse voltage due to the Lorentz force

$$\vec{F} = q(\vec{E} + \vec{v} \times \vec{B}) \tag{3.2}$$
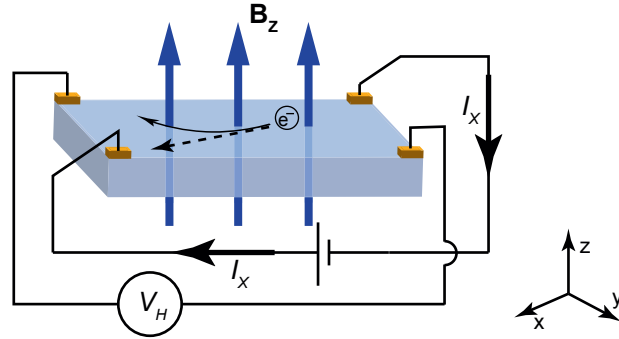
Figure 3.10: Schematic illustration of the Hall effect. The shown square-shaped van der Pauw geometry has been used for Hall effect and sheet resistivity measurements in this work. *Adapted from [358].*

exerted on moving electrons by a magnetic field $\vec{B}$. Here, q is the electric charge, $\vec{E}$ is the electric field strength and $\vec{v}$ is the velocity of the charge carriers. Fig. 3.10 illustrates the fundamental aspects of the Hall effect, if electrons are the majority charge carriers in the semiconductor. When an electric field E_x is applied along the x-axis, electrons drift through the material and cause an electric current I_x. With the magnetic field B_z in the z-direction, the Lorentz force induces an additional charge drift along the y-axis. The resulting current I_y leads to charge accumulation at the edges of the conductor, building up a transverse electric field E_y that counteracts I_y and cancels the Lorentz force [358]. Upon reaching equilibrium conditions, I_y vanishes and a potential difference

$$V_H = -\frac{B_z I_y}{ned} \tag{3.3}$$

can be measured across the semiconductor known as the *Hall voltage*. Here, n is the carrier concentration, e the elemental charge and d the thickness of the conductor slab as denoted in Fig. 3.10. This leads to the Hall coefficient defined as

$$R_H = \frac{E_y}{j_x B_z} = \frac{V_H d}{I_x B_z} = -\frac{1}{ne} \tag{3.4}$$

Therefore, by measuring the Hall voltage at constant magnetic field B_z and forward current I_x, the carrier concentration n as well as the type of majority charge carriers (given by the sign of equation 3.4) can be determined. Additionally, if the resistivity ρ of the thin film is known, the electron mobility μ_e in the sample can be calculated using the relation

58

$$\mu_e = \frac{\sigma}{ne} = \frac{1}{ne\rho}. \qquad (3.5)$$

A commonly employed method for determining the resistivity ρ of a thin film with arbitrary geometry is the van der Pauw method [358, 359]. The thin film is contacted at four points at the edges of the sample and ρ is evaluated by a series of $I - V$ curve measurements with appropriate contact configurations for current-injection and voltage-measurement. Simultaneously, the Hall coefficient R_H can be measured using the same geometry by applying a magnetic field B_z.

In this work, van der Pauw measurements have been carried out on AZO thin films using a Lakeshore 7504 system. A square-shaped sample geometry with contacts in the four corners has been utilized as depicted schematically in Fig. 3.10. For the Hall voltage measurements, the forward current has been fixed at $I_x = 1$ mA with the magnetic field sweeping from -0.5 T to 0.5 T in steps of 0.1 T. Prior to the actual measurement, the ohmic behaviour of the contacts has been confirmed by $I - V$ curve measurements over various contact configurations.

3.6   Optical characterization

Besides low resistivity, the transmission of light within the desired wavelength range is a key feature of transparent electrodes. For thin films on a transparent substrate such as glass or sapphire, the optical transmittance of the electrode layer can be measured directly using appropriate light sources, monochromators and spectrometers (e.g. UV-Vis spectrometers). However, this approach cannot be employed with transparent conducting films grown directly on opaque substrates or functional layers, e.g. for use as top electrodes. In these cases, spectroscopic ellipsometry can disclose the properties of interest.

In ellipsometry, changes in the polarization of light after interaction with and reflection from a specimen are measured. In a typical setup (cf. 3.11), a beam of light with a defined polarization is incident on the sample surface at a distinct angle (typically 70°) [361]. The reflected light passes through a polarization filter and its intensity is measured in a detector.

The experimental data obtained from a spectroscopic ellipsometry measurement contains information from all layers and interfaces the light interacts with, including the substrate, the thin film as well as the substrate-film and film-air interfaces. Therefore, meaningful interpretation of ellipsometry measurements is not straight-forward and typically requires
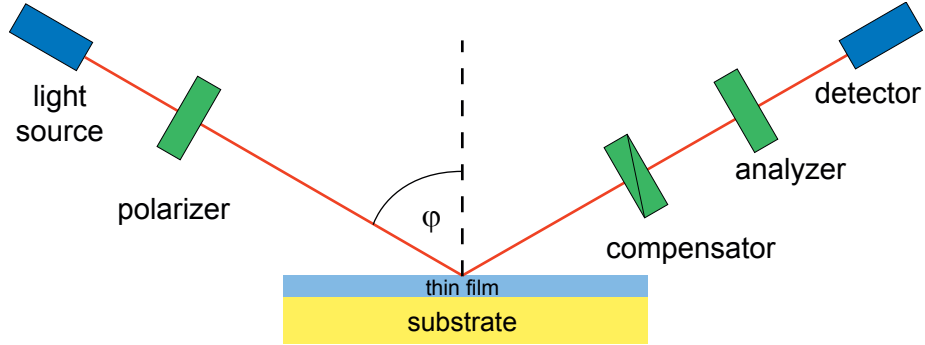
Figure 3.11: Schematic illustration of a typical ellipsometry setup. *Adapted from [360].*

modelling of the acquired data, taking into account the different layers and interfaces on the sample. Furthermore, structural and electrical properties of the films such as crystallinity and the concentration of free charge carriers can influence the selection of a suitable model [361]. Once a model is fitted to the data, the complex refractive index $N = n + i\kappa$ can be calculated for the layer of interest. Here, the real part n is the real refractive index and the imaginary part κ is the extinction coefficient. The optical transmittance of the thin film can then be determined from the relation [362, 363]

$$T = \frac{I}{I_0} = e^{-\alpha d} \tag{3.6}$$

where I and I_0 are the transmitted and incident intensities, d is the film thickness and α is the absorption coefficient which is related to the extinction coefficient κ via

$$\alpha = \frac{4\pi\kappa}{\lambda} \tag{3.7}$$

with λ as the wavelength of the transmitted light [362].

The layer stack used to model the AZO thin films grown on GaAs substrates by PLD is shown schematically in Fig. 3.12. It consists of a top roughness layer (effective media approximation with 50% ZnO, 50% void material), a general oscillator layer representing the AZO thin film, and the GaAs substrate with a thin native oxide layer. The AZO layer was fitted using a combination of a Tauc-Lorentz oscillator and a Drude model. The former oscillator works well with amorphous crystal structures which are to be expected in this work due to the room temperature growth of AZO films [361]. The Drude oscillator model accounts for the absorption of light caused by the high charge carrier concentrations observed in the AZO films ($\sim 10^{20}$ cm^{-3}) [361].
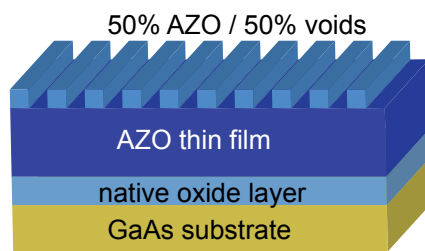
Figure 3.12: Schematic illustration of the AZO/GaAs layer stack used for the modelling of the ellipsometry data.

Chapter 4

The papers

Paper I

Effects of substrate annealing on the gold-catalyzed growth of ZnO nano-structures

Abstract. The effects of thermal substrate pretreatment on the growth of Au-catalyzed ZnO nanostructures by pulsed laser deposition are investigated. C-plane sapphire substrates are annealed *prior* to deposition of a thin Au layer. Subsequent ZnO growths on substrates annealed above 1200 °C resulted in a high density of nanosheets and nanowires, whereas lower temperatures led to low nanostructure densities. Separate Au film annealing experiments at 700 °C showed little variation in the size and density of the Au catalyst droplets with substrate annealing temperature. The observed variation in the density of nanostructures is attributed to the number of surface nucleation sites on the substrate, leading to a competition between nucleation promoted by the Au catalyst and surface nucleation sites on the rougher surfaces annealed below 1200 °C.

Effects of substrate annealing on the gold-catalyzed growth of ZnO nanostructures

Christian C Weigand[1], Daniel Skåre[2], Cecile Ladam[3], Jostein Grepstad[1] and Helge Weman[1*]

Abstract

The effects of thermal substrate pretreatment on the growth of Au-catalyzed ZnO nanostructures by pulsed laser deposition are investigated. C-plane sapphire substrates are annealed *prior* to deposition of a thin Au layer. Subsequent ZnO growths on substrates annealed above 1,200°C resulted in a high density of nanosheets and nanowires, whereas lower temperatures led to low nanostructure densities. Separate Au film annealing experiments at 700°C showed little variation in the size and density of the Au catalyst droplets with substrate annealing temperature. The observed variation in the density of nanostructures is attributed to the number of surface nucleation sites on the substrate, leading to a competition between nucleation promoted by the Au catalyst and surface nucleation sites on the rougher surfaces annealed below 1,200°C.

Keywords: zinc oxide, laser ablation, atomic force microscopy, thermal annealing, vapourliquid-solid growth, nanostructures; surface roughness, surface defects

Introduction

Semiconductor nanostructures have attracted great interest in the past decade due to a wide range of potential applications, e.g., in solar cells, lasers and sensors, and as building blocks of integrated systems [1-3]. Fabrication of different types of nanostructures, such as nanowires, nanorods, nanobelts and nanosheets can be achieved from a variety of methods, including solution-based, chemical and physical vapor deposition techniques, with and without the use of a metal catalyst [1,4-7]. The morphology and orientation of nanostructures can be controlled by tuning growth parameters such as the substrate temperature, background pressure and precursor flux, as well as the substrate material. Furthermore, substrate treatments like chemical etching and thermal annealing have been shown to have significant impact on nanostructure growth for solution-based and catalyst-free vapor deposition techniques [8-11]. For catalyst-assisted nanostructure growth, however, little information exists on the effects of substrate pretreatment *prior* to catalyst metal deposition [12]. Moreover, reports on pretreatment by thermal annealing often refer to substrates coated with a thin layer of the

catalyst metal, resulting in alloying and formation of catalyst droplets, which serve to guide the subsequent nanostructure growth [13-16]. Thermal annealing of clean substrates, however, is often reported to cause smooth and well-defined step-and-terrace substrate surfaces [17,18].

In this report, we show how thermal annealing of the substrate *prior* to catalyst metalization can significantly impact catalyst-assisted nanostructure growth. This is demonstrated for ZnO nanostructures grown on c-plane sapphire substrates by pulsed laser deposition (PLD) using gold as a catalyst.

Experimental work

The nanostructures were grown by ablation from a raster-scanned ZnO target using a 248-nm KrF excimer laser at 10 Hz repetition rate and a fluency of ~1.33 J/cm^2. The substrates were heated to 700°C in a 0.5 mbar ambient of 5% oxygen/95% argon and ZnO was deposited for 30 min. Prior to growth, the "epi-ready" c-plane sapphire substrates (Valley Design Corp., 0° ± 0.25° miscut) were annealed in oxygen at 1,000, 1,200 and 1,400°C for 1 h, followed by deposition of a 1-nm-thin layer of Au using e-beam evaporation. No further annealing of the Au layer took place before introduction into the PLD chamber.

In order to investigate the effects of substrate annealing on the formation of Au catalyst droplets, separate

* Correspondence: helge.weman@iet.ntnu.no
[1]Department of Electronics and Telecommunications, Norwegian University of Science and Technology, 7491 Trondheim, Norway
Full list of author information is available at the end of the article

Springer

experiments were carried out in the PLD chamber with a Au layer only. C-plane sapphire substrates coated with a 1-nm-thin film of Au were annealed for 5 min at the same growth temperature and ambient as for the growth of ZnO nanostructures.

The clean and Au-coated substrates were examined using atomic force microscopy (AFM), and the PLD-grown ZnO nanostructures were studied with scanning electron microscopy (SEM).

The size and density of the catalyst droplets resulting from the Au layer annealing experiments were determined using the image processing software "ImageJ" [19]. The analysis procedure adopting image contrast enhancement, noise removal and particle separation by threshold and "watershed" methods was applied to 2μm × 2μm AFM images of the Au droplets. From subsequent automated particle measurements, the area, circularity, diameter and number density of the Au droplets were calculated.

Results and discussion

The topography of the as-received and annealed c-plane sapphire substrates and their characteristic parameters are shown in Figure 1 andTable 1 respectively. Both as-received substrates and those annealed at 1,000°C exhibit a rough surface morphology with scratches from the surface polishing provided by the manufacturer (Figure 1a, b). While the as-received substrates show no sign of a step-and-terrace structure, the onset of terrace formation is observed upon substrate annealing at 1,000°C with distinct steps of varying height (cf. inset in Figure 1b). By increasing the annealing temperature to 1,200°C (Figure 1c), the substrate surface becomes atomically flat, displaying an irregular step-and-terrace morphology with constant step heights of about 0.24 nm, corresponding to atomic bilayers [17]. After substrate annealing at 1,400°C, the step-and-terrace morphology shows a distinct anisotropy with terraces of comparable widths and nearly parallel edges (Figure 1d).

Figure 2 shows SEM images of the ZnO nanostructures grown on sapphire substrates annealed at these different temperatures. Under the growth conditions adopted here, tilted ZnO nanowires and nanosheets form with the latter being the predominant type and Au particles could be clearly identified at the tip of these structures, indicating catalyst-assisted growth [20]. The size and density of the ZnO nanostructures grown on as-received sapphire substrates (Figure 2a) and on those annealed at 1,000°C (Figure 2b) were noticeably inferior to those grown on substrates annealed at 1,200°C and above (Figure 2c, d), i.e., on substrates with a step-and-terrace surface morphology (cf. Table 1). The latter exhibit a high density of nanosheets and nanowires with significantly increased sizes. We note that the annealing temperature seems to
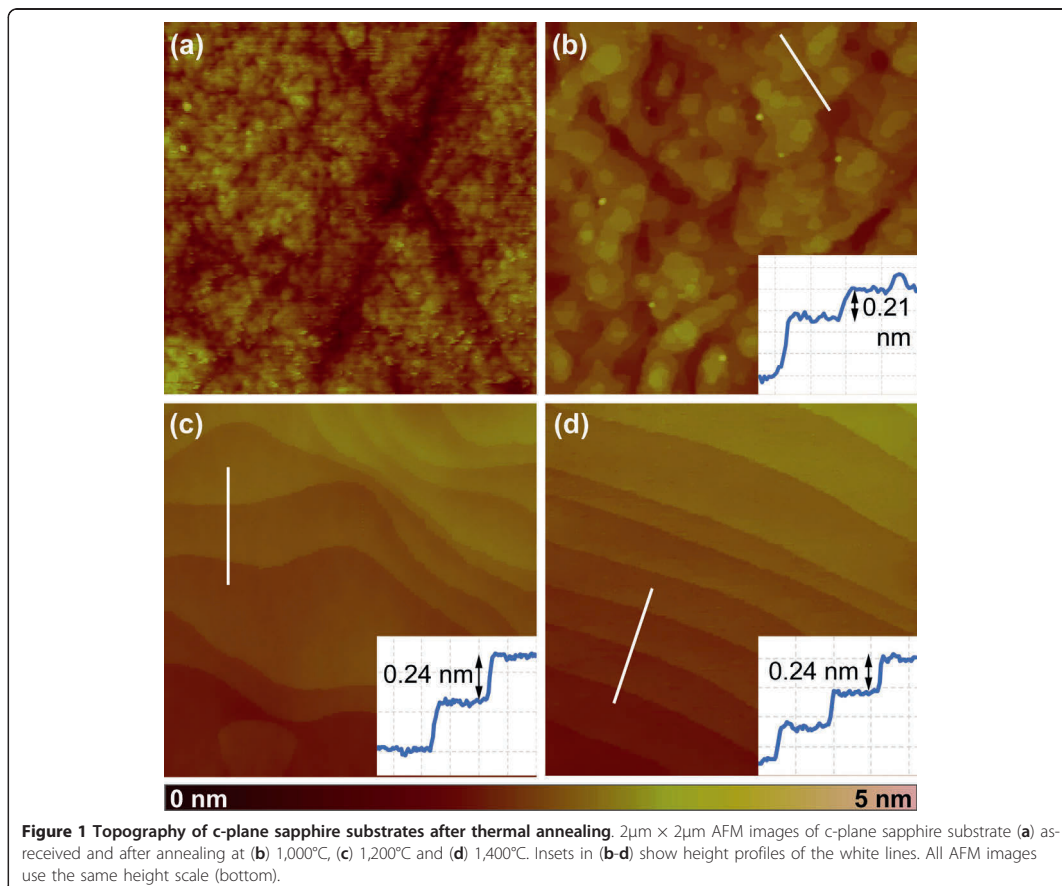
have no appreciable effect on the specific type of nanostructure grown. The observed differences in size and density could derive from two different parameters: (a) the size and density of the Au catalyst droplets and/or (b) the density of surface nucleation sites.

It has been reported that substrate pretreatment and morphology may significantly influence the size and density of Au catalyst droplets promoting nanostructure growth [12,21]. In order to investigate the effects of substrate annealing on catalyst droplet formation, Au-coated sapphire substrates were annealed in the PLD chamber at the 700°C growth temperature for 5 min, mimicking the adopted growth procedure prior to ZnO deposition. Before annealing of the Au layer, the step-and-terrace morphology of the substrate is still visible in AFM (Figure 3a). After annealing, the AFM images reveal a homogeneous distribution of Au droplets on the substrate surface regardless of the underlying step-and-terrace structure (Figure 3b). The size distribution and number density of the Au catalyst droplets are summarized in Table 1 and do not appear appreciably affected by thermal annealing of the substrate. Only for an annealing temperature of 1,400°C, we observe a slightly decreased average value and standard deviation of the droplet diameter as well as a higher number density of the Au droplets, presumably caused by the flat and smooth substrate topography [21]. We therefore conclude that the Au catalyst particle size is unlikely to bring about the observed differences in nanostructure size and density with substrate annealing temperature.

In the ideal scenario of catalyst-assisted nanostructure growth, the growth species are all incorporated into the nanostructure lattice via the catalyst-nanostructure interface. These species can reach the catalyst droplet either by direct impingement from the vapor or by surface diffusion from the substrate. In reality, however, the catalyst-nanostructure interface competes with nucleation at low-energy surface sites such as pits, craters and grain boundaries, as well as other surface defects abundant in rough surfaces [22-24]. At these surface sites, catalyst-free growth of ZnO is promoted, leading to reduced incorporation of growth species at the catalyst-nanostructure interface. Simultaneously, these surface sites also provide increased energy barriers for surface diffusion and thus imply reduced diffusion lengths of the adsorbed growth species [22].

From Figure 1, it is apparent that the number of surface nucleation sites promoting catalyst-free growth is large for substrates annealed at 1,000°C and below. For the step-and-terrace structures formed at higher annealing temperatures, however, the density of surface nucleation sites is significantly reduced. This is also indicated by the decrease in the measured surface roughnesses with annealing temperature listed in Table 1. In order to investigate the effect of surface nucleation sites, we have also deposited ZnO without the metal catalyst layer, but

Figure 1 Topography of c-plane sapphire substrates after thermal annealing. 2µm × 2µm AFM images of c-plane sapphire substrate (**a**) as-received and after annealing at (**b**) 1,000°C, (**c**) 1,200°C and (**d**) 1,400°C. Insets in (**b**-**d**) show height profiles of the white lines. All AFM images use the same height scale (bottom).

otherwise identical growth conditions and procedures. The SEM images displayed in Figure 4a and 4b, respectively, show that a high density of catalyst-free ZnO nanorods grows on the as-received c-plane sapphire, whereas only few rods nucleate on the substrate annealed at 1,200°C. This implies a higher density of nucleation sites on as-received c-plane sapphire substrates compared to those annealed at 1,200°C, thus promoting enhanced catalyst-free growth of ZnO nanorods. For substrates annealed at 1,000°C and below, catalyst-assisted growth of ZnO nanostructures may therefore be obstructed by the increased competition for growth species with catalyst-free ZnO growth nucleated at these surface sites, leading to the observed low density and reduced size of ZnO nanostructures. Conversely, the small number of surface nucleation sites on the atomically flat surfaces of substrates annealed at 1,200°C and above allows for the growth species to reach the Au droplets without being

Table 1 Characteristic features of substrates annealed at different temperatures and nanostructures grown on these substrates

Substrate anneal T (°C)	RMS roughness (nm)	Terrace width (nm)	Gold droplet size (nm)	Gold droplet density (cm^{-2})	Nanostructure density (cm^{-2})
As-received	0.46	N/A	24.5 ± 10.8	$7.3 \cdot 10^{10}$	$2.53 \cdot 10^{8}$
1,000	0.36	30-150	22.3 ± 10.2	$7.0 \cdot 10^{10}$	$4.21 \cdot 10^{8}$
1,200	0.24	100-700	24.0 ± 9.3	$6.8 \cdot 10^{10}$	$1.19 \cdot 10^{9}$
1,400	0.16	100-350	19.4 ± 6.5	$1.4 \cdot 10^{11}$	$9.87 \cdot 10^{8}$

Figure 2 ZnO nanostructures grown on annealed c-plane sapphire substrates. Top-view SEM images of ZnO nanostructures grown on c-plane sapphire substrates (**a**) as-received and annealed at (**b**) 1,000°C, (**c**) 1,200°C and (**d**) 1,400°C.

Figure 3 Morphology of annealed c-plane sapphire substrates before and after annealing of the Au catalyst layer. 2μm × 2μm AFM images of a 1-nm-thin Au layer on 1,200°C-annealed c-plane sapphire substrate before (**a**) and after annealing in the PLD chamber at 700°C for 5 min (**b**).

Figure 4 ZnO grown on as-received and annealed substrates without the Au catalyst. Tilted (45°) edge-on view SEM images of ZnO grown on c-plane sapphire substrates (**a**) as-received and annealed at (**b**) 1,200°C under identical growth conditions without the Au catalyst layer.

incorporated at surface nucleation sites, thus promoting the increased density and larger sizes of ZnO nanostructures.

Furthermore, it is obvious from Figure 4 that the rate of catalyst-free ZnO growth is significantly higher on the as-received substrate than on sapphire annealed at 1,200°C. It has been previously reported that high rates of catalyst-free, vapor-solid (VS) growth can obstruct the catalyst-assisted growth of oxide nanostructures due to competition between the two growth modes [25]. This provides further support for the scenario proposed in the present work.

Conclusion

In this study, we have shown that thermal annealing of the substrate prior to the Au catalyst deposition affects the density of ZnO nanostructures grown on c-plane sapphire. However, this substrate annealing does not seem to have a significant impact on the nanostructure morphology or the size and location of the Au catalyst droplets. The observed difference in nanostructure size and density can be explained by the competition between nucleation at the Au-ZnO interface and nucleation at low-energy surface sites associated with defects on rough substrate surfaces. The atomically flat surfaces obtained by high-temperature annealing promote formation of high densities of ZnO nanostructures through a significant reduction in surface nucleation sites, thus demonstrating the importance of smooth surfaces for catalyst-assisted nanostructure growth. We believe these findings will help improve control and understanding of catalyst-assisted nanostructure growth, also beyond the ZnO material system.

Author details

[1]Department of Electronics and Telecommunications, Norwegian University of Science and Technology, 7491 Trondheim, Norway [2]Department of Physics, Norwegian University of Science and Technology, 7491 Trondheim, Norway [3]SINTEF Materials and Chemistry, 7465 Trondheim, Norway

Authors' contributions

CW participated in the acquisition of scanning electron microscopy images, in the analysis and in the interpretation of the data and drafted the manuscript. DS carried out the growth of the zinc oxide nanostructures and the acquisition of atomic force microscopic and scanning electron microscopic data. He also contributed to data analysis. CL conceived and designed the study and participated in the analysis and interpretation of the data. JG participated in the coordination of the study and helped to draft the manuscript. HW participated in conceiving, designing and coordinating the study and helped in the writing process of the manuscript.

Competing interests

The authors declare that they have no competing interests.

References

1. Wang ZL: **ZnO nanowire and nanobelt platform for nanotechnology.** *Mat Sci Eng R* 2009, **64(3-4)**:33-71.
2. Lu W, Lieber CM: **Semiconductor nanowires.** *J Phys D Appl Phys* 2006, **39(21)**:R387.
3. Yan H, Choe HS, Nam S, Hu Y, Das S, Klemic JF, Ellenbogen JC, Lieber CM: **Programmable nanowire circuits for nanoprocessors.** *Nature* 2011, **470(7333)**:240-244.
4. Park WI, Kim DH, Jung SW, Yi GC: **Metalorganic vapor-phase epitaxial growth of vertically well-aligned ZnO nanorods.** *Appl Phys Lett* 2002, **80(22)**:4232-4234.
5. Greene LE, Law M, Goldberger J, Kim F, Johnson JC, Zhang Y, Saykally RJ, Yang P: **Low-temperature wafer-scale production of ZnO nanowire arrays.** *Angew Chem Int Ed* 2003, **42(26)**:3031-3034.
6. Amarilio-Burshtein I, Tamir S, Lifshitz Y: **Growth modes of ZnO nanostructures from laser ablation.** *Appl Phys Lett* 2010, **96(10)**:103104.

7. Dick KA: **A review of nanowire growth promoted by alloys and non-alloying elements with emphasis on Au-assisted III-V nanowires.** *Prog Cryst Growth Charact Mater* 2008, **54(3-4)**:138-173.
8. Yang J, Song J, Baek S, Lim S: **Effect of surface preparation on the morphology of ZnO nanorods.** *Phys B* 2008, **403(18)**:3034-3039.
9. Thune E, Boulle A, Babonneau D, Pailloux F, Hamd W, Guinebretière R: **Nanostructured sapphire vicinal surfaces as templates for the growth of self-organized oxide nanostructures.** *Appl Surf Sci* 2009, **256(3)**:924-928.
10. Ho ST, Chen KC, Chen HA, Lin HY, Cheng CY, Lin HN: **Catalyst-free surface-roughness-assisted growth of large-scale vertically aligned zinc oxide nanowires by thermal evaporation.** *Chem Mater* 2007, **19(16)**:4083-4086.
11. Guo R, Nishimura J, Higashihata M, Nakamura D, Okada T: **Substrate effects on ZnO nanostructure growth via nanoparticle-assisted pulsed-laser deposition.** *Appl Surf Sci* 2008, **254(10)**:3100-3104.
12. Ghosh SC, Kruse P, Lapierre RR: **The effect of GaAs(100) surface preparation on the growth of nanowires.** *Nanotechnology* 2009, **20(11)**:115602.
13. Kim HW, Shim SH: **Growth of MgO nanowires assisted by the annealing treatment of Au-coated substrates.** *Chem Phys Lett* 2006, **422(1-3)**:165-169.
14. Prete P, Lovergine N, Tapfer L: **Nanostructure size evolution during Au-catalysed growth by carbo-thermal evaporation of well-aligned ZnO nanowires on (100)Si.** *Appl Phys A Mater Sci Process* 2007, **88**:21-26.
15. Zhang G, Nakamura A, Nakagawa S, Aold T, Temmyo J: **Growth and characterization of ZnO nanostructures by remote plasma-enhanced metal-organic chemical vapor deposition.** *phys stat sol (c)* 2006, **3**:722-725.
16. Alet PJ, Eude L, Palacin S, Cabarrocas PRi: **Transition from thin gold layers to nano-islands on TCO for catalyzing the growth of one-dimensional nanostructures.** *phys stat sol (a)* 2008, **205(6)**:1429-1434.
17. Yoshimoto M, Maeda T, Ohnishi T, Koinuma H, Ishiyama O, Shinohara M, Kubo M, Miura R, Miyamoto A: **Atomic-scale formation of ultra-smooth surfaces on sapphire substrates for high-quality thin-film fabrication.** *Appl Phys Lett* 1995, **67(18)**:2615-2617.
18. Stäuble-Pümpin B, Ilge B, Matijasevic VC, Scholte PMLO, Steinfort AJ, Tuinstra F: **Atomic force microscopy study of (001) $SrTiO_3$ surfaces.** *Surf Sci* 1996, **369(1-3)**:313-320.
19. Abràmoff MD, Magalhäes PJ, Ram SJ: **Image processing with ImageJ.** *Biophotonics Int* 2004, **11(7)**:36-41.
20. Wagner RS, Ellis WC: **Vapor-liquid-solid mechanism of single crystal growth.** *Appl Phys Lett* 1964, **4(5)**:89-90.
21. Roozbehi M, Sangpour P, Khademi A, Moshfegh A: **The effect of substrate surface roughness on ZnO nanostructures growth.** *Appl Surf Sci* 2011, **257(8)**:3291-3297.
22. Smith DL: *Thin-Film Deposition: Principles and Practice.* 1 edition. New York: McGraw-Hill Professional; 1995.
23. Jensen P, Larralde H, Meunier M, Pimpinelli A: **Growth of three-dimensional structures by atomic deposition on surfaces containing defects: simulations and theory.** *Surf Sci* 1998, **412, 413**:458-476.
24. Min BK, Wallace WT, Santra AK, Goodman DW: **Role of defects in the nucleation and growth of Au nanoclusters on SiO_2 thin films.** *J Phys Chem B* 2004, **108(42)**:16339-16343.
25. Klamchuen A, Yanagida T, Kanai M, Nagashima K, Oka K, Kawai T, Suzuki M, Hidaka Y, Kai S: **Role of surrounding oxygen on oxide nanowire growth.** *Appl Phys Lett* 2010, **97(7)**:073114.

Paper II

Formation of ZnO nanosheets grown by catalyst-assisted pulsed laser deposition

Abstract. We report on the growth of single-crystal ZnO nanosheets without stacking faults by Au-seeded pulsed laser deposition in a 0.5 mbar pure oxygen ambient, with their growth direction inclined to the ZnO[0001] crystalline axis. Changing the deposition ambient to 5% oxygen and 95% argon at the same total pressure led to formation of [0001]-oriented single-crystalline nanowires. We propose a formation mechanism for ZnO nanosheets based on superposition of catalyst-assisted growth beneath the Au droplet and asymmetric radial growth due to enhanced growth rates on exposed ZnO0001 sidewall facets. The crystalline facets present at the Au-ZnO interface were found to be affected by the VI/II-ratio and seem to play an important role in determining the growth mode of the ZnO nanostructures. A possible mechanism for the formation of a rough Au-ZnO interface with facets different from ZnO(0001) is proposed, on the basis of convergence of the nucleation and step propagation rates at the growth front upon increasing the oxygen partial pressure.

Formation of ZnO Nanosheets Grown by Catalyst-Assisted Pulsed Laser Deposition

C. C. Weigand,[†] M. R. Bergren,[‡] C. Ladam,[§] J. Tveit,[∥] R. Holmestad,[∥] P. E. Vullum,[§] J. C. Walmsley,[§] Ø. Dahl,[§] T. E. Furtak,[‡] R. T. Collins,[‡] J. Grepstad,[†] and H. Weman*,[†]

[†]Department of Electronics and Telecommunications, Norwegian University of Science and Technology, NO-7491 Trondheim, Norway

[‡]Department of Physics, Colorado School of Mines, Golden, Colorado 80401, United States

[§]SINTEF Materials and Chemistry, NO-7465 Trondheim, Norway

[∥]Department of Physics, Norwegian University of Science and Technology, NO-7491 Trondheim, Norway

ABSTRACT: We report on the growth of single-crystal ZnO nanosheets without stacking faults by Au-seeded pulsed laser deposition in a 0.5 mbar pure oxygen ambient, with their growth direction inclined to the ZnO[0001] crystalline axis. Changing the deposition ambient to 5% oxygen and 95% argon at the same total pressure led to formation of [0001]-oriented single-crystalline nanowires. We propose a formation mechanism for ZnO nanosheets based on superposition of catalyst-assisted growth beneath the Au droplet and asymmetric radial growth due to enhanced growth rates on exposed ZnO{0001} sidewall facets. The crystalline facets present at the Au−ZnO interface were found to be affected by the VI/II-ratio and seem to play an important role in determining the growth mode of the ZnO nanostructures. A possible mechanism for the formation of a rough Au−ZnO interface with facets different from those of ZnO(0001) is proposed, on the basis of convergence of the nucleation and step propagation rates at the growth front upon increasing the oxygen partial pressure.
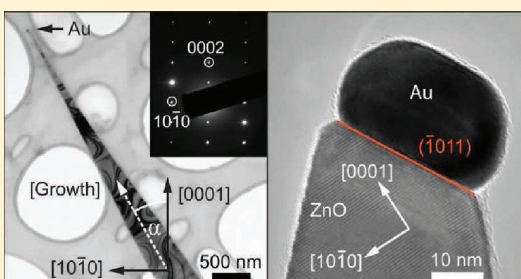
■ INTRODUCTION

A lot of research during the past decade has been devoted to the growth and characterization of ZnO nanostructures.[1,2] Due to their wide band gap (3.37 eV) and high exciton binding energy (60 meV), they are of interest for numerous applications, e.g., field emitters, light-emitting diodes, piezoactuators, and biosensors.[2−4] Each application places special requirements on the material with respect to electronic and optical, as well as mechanical and structural, properties. Since these characteristics often depend on the nanostructure morphology, the type of structure most suitable for a particular application will differ. Many different ZnO nanostructures have been reported in the literature, e.g., nanowires, nanorods, nanobelts, nanorings, nano-tetrapods, and triangular nanosheets.[4−6] Among these, ZnO nanowires and nanorods are the types most frequently considered for device applications. Controlled growth of such ZnO nanostructures has been demonstrated using a variety of growth techniques, including solution-based and vapor deposition techniques, with or without a catalyst.[2,7−10] In contrast, little information exists on the fabrication and properties of triangular ZnO nanosheets. Even though these structures were observed in conjunction with catalyst-assisted growth of ZnO nanowires,[11−13] not much has been published on their characterization and little is known about their formation.[6,14,15]

In a preliminary study,[16] we explored catalyst-assisted growth of ZnO nanostructures by pulsed laser deposition (PLD) for a range of absolute pressures (0.005−0.5 mbar) and two different gas compositions, i.e., pure oxygen and 5% O₂−95% Ar, respectively. Independent of the gas composition, higher ambient pressures were found to promote the growth of ZnO nanostructures. In the present work, we focus on the fabrication of triangular ZnO nanosheets at high ambient pressures by catalyst-assisted PLD and investigate their structural properties using scanning (SEM) and transmission electron microscopy (TEM). Furthermore, we propose a growth mechanism for the formation of nanosheets by PLD growth at elevated oxygen partial pressures.

■ EXPERIMENTAL SECTION

ZnO nanostructures were grown on sapphire substrates by laser ablation from a 99.999% pure ZnO target (American Elements, Inc.) in an on-axis configuration, using a 248 nm pulsed KrF excimer laser (Lambda Physik LPX Pro 210i) with a fluency of ∼1 J/cm² and a pulse repetition rate of 10 Hz. Au-coated c-plane sapphire substrates were placed on a heater at 45 mm distance from the target, which was raster-scanned in a
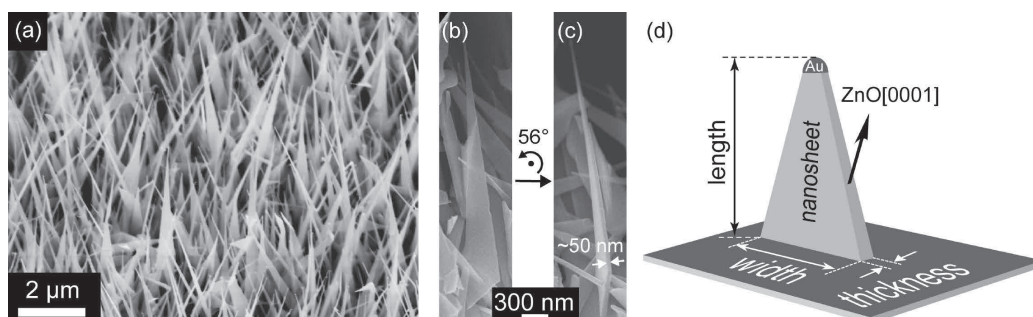
Figure 1. (a) 45° tilted view SEM image of a sample grown at 800 °C in a 0.5 mbar pure oxygen ambient (parameter set 1). (b and c) SEM images of the same nanosheet dispersed on a TEM mesh, recorded at two different tilt angles. (d) Schematic of a ZnO nanosheet with definition of its length, width, and thickness dimensions, also depicting the orientation of the ZnO hexagonal c-axis in the plane of the nanosheet.

circular area of 15 mm in diameter with the laser beam fixed. During deposition, the substrates were kept at 800 °C, as measured with a thermocouple in contact with the heater block. The chamber base pressure was $\sim 1 \times 10^{-7}$ mbar. Following extensive preablation, ZnO deposition was carried out at an absolute pressure of 0.5 mbar of pure oxygen and 5% O_2−95% Ar ambients.

The substrates were cleaned in ultrasonic baths of acetone and ethanol for 5 min each and blown dry with pure nitrogen prior to introduction in an electron beam evaporator, where a 2.5 nm thick Au layer was deposited onto the substrate surface. The substrates were then mounted on the PLD substrate holder using thermally conductive silver paste. After introduction into the PLD chamber, the substrates were heated to the desired growth temperature at a rate of 15 °C/min, followed by ZnO deposition for 15 min up to 1 h. After ablation, the samples were left to cool at a rate of 15 °C/min while maintaining the ambient conditions in the chamber.

As-grown samples were characterized using a Zeiss Supra VP55 SEM, and individual nanostructures which were separated from the substrate and dispersed on a carbon mesh were studied with a Hitachi S-5500 SEM and a JEOL 2010F TEM, operating at 200 kV.

■ RESULTS AND DISCUSSION

An SEM image of ZnO grown by PLD at a substrate temperature of T_{sub} = 800 °C in a pure oxygen atmosphere (parameter set 1) is displayed in Figure 1a and shows a dense array of ZnO nanosheets with average lengths of 4.5 ± 1 μm. As can be seen from SEM micrographs recorded at two different tilt angles of the same nanosheet dispersed on a TEM mesh (Figure 1b and c), the nanosheets exhibit a flat and triangular morphology. The average thickness of a nanosheet (cf. Figure 1d) is 51 ± 10 nm near the base and 30 ± 9 nm at the tip, while the average width is 508 ± 130 nm near the base and 34 ± 6 nm at the tip.

TEM images of single nanosheets, cf. Figure 2a and b, reveal a gold particle at the tip of each sheet, indicating a catalyst-assisted growth mechanism. Figure 2a also shows that the nanosheets are single-crystalline and free from stacking faults, but significantly bent, as is evident in the numerous bending contours. Their growth axis, as indicated by the white dashed arrow in Figure 2a, is not confined to a single direction, but always inclined to the ZnO[0001] axis by an angle α, as depicted in Figure 2a. This angle was found to vary from sheet to sheet between values of 11° and 48°. Minor shifts in the growth direction along the length of a nanosheet were frequently observed. Most nanosheets were
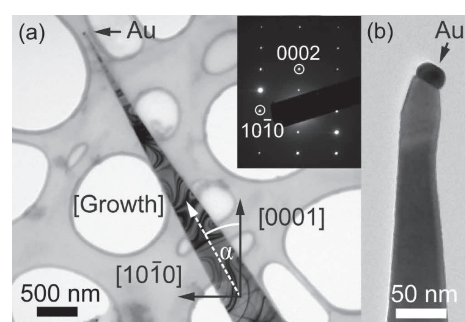
Figure 2. (a) Bright-field TEM image with corresponding selected-area electron diffraction (SAED) pattern of a single ZnO nanosheet, showing the inclination angle α of the growth direction with the ZnO hexagonal c-axis. (b) Bright-field image of a nanosheet tip showing a kink below the Au catalyst droplet.

found to exhibit a kink at the very tip, as shown in Figure 2b. The ZnO[0001] axis was found to lie in the plane of the nanosheet for all samples examined, as depicted schematically in Figure 1d. Besides the predominant nanosheet morphology, a small number of ZnO nanowires were observed for these growth conditions.

In comparison, formation of ZnO nanowires was found to predominate (Figure 3a) upon reduction of the oxygen partial pressure in the growth chamber ambient, cf. parameter set 2 in Table 1. The average diameter of the nanowires varied from 55 ± 15 nm near the base to 28 ± 7 nm at the tip, for a total average length of 2.1 ± 0.7 μm. Small Au particles were observed at the tip of the nanowires, suggesting catalyst-assisted growth. The TEM image and SAED pattern in Figure 3b show that the nanowires are single-crystalline, are free from stacking faults, and grow along the ZnO hexagonal c-axis.

The growth of nanostructures using a catalyst and a vapor phase source is often described in terms of the vapor−liquid−solid (VLS) mechanism. It involves the dissolution of growth species in a liquid catalyst droplet at the tip of the nanostructure, followed by precipitation and growth at the catalyst−nanowire interface.[17] However, nanowire growth is also possible from solid catalyst particles, and it has been argued that not only bulk
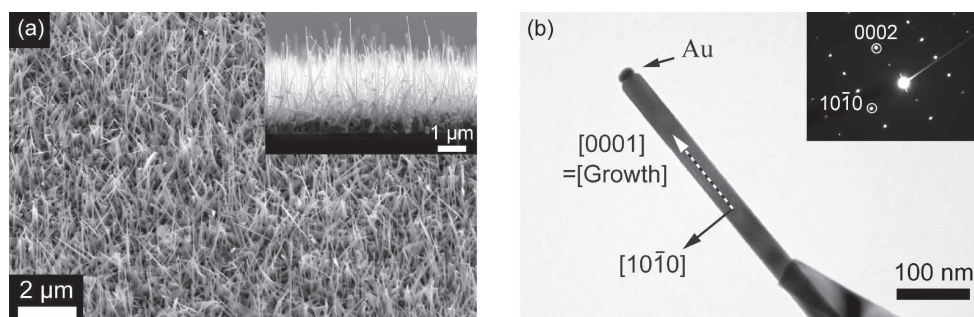
Figure 3. (a) 45° tilted view and cross-sectional (inset) SEM images of a sample grown at 800 °C in a 0.5 mbar mixed ambient of 5% oxygen and 95% argon (parameter set 2). (b) Bright-field TEM image with its corresponding SAED pattern of a single nanowire.

Table 1. Growth Conditions for the Discussed PLD-Grown Samples

	parameter set 1	parameter set 2
temperature	800 °C	800 °C
gas composition	100% O_2	5% O_2—95% Ar
deposition time	60 min	60 min
total pressure	0.5 mbar	0.5 mbar
structures observed	nanosheets	nanowires

diffusion through the particle but also surface diffusion might play an important role in such catalyst-assisted growth.[18−20] We thus adopt the more general term "preferential interface nucleation" to describe nanowire growth from a catalyst droplet, as suggested by Wacaser et al.[21] In this case, nanowire formation occurs by preferential nucleation at the catalyst−nanowire interface and subsequent rapid growth underneath the catalyst particle, allowing for both solid and liquid catalysts as well as surface and bulk diffusion.

The formation of a ZnO nanowire is mainly governed by preferential interface nucleation, as shown schematically in Figure 4a−c. Upon heating of the substrate, the thin Au layer self-organizes into small droplets.[22,23] Then, nucleation takes place at the catalyst−nanowire interface, and nanowire growth proceeds by step propagation beneath the catalyst droplet.[24,25] Even though growth underneath the catalyst dominates, the specific growth conditions can still allow for significant catalyst-free radial growth on the nanowire sidewalls via the vapor−solid (VS) mechanism, with growth rates determined by the surface energy and stability of the sidewalls.[26,27] ZnO nanowire growth is often reported to proceed in the ZnO[0001] direction,[4,10,28−31] which is also observed for the nanowires grown in this work (parameter set 2). All side facets are therefore composed of identical ZnO crystal planes with equal surface energies and VS growth rates. Radial growth will thus be "isotropic" ($VS_B = VS_A$ in Figure 4b), and the ratio of axial to radial growth rates will determine the tapering of the nanowire. For simplicity, we assume here a hexagonal cross section for the nanowires. This assumption is, however, not essential for the discussed growth mechanism, and near "isotropic" radial growth can be expected also for circular cross sections due to the small differences in surface energy of other low-index ZnO crystal planes perpendicular to the ZnO(0001) plane.[32]

It has been previously proposed that tapered ZnO nanostructures could evolve from instability, i.e. the decrease in size, of the
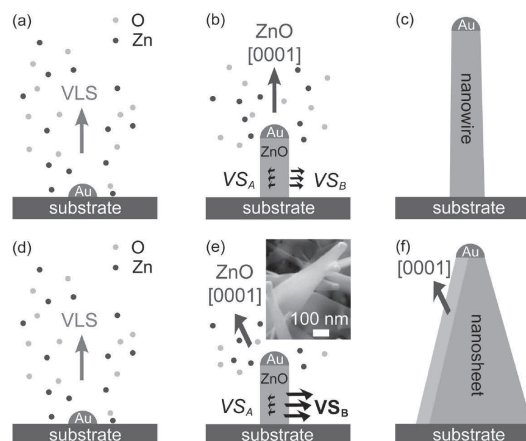
Figure 4. Schematic illustration of the growth mechanism for a nanowire (a−c) and a nanosheet (d−f). ZnO nanowire growth is nucleated by a Au catalyst particle (a) and proceeds at a fast growth rate in the ZnO[0001] direction underneath the Au droplet, denoted by VLS (b). Here, all side facets have equal VS growth rates ($VS_B = VS_A$). (c) Final nanowire morphology. (d) ZnO nanosheet growth is also nucleated from a Au particle, and catalytic growth predominates. (e) For the nanosheets, the growth direction is inclined to the ZnO[0001] axis. Sidewalls A have a lower VS growth rate than sidewalls B ($VS_B \gg VS_A$) due to exposed ZnO{0001} facets. Inset: the nanosheet morphology is already present at the early growth stage (15 min deposition). (f) Final flat, triangular nanosheet morphology with the hexagonal ZnO c-axis lying in the plane of the nanosheet.

catalyst droplet at the nanostructure tip during growth.[33] For ZnO nanosheet formation, however, this would imply that the size of the catalyst alloy droplet would have to be comparable to the dimensions of the nanosheet base at the initial stage of the ZnO growth. Catalyst droplets of up to 700 nm in diameter would thus be required at the tip of a growing nanosheet. The thickness of the initial Au catalyst layer, however, is only 2.5 nm and ZnO depositions carried out in our group under various growth conditions and durations showed similar catalyst droplet sizes of 20−40 nm in diameter at the tips of nanowires and nanosheets alike. Furthermore, it has been shown that diffusion of catalyst material away from the tips of oxide nanostructures is negligible in the pressure regime adopted in this work.[34] We

therefore discard the possibility that growth mediated by the catalyst droplet alone is responsible for the evolution of the nanosheet morphology.

Increased tapering in oxide nanostructures has been reported upon reduction in substrate temperature due to reduced diffusion lengths of the growth species.[23] However, since the substrate temperature is kept constant during nanowire and nanosheet growth alike, the corresponding diffusion lengths in the present study should not be significantly different.

Instead, we picture the nanosheet growth starting with the formation of a nanowire nucleus due to preferential nucleation at the catalyst interface (Figure 4d−f), similar to the mechanism leading to the nanowire morphology, where growth underneath the catalyst predominates and the axial growth rate is the highest. However, the nanostructure grows in a direction inclined to the ZnO hexagonal c-axis. This implies that two opposite nanostructure sidewalls include a small fraction of $ZnO\{0001\}$ facets. These facets have the largest surface energy and, consequently, the highest VS growth rate of all the ZnO low-index planes.[26,27,32] With different planes growing at different speeds, faceting of these two sidewalls might be expected. However, due to high substrate temperature and supersaturation, the surfaces are flattened by interspace filling of concave corner sites, leading to smooth surfaces of these sidewalls, as observed in Figure 2a.[6] Practically, the presence of the $ZnO\{0001\}$ facets therefore enhances the overall growth rate of these two sidewalls without introducing faceting ($VS_B \gg VS_A$ in Figure 4e). The radial growth is thus anisotropic. Furthermore, the sidewalls established early in the growth process, i.e. near the substrate, are available to VS growth for a longer period of time than those created shortly before growth termination, i.e. at the nanosheet tip. This leads to the final flat and triangular nanosheet morphology, with a large width at the base and a small width near the tip. We note that depicting the initial nanosheet growth stage by the nanowire morphology in Figure 4e is for purposes of clarity only. In reality, the nanostructure resembles the final nanosheet morphology also at the early stage, since axial catalyst-assisted and radial VS sidewall growth occur simultaneously (cf. inset in Figure 4e).

The proposed growth mechanism implies that the nanosheet morphology can only be observed under growth conditions allowing for sufficient VS growth. It has been previously reported for oxide nanowire growth by PLD that an increasing oxygen partial pressure enhances the degree of VS sidewall growth.[35,36]

As mentioned above, the formation of a nanosheet can be envisaged as the formation of an initial nanowire with a growth direction that deviates from the ZnO c-axis. Only the preferential VS growth on two opposite sidewalls with a small fraction of $ZnO(0001)$ and $ZnO(000\bar{1})$ facets, respectively, leads to the evolution of the final nanosheet morphology. It is difficult, however, to determine the exact growth direction of the initial nanowire from the recorded TEM images due to the expansion of the sidewalls. In principle, two scenarios are possible: in the first, the VS growth rates of the (0001) and $(000\bar{1})$ facets are identical, and the initial nanowire grows along the center of the nanosheet, as illustrated by the dashed arrow in Figure 2a. The second (more likely) scenario derives from different growth rates of the ZnO-(0001) and $(000\bar{1})$ facets. In the extreme case, VS growth on one of the two facets could be fully suppressed, suggesting that the initial nanowire grows along one of the two nanosheet edges. In fact, a significant difference in the VS growth rates for the two polar ZnO surfaces was reported.[37] Although VS growth on the

oxygen terminated $(000\bar{1})$ facet was not fully suppressed, preferential deposition on the Zn-terminated (0001) surface was observed. The ratio of VS growth rates for ZnO nanosheet sidewalls with (0001) and $(000\bar{1})$ facets, respectively, will be sensitive to the growth conditions in the PLD chamber and is difficult to determine. Therefore, the precise growth direction of the initial nanowire of the ZnO nanosheets could not be unambiguously defined. Moreover, the minor bends and kinks found in some of the nanosheets indicate that their growth direction can shift during deposition.

In the growth mechanism proposed above, the inclination of the growth direction with respect to the $ZnO[0001]$ axis is crucial for the formation of nanosheets. Whereas catalyst-induced growth of ZnO nanostructures is commonly reported to proceed in the $[0001]$ direction,[2,4,31] deviations from the most stable growth axes have been observed in numerous materials systems and various possible reasons have been advanced to explain these alternative growth directions. In the following section we will discuss the applicability of these mechanisms to the evolution of the ZnO nanosheets observed in our experiments.

Several authors attribute such deviations in nanowire growth direction to the size of the catalyst droplet.[38,39] Below a critical droplet size, minimization of Gibbs free energy favors a different crystal facet at the catalyst−nanowire interface and thus a different growth direction. We have measured the size of the catalyst droplet at the tips of nanosheets and nanowires in our samples, using TEM, without finding any correlation between Au droplet size and the growth morphology. The droplet diameters were found to be nearly identical for nanosheets and nanowires, with measured average values of 30 ± 7 nm and 31 ± 8 nm, respectively.

It has been shown that the catalyst metal species has a significant impact on the growth morphology and orientation of the nanostructures.[40,41] The chemical composition of the catalyst droplets in this experiment was analyzed by energy dispersive X-ray spectroscopy (EDS) in TEM. Besides gold, the spectra from the droplets of both nanowires and nanosheets showed minor traces of silver, which may originate from sublimated silver paste used to mount the substrates in the PLD chamber. However, no difference in the Ag signal was observed for spectra taken from the catalyst droplets of several nanosheets and a few nanowires found on a sample grown by parameter set 1. This indicates that both nanosheets and nanowires can grow from catalyst droplets with the same chemical composition (within the accuracy of EDS).

Catalyst-assisted growth proceeds perpendicular to the catalyst-nanowire interface, and the growth direction of a nanowire is thus determined by the crystal facets present at this interface.[21] Under equilibrium conditions, minimization of the total interface and surface energies will govern the formation of those facets. In most cases, the catalyst−nanowire interface is a single facet, i.e. the most stable growth surface of the nanowire crystal, e.g. $(111)B$ for GaAs and (0001) for ZnO, leading to nanowire growth in the well-known directions ($[111]B$ for GaAs and $[0001]$ for ZnO, respectively).[42] However, certain growth conditions can allow for nonflat catalyst−nanowire interfaces with different single or multiple facets and the growth direction can therefore deviate from the commonly observed orientations.[39,43] In Figure 5a, the Au−ZnO interface of a nanowire growing in the $ZnO[0001]$ direction (parameter set 2) is examined in detail by TEM. The interface is a single $ZnO(0001)$ facet covered entirely
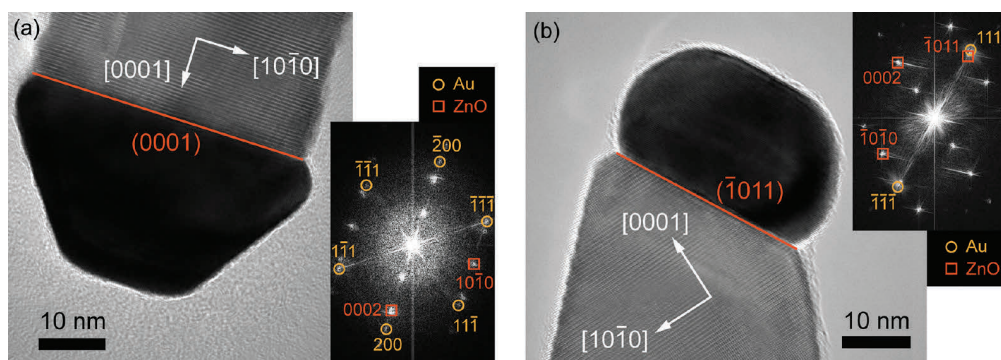
Figure 5. (a) High-resolution TEM image and its Fourier transform of a nanowire, grown in a 0.5 mbar mixed ambient of 5% O_2—95% Ar (parameter set 2). (b) High-resolution TEM image and its Fourier transform of a nanosheet grown in a 0.5 mbar pure oxygen ambient (parameter set 1).

by the Au droplet. This observation is consistent with formation of the most stable growth facet at the catalyst—nanowire interface, as discussed above.

In contrast, the Au—ZnO interface of nanosheets grown at high oxygen partial pressure (parameter set 1) is found to be a single ZnO($\bar{1}011$) facet for all samples examined (Figure 5b). This suggests that the Au—ZnO interface can take on facets other than ZnO(0001) under certain growth conditions and growth directions other than ZnO[0001] are possible. We note, however, that the Au—ZnO interface at the tips of the nanosheets may differ from the facets present during the actual growth. As described above, a small kink was observed for all the examined nanosheets only a few tens of nanometers below the tip. We attribute this kink to postgrowth formation caused by the persistent flow of oxygen during sample cooling. ZnO nucleation can then occur at the catalyst—nanowire interface even after the laser has been switched off, fed by purging of the Zn reservoir in the gold droplet (no Zn was measured in the EDS spectra from the Au droplets) or possibly by residual Zn vapor in the PLD chamber.[44] Under these conditions, the supersaturation, i.e. the chemical potential difference of growth species in the supply phase (catalyst droplet or vapor source) and the solid phase (ZnO nanostructure), is reduced and the VI/II-ratio is increased. Since the formation of a kink essentially implies a shift in growth direction, this finding provides further evidence that the VI/II-ratio can be used to control the growth direction of ZnO nanostructures.

The question remains, however, why facets other than ZnO-(0001) form at the catalyst—nanowire interface, even though they are less favorable energetically, and what role the oxygen partial pressure plays in the formation of these facets. Increasing the oxygen partial pressure may affect the growth mechanisms of catalyst-assisted PLD in several ways. First, the increase in VI/II-ratio imposed by an increased oxygen partial pressure may affect the surface energy of the catalyst droplet and the nanowire side facets and, thus, influence the energy balance of the growth interface.[45] Second, an increased oxygen partial pressure will also affect the supersaturation, i.e. the driving force for nucleation and growth of ZnO. While the original VLS model and numerous studies of catalyst-assisted nanowire growth take into account the supersaturation inside the catalyst particle only,[17,46,47] nucleation in catalyst-assisted nanowire growth can also be affected by supersaturation in the vapor, and corresponding Gibbs free
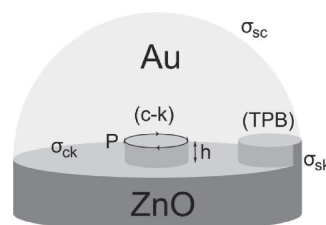
Figure 6. Schematic illustration of different nucleation sites in catalyst-assisted nanowire growth. Nucleation at the catalyst—nanowire interface nucleus labeled (c—k); nucleation at the three-phase boundary is abbreviated (TPB). The dimensions h and P denote the height and perimeter length of the nuclei.

energies can be formulated for different nucleation sites.[21] In the following, the two most important cases relevant to the present study will be discussed. The first case considers nucleation beneath the catalyst—nanowire interface, as depicted by the nucleus (c—k) in Figure 6. The corresponding energy barrier for nucleation is given by

$$\Delta G_{ck} = -n\Delta\mu_{ck} + Ph\sigma_{ck} \qquad (1)$$

where $\Delta\mu_{ck}$ is the supersaturation in the catalyst droplet and n is the number of atoms or buildings blocks of the nucleus with height h and perimeter length P. σ_{ck} denotes the surface energy of the catalyst (c)—crystal (k) interface. As can be seen from eq 1, nucleation at the interface is governed entirely by the supersaturation inside the catalyst. In the second case, nucleation occurs at the three-phase boundary (TPB), denoted by nucleus (TPB) in Figure 6. The corresponding Gibbs free energy can be written as

$$\Delta G_{TPB} = -n\Delta\mu_{sk} + P_{ck}h\sigma_{ck} + P_{sk}h\sigma_{sk} \qquad (2)$$

where $\Delta\mu_{sk}$ is the supersaturation in the vapor and P_{sk}, σ_{sk} and P_{ck}, σ_{ck} denote the perimeter lengths and surface energies of nucleus segments in contact with vapor (supply s) and catalyst (c), respectively. In this case, the nucleation is governed by the vapor supersaturation.

The nucleation event is the very first stage of catalyst-assisted nanowire growth and can occur at either of the two nucleation

sites discussed above. In both cases, the nanowire growth subsequently proceeds by step propagation beneath the catalyst—nanowire interface to complete a full monolayer before another nucleus is formed.[48]

In PLD, the Zn concentration in the vapor is governed mainly by the laser energy density on the target and the substrate temperature (desorption) and is therefore thought to be unaffected by the oxygen partial pressure. However, the oxygen concentration in the vapor increases with oxygen partial pressure and leads to an increased vapor supersaturation. Moreover, ZnO may already form in the vapor by a gas phase reaction of zinc and oxygen

$$2Zn_{(v)} + O_{2(v)} \rightleftharpoons 2ZnO_{(s)} \qquad (3)$$

where (v) and (s) denote the vapor and solid phases, respectively. Similarly, ZnO can also be formed at the vapor—catalyst interface via oxidation of Zn dissolved in the liquid catalyst droplet,

$$2Zn_{(l)} + O_{2(v)} \rightleftharpoons 2ZnO_{(s)} \qquad (4)$$

where (l) denotes the liquid phase. According to Le Chatelier's principle, an increase in oxygen concentration in the vapor shifts the chemical equilibrium toward the right-hand side of reactions 3 and 4, leading to increased consumption of both liquid- and vapor-phase Zn reactants to form ZnO.[49] Inside the catalyst droplet, the Zn concentration is therefore diminished, whereas the oxygen concentration most likely remains unchanged due to the low solubility of oxygen in gold.[50] Thus, the supersaturation $\Delta\mu_{ck}$ inside the catalyst droplet decreases with increasing oxygen partial pressure.

On the basis of this analysis, we propose a mechanism for the formation of ZnO nanosheets or, more generally, nanowires with a growth direction that differs from the most stable one under the influence of increased VI/II-ratios. We consider the growth of a nanowire first under the growth conditions used in parameter set 2 and subsequently under increased oxygen partial pressure. Two scenarios are possible for nanowire formation with parameter set 2: nucleation occurs (a) at the catalyst—nanowire interface and (b) at the TPB.

For nucleation at the catalyst—nanowire interface, the nucleation and growth rates are governed by the supersaturation $\Delta\mu_{ck}$ inside the catalyst. When the oxygen partial pressure is raised (moving toward the conditions of parameter set 1), the reduction in $\Delta\mu_{ck}$ results in a higher energy barrier for nucleation at the catalyst—nanowire interface in eq 1. Simultaneously, the vapor supersaturation increases and the corresponding Gibbs free energy for nucleation at the TPB is lowered. This results in a lower barrier for nucleation at the TPB while the supersaturation in the catalyst may fall below the threshold for activation of nucleation at the catalyst—nanowire interface. Thus, the nucleation site shifts from the center of the catalyst—nanowire interface to the TPB upon oxygen partial pressure increase.

Furthermore, the vapor supersaturation $\Delta\mu_{sk}$ governs the rate of nucleation at the TPB, R_{TPB}, whereas the step propagation rate, R_{step}, is controlled by the supersaturation $\Delta\mu_{ck}$ in the catalyst. For the growth of nanowires by parameter set 2, R_{step} largely exceeds R_{TPB}, and a full monolayer is completed before a second nucleus is formed.[48] When the oxygen partial pressure is raised, the step propagation rate, R_{step}, is reduced (since $\Delta\mu_{ck}$ decreases), while R_{TPB} will be enhanced due to the increase in vapor supersaturation $\Delta\mu_{sk}$. If the change in rates is sufficiently

large, i.e. they become comparable, additional nucleation will occur at the TPB before a full monolayer is completed, essentially adding a new facet at the catalyst—nanostructure interface. As a result, the interface roughness and thus also the interface area are increased, resulting in a higher energy of the catalyst—nanostructure interface. Consequently, the combined surface and interface energy of the catalyst—nanostructure system is increased, which may cause less stable nanostructure growth, i.e. single or multiple growth facets other than ZnO(0001). The growth direction of the nanostructure changes accordingly and deviates from that of ZnO[0001], leading to the observed morphology of the nanosheets, promoted by preferential growth on the {0001}-containing sidewalls.

■ CONCLUSION

In conclusion, we have demonstrated catalyst-assisted growth of ZnO nanosheets with a flat and triangular morphology using pulsed laser deposition. For high oxygen partial pressures, formation of single-crystalline nanosheets with a growth direction inclined to the hexagonal c-axis was dominant, whereas a low oxygen partial pressure led to the formation of nanowires growing in the ZnO[0001] direction. A growth mechanism for the formation of nanosheets is proposed, in which the growth direction of the initial nanowire explains the final nanostructure morphology. TEM data strongly indicate that the crystalline facets present at the Au—ZnO interface play an important role in determining the nanowire growth direction and, thus, the final morphology of the nanostructure. An explanation for the formation of facets other than the most stable ZnO(0001) may be found in convergence of the nucleation rate at the three-phase boundary and the step propagation rate caused by changes in the supersaturation in the vapor and in the catalyst droplet due to an increased VI/II-ratio.

■ AUTHOR INFORMATION

Corresponding Author
*E-mail: helge.weman@iet.ntnu.no.

■ ACKNOWLEDGMENT

■ REFERENCES

(1) Wang, Z. L. *Mater. Sci. Eng., R* **2009**, *64*, 33–71.
(2) Yi, G.-C.; Wang, C.; Park, W. I. *Semicond. Sci. Technol.* **2005**, *20*, S22–S23.
(3) Wang, J. X.; Sun, X. W.; Wei, A.; Lei, Y.; Cai, X. P.; Li, C. M.; Dong, Z. L. *Appl. Phys. Lett.* **2006**, *88*, 233106.
(4) Wang, Z. L. *J. Phys.: Condens. Matter* **2004**, *16*, R829–R858.
(5) Liu, D.; Wu, W.; Qiu, Y.; Yang, S.; Xiao, S.; Wang, Q.-Q.; Ding, L.; Wang, J. *Langmuir* **2008**, *24*, 5052–5059.
(6) Park, J.-H.; Choi, H.-J.; Choi, Y.-J.; Sohn, S.-H.; Park, J.-G. *J. Mater. Chem.* **2004**, *14*, 35–36.
(7) Vayssieres, L. *Adv. Mater.* **2003**, *15*, 464–466.
(8) Kong, Y. C.; Yu, D. P.; Zhang, B.; Fang, W.; Feng, S. Q. *Appl. Phys. Lett.* **2001**, *78*, 407–409.

(9) Kawakami, M.; Hartanto, A. B.; Nakata, Y.; Okada, T. *Jpn. J. Appl. Phys.* **2003**, *42*, L33–L35.

(10) Huang, M. H.; Wu, Y.; Feick, H.; Tran, N.; Weber, E.; Yang, P. *Adv. Mater.* **2001**, *13*, 113–116.

(11) Park, J.; Choi, H.; Park, J. *J. Korean Phys. Soc.* **2004**, *45*, 729–732.

(12) Dalal, S. H.; Baptista, D. L.; Teo, K. B. K.; Lacerda, R. G.; Jefferson, D. A.; Milne, W. I. *Nanotechnology* **2006**, *17*, 4811–4818.

(13) Heo, Y. W.; Varadarajan, V.; Kaufman, M.; Kim, K.; Norton, D. P.; Ren, F.; Fleming, P. H. *Appl. Phys. Lett.* **2002**, *81*, 3046–3048.

(14) Amarilio-Burshtein, I.; Tamir, S.; Lifshitz, Y. *Appl. Phys. Lett.* **2010**, *96*, 103104.

(15) Rahm, A.; Yang, G.; Lorenz, M.; Nobis, T.; Lenzner, J.; Wagner, G.; Grundmann, M. *Thin Solid Films* **2005**, *486*, 191–194.

(16) Weigand, C.; Bergren, M.; Valset, K.; Carey, D.; Fagerberg, R.; Ladam, C.; Grepstad, J.; Weman, H.; Furtak, T. E.; Collins, R. T. *Proc. 23rd Eur. Photovoltaic Conf. Exhib.* **2008**, 692.

(17) Wagner, R. S.; Ellis, W. C. *Appl. Phys. Lett.* **1964**, *4*, 89–90.

(18) Persson, A. I.; Larsson, M. W.; Stenstrom, S.; Ohlsson, B. J.; Samuelson, L.; Wallenberg, L. R. *Nat. Mater.* **2004**, *3*, 677–681.

(19) Cheyssac, P.; Sacilotti, M.; Patriarche, G. *J. Appl. Phys.* **2006**, *100*, 044315.

(20) Wang, H.; Fischman, G. S. *J. Appl. Phys.* **1994**, *76*, 1557–1562.

(21) Wacaser, B. A.; Dick, K. A.; Johansson, J.; Borgström, M. T.; Deppert, K.; Samuelson, L. *Adv. Mater.* **2008**, *21*, 153–165.

(22) Alet, P.-J.; Eude, L.; Palacin, S.; Cabarrocas, P. R. i. *Phys. Status Solidi A* **2008**, *205*, 1429–1434.

(23) Nagashima, K.; Yanagida, T.; Tanaka, H.; Kawai, T. *Appl. Phys. Lett.* **2007**, *90*, 233103.

(24) Hofmann, S.; Sharma, R.; Wirth, C. T.; Cervantes-Sodi, F.; Ducati, C.; Kasama, T.; Dunin-Borkowski, R. E.; Drucker, J.; Bennett, P.; Robertson, J. *Nat. Mater.* **2008**, *7*, 372–375.

(25) Oh, S. H.; Chisholm, M. F.; Kauffmann, Y.; Kaplan, W. D.; Luo, W.; Rühle, M.; Scheu, C. *Science* **2010**, *330*, 489–493.

(26) Smith, D. L. *Thin-Film Deposition: Principles and Practice*, 1st ed.; McGraw-Hill Professional: New York, 1995; p 153.

(27) Laudise, R. A.; Ballman, A. A. *J. Phys. Chem.* **1960**, *64*, 688–691.

(28) Doherty, R.; Sun, Y.; Sun, Y.; Warren, J.; Fox, N.; Cherns, D.; Ashfold, M. *Appl. Phys. A: Mater. Sci. Process.* **2007**, *89*, 49–55.

(29) Zuniga-Perez, J.; Rahm, A.; Czekalla, C.; Lenzner, J.; Lorenz, M.; Grundmann, M. *Nanotechnology* **2007**, *18*, 195303.

(30) Song, M. Y.; Ahn, Y. R.; Jo, S. M.; Kim, D. Y.; Ahn, J.-P. *Appl. Phys. Lett.* **2005**, *87*, 113113.

(31) Liu, Z.; Zhang, D.; Li, C.; Zhou, C. *Proceedings of the 3rd IEEE Conference on Nanotechnology, IEEE-NANO (San Francisco, 2003)*, Piscataway, NJ, 2003; pp 592−595.

(32) Meyer, B.; Marx, D. *Phys. Rev. B* **2003**, *67*, 035403.

(33) Kar, A.; Low, K.-B.; Oye, M.; Stroscio, M.; Dutta, M.; Nicholls, A.; Meyyappan, M. *Nanoscale Res. Lett.* **2011**, *6*, 1–9.

(34) Yanagida, T.; Nagashima, K.; Tanaka, H.; Kawai, T. *Appl. Phys. Lett.* **2007**, *91*, 061502.

(35) Nagashima, K.; Yanagida, T.; Oka, K.; Tanaka, H.; Kawai, T. *Appl. Phys. Lett.* **2008**, *93*, 153103.

(36) Klamchuen, A.; Yanagida, T.; Kanai, M.; Nagashima, K.; Oka, K.; Kawai, T.; Suzuki, M.; Hidaka, Y.; Kai, S. *Appl. Phys. Lett.* **2010**, *97*, 073114.

(37) Wang, Z. L.; Kong, X. Y.; Zuo, J. M. *Phys. Rev. Lett.* **2003**, *91*, 185502.

(38) Cai, Y.; Chan, S.; Sou, I.; Chan, Y.; Su, D.; Wang, N. *Adv. Mater.* **2006**, *18*, 109–114.

(39) Wu, Y.; Cui, Y.; Huynh, L.; Barrelet, C. J.; Bell, D. C.; Lieber, C. M. *Nano Lett.* **2004**, *4*, 433–436.

(40) Andreazza-Vignolle, C.; Andreazza, P.; Zhao, D. *Superlattices Microstruct.* **2006**, *39*, 340–347.

(41) Nguyen, P.; Ng, H.; Meyyappan, M. *Adv. Mater.* **2005**, *17*, 1773–1777.

(42) Seifert, W.; Borgström, M.; Deppert, K.; Dick, K. A.; Johansson, J.; Larsson, M. W.; Mårtensson, T.; Sköld, N.; Svensson, C. P. T.; Wacaser, B. A.; Wallenberg, L. R.; Samuelson, L. *J. Cryst. Growth* **2004**, *272*, 211–220.

(43) Wang, N.; Cai, Y.; Zhang, R. *Mater. Sci. Eng., R* **2008**, *60*, 1–51.

(44) Harmand, J. C.; Patriarche, G.; Pere-Laperne, N.; Merat-Combes, M.-N.; Travers, L.; Glas, F. *Appl. Phys. Lett.* **2005**, *87*, 203101.

(45) Cirlin, G. E.; Dubrovskii, V. G.; Samsonenko, Y. B.; Bouravleuv, A. D.; Durose, K.; Proskuryakov, Y. Y.; Mendes, B.; Bowen, L.; Kaliteevski, M. A.; Abram, R. A.; Zeze, D. *Phys. Rev. B* **2010**, *82*, 035302.

(46) Glas, F.; Harmand, J.-C.; Patriarche, G. *Phys. Rev. Lett.* **2007**, *99*, 146101.

(47) Borchers, C.; Muller, S.; Stichtenoth, D.; Schwen, D.; Ronning, C. *J. Phys. Chem. B* **2006**, *110*, 1656–1660.

(48) Wen, C.-Y.; Reuter, M. C.; Bruley, J.; Tersoff, J.; Kodambaka, S.; Stach, E. A.; Ross, F. M. *Science* **2009**, *326*, 1247–1250.

(49) Atkins, P.; De Paula, J. *Atkins' physical chemistry*; Oxford University Press: Oxford, 2006; p 210.

(50) Predel, B. Au-O (Gold-Oxygen). In *SpringerMaterials—The Landolt-Börnstein Database* (http://www.springermaterials.com/docs/info/10000866_300.html; DOI: 10.1007/10000866_300); Madelung, O., Ed.; Vol. 5a.

Paper III

Epitaxial relationships of ZnO nanostructures grown by Au-assisted pulsed laser deposition on c- and a-plane sapphire

Abstract. We report on the epitaxial growth of ZnO nanosheets and nanowires on a- and c-plane sapphire substrates by Au-assisted pulsed laser deposition. The epitaxial relationship of the nanostructures was determined by x-ray diffraction (XRD) pole figure measurements. On c-plane sapphire, the ZnO nanowires grew along the ZnO c-axis and were inclined to the substrate surface normal with an angle of about $37°$. The ZnO(0001) plane of the wires aligned with $Al_2O_3(10\bar{1}4)$ of the sapphire substrate via two degenerate in-plane configurations, promoted by low lattice mismatch (0.05 %). ZnO nanosheets grown on c-plane sapphire exhibited no preferential orientation on the substrate and no epitaxial relationship could be unambiguously identified. On a-plane sapphire, ZnO nanowires grew vertically along the ZnO c-axis with a single epitaxial configuration, whereas ZnO nanosheets seemed to grow along $ZnO[10\bar{1}0]$ in two preferred in-plane orientations, $72°$ - $74°$ apart. These configurations could be explained by two distinct alignments of the $ZnO(10\bar{1}1)$ plane on the a-plane sapphire substrate surface, promoted by low lattice mismatches.

Paper IV

Electrical, optical and structural properties of Al-doped ZnO thin films grown on GaAs(111)B substrates by pulsed laser deposition

Abstract. We report on the characteristics of Al-doped ZnO thin films (AZO) grown on GaAs(111)B substrates using pulsed laser deposition. The influence of ambient gas composition, overall pressure, and growth temperature on the electrical, structural and optical properties of 100 nm-thin films grown from a ZnO target with 2 wt% Al were investigated. Growth in a 0.01 mbar pure O_2 ambient was found to be superior to films grown in Ar ambient or vacuum with respect to their electrical properties. As-grown AZO films showed a low resistivity on the order of 10^{-4} Ωcm. Post-deposition annealing *in-situ* showed no improvement of the transport properties, irrespective of annealing temperature and ambient gas. At high substrate temperatures, the interaction with the GaAs(111)B substrate seemed to affect the growth and conductivity of the AZO films.

Status: Manuscript in preparation. To be submitted to Thin Solid Films.

Is not included due to copyright

Chapter 5

Conclusion and outlook

In this work, some fundamental aspects of ZnO nanostructure growth by catalyst-assisted pulsed laser deposition have been investigated. It has been shown in Paper I that the presence of surface nucleation sites has a significant influence on the size and number density of ZnO nanostructures on the substrate. Despite the "sink"-like action of the catalyst on impinging growth species, nucleation at the Au droplets competes with surface nucleation sites for available growth atoms, leading to reduced sizes and number densities of ZnO nanostructures. The paper also shows that suitable thermal pretreatments of the substrate can successfully suppress surface nucleation sites by forming a well-defined surface state.

In Paper II, some insight is given into the effects of ambient oxygen on the morphology of ZnO nanostructures. By changing the oxygen partial pressure in the chamber, the ZnO nanostructure morphology can be switched between nanowires and triangular nanosheets. Simultaneously, distinct differences in the facets present at the catalyst-nanowire interface of the two nanostructure types have been observed. This phenomenon is attributed to relative changes of the supersaturation in the catalyst droplet and in the vapour phase induced by a rise in oxygen partial pressure. It is believed that the excess oxygen thereby leads to altered growth kinetics resulting in alternative facets at the growth front.

Furthermore, the epitaxial relationships of both nanowires and triangular nanosheets grown on c- and a-plane sapphire substrates have been studied in detail (Paper III). On c-plane sapphire, tilted ZnO nanowires align with a buried and inclined substrate plane. Contrary to previous reports, it has been revealed that the wires can adapt two degenerate epitaxial configurations with the substrate. Calculations indicate that this degeneracy is caused by equally low lattice mismatches of the two configurations and that tilted nano-

wire growth on c-plane sapphire is energetically preferred over vertical wires. The study has also revealed the epitaxial relationship of triangular ZnO nanosheets with a-plane sapphire substrates. Interestingly, a direct correlation between the nanostructure morphology (i.e. nanowire or nanosheet) and the epitaxial configuration with the substrate has been observed.

The results on ZnO nanostructures presented in this work demonstrate the influence of substrate properties such as crystal orientation and surface morphology on the formation of ZnO nanostructures. The substrate can have significant impact on the nanostructure size, density, orientation and morphology. Moreover, further light has been shed on the role of ambient oxygen during the growth of ZnO nanostructures and its impact on nanostructure morphology. The findings presented in this thesis demonstrate that a fundamental understanding of the essential processes of nanostructure formation is necessary in order to gain control over ZnO nanostructure growth. It forms the basis for reproducible fabrication of ordered ZnO nanostructure arrays with controlled morphologies and growth orientations. In order to complete the picture, further studies addressing the influence of other growth parameters such as absolute pressure or the energy of adatoms (supplied by substrate temperature as well as kinetic energy of impinging growth species) will be of interest.

As a second aspect of this thesis, AZO thin films have been grown by PLD on GaAs substrates. The films grown at room temperature under optimized conditions have shown resistivities competitive to ITO on the order of 10^{-4} Ωcm while retaining high optical transmission in the visible wavelength range. The results for AZO thin films on GaAs substrates have been compared with previous reports on transparent substrates such as glass or sapphire. At growth temperatures reaching 500°C, the GaAs substrate seems to have significant influence on the electrical properties of AZO thin films. However, the good electrical and optical properties indicate that AZO thin films grown at low temperatures are promising candidates for use as transparent electrodes on GaAs nanowire solar cells. This potential of AZO for this type of application should be confirmed directly by investigating the GaAs/AZO-core/shell system. Electron-beam lithographic techniques and a Ti/Au metal layer system could be used to prepare ohmic contacts to single AZO shells on insulating GaAs nanowires and directly establish the electrical properties of the AZO shells as has been initiated already in preliminary experiments during the final phase of this thesis work.

Bibliography

[1] Arico, A. S., Bruce, P., Scrosati, B., Tarascon, J.-M., and van Schalkwijk, W. *Nature Materials* **4**, 366–377 (2005).

[2] Intel Corporation. *3rd Generation Intel®Core™Processors Bring Exciting New Experiences and Fun to the PC*, Press release (23.04.2012).

[3] Kharissova, O., Kharisov, B., Garcia, T., and Mendez, U. *Synthesis and Reactivity in Inorganic, Metal-Organic and Nano-Metal Chemistry* **39**, 662–684 (2009).

[4] Shen, G., Bando, Y., and Lee, C.-J. *The Journal of Physical Chemistry B* **109**, 10779–10785 (2005).

[5] Wang, Z. L. *Journal of Physics: Condensed Matter* **16**, R829–R858 (2004).

[6] Ashraf, S., Jones, A. C., Bacsa, J., Steiner, A., Chalker, P. R., Beahan, P., Hindley, S., Odedra, R., Williams, P. A., and Heys, P. N. *Chemical Vapor Deposition* **17**, 45–53 (2011).

[7] Dick, K. A. *Progress in Crystal Growth and Characterization of Materials* **54**, 138–173 (2008).

[8] Greene, L. E., Law, M., Goldberger, J., Kim, F., Johnson, J. C., Zhang, Y., Saykally, R. J., and Yang, P. *Angewandte Chemie Internationale Edition* **42**, 3031–3034 (2003).

[9] Wang, N., Cai, Y., and Zhang, R. *Materials Science and Engineering: R: Reports* **60**, 1 – 51 (2008).

[10] The Project on Emerging Nanotechnologies (PEN). *Consumer Products Inventory*, http://www.nanotechproject.org/inventories/consumer/, accessed June 2012.

[11] Moezzi, A., McDonagh, A. M., and Cortie, M. B. *Chemical Engineering Journal* **185 - 186**, 1 – 22 (2012).

[12] Klingshirn, C. *physica status solidi (b)* **244**, 3027–3073 (2007).

[13] Klingshirn, C. *ChemPhysChem* **8**, 782–803 (2007).

[14] Willander, M., Nur, O., Zhao, Q. X., Yang, L. L., Lorenz, M., Cao, B. Q., Zuniga-Perez, J., Czekalla, C., Zimmermann, G., Grundmann, M., Bakin, A., Behrends, A., Al-Suleiman, M., El-Shaer, A., Mofor, A. C., Postels, B., Waag, A., Boukos, N., Travlos, A., Kwack, H. S., Guinard, J., and Dang, D. L. S. *Nanotechnology* **20**, 332001 (2009).

[15] Wang, Z. L., Kong, X. Y., and Zuo, J. M. *Physical Review Letters* **91**, 185502 (2003).

[16] Wang, Z. L., Yang, R., Zhou, J., Qin, Y., Xu, C., Hu, Y., and Xu, S. *Materials Science and Engineering: R: Reports* **70**, 320 – 329 (2010).

[17] Lee, C., Lee, T., Lyu, S., Zhang, Y., Ruh, H., and Lee, H. *Applied Physics Letters* **81**, 3648–3650 (2002).

[18] Morkoç, H. and Özgür, m. *General Properties of ZnO*, chapter 1, 1–76. Wiley-VCH Verlag GmbH & Co. KGaA (2009).

[19] Minami, T. *Semiconductor Science and Technology* **20**, S35 (2005).

[20] Desgreniers, S. *Physical Review B* **58**, 14102–14105 (1998).

[21] Kihara, K. and Donnay, G. *Canadian Mineralogist* **23**, 647–654 (1985).

[22] Momma, K. and Izumi, F. *Journal of Applied Crystallography* **44**, 1272–1276 (2011).

[23] Birkholz, D. M. *Thin Film Analysis by X-Ray Scattering*. IHP Microelectronics GmbH, Im Technologiepark 25, 15236 Frankfurt (Oder), Germany, (2006).

[24] Wang, Z., Kong, X., Ding, Y., Gao, P., Hughes, W., Yang, R., and Zhang, Y. *Advanced Functional Materials* **14**, 943–956 (2004).

[25] Tasker, P. W. *Journal of Physics C: Solid State Physics* **12**, 4977 (1979).

[26] Meyer, B. and Marx, D. *Physical Review B* **67**, 035403 (2003).

[27] Claeyssens, F., Freeman, C. L., Allan, N. L., Sun, Y., Ashfold, M. N. R., and Harding, J. H. *Journal of Materials Chemistry* **15**, 139–148 (2005).

[28] Wöll, C. *Progress in Surface Science* **82**, 55–120 (2007).

[29] Noguera, C. *Journal of Physics: Condensed Matter* **12**, R367 (2000).

[30] Goniakowski, J., Finocchi, F., and Noguera, C. *Reports on Progress in Physics* **71**, 016501 (2008).

[31] Laudise, R. A. and Ballman, A. A. *The Journal of Physical Chemistry* **64**, 688–691 (1960).

[32] Heiland, G., Mollwo, E., and StÃűckmann, F. volume 8 of *Solid State Physics*, 191 – 323. Academic Press (1959).

[33] Janotti, A. and de Walle, C. G. V. *Applied Physics Letters* **87**, 122102 (2005).

[34] Kohan, A., Ceder, G., Morgan, D., and Van De Walle, C. *Physical Review B - Condensed Matter and Materials Physics* **61**, 15019–15027 (2000).

[35] Vanheusden, K., Seager, C. H., Warren, W. L., Tallant, D. R., and Voigt, J. A. *Applied Physics Letters* **68**, 403–405 (1996).

[36] Janotti, A. and Van de Walle, C. G. *Nature Materials* **6**, 44–47 (2007).

[37] Noh, J. H., An, J.-S., Kim, J. Y., Cho, C. M., Hong, K. S., and Jung, H. S. *Journal of Electroceramics* **23**, 497–501 (2009).

[38] Papadopoulou, E. L., Varda, M., Kouroupls-Agalou, K., Androulidaki, M., Chikoidze, E., Galtier, P., Huyberechts, G., and Aperathitis, E. *Thin Solid Films* **516**, 8141–8145 (2008).

[39] Steinhauser, J., Fay, S., Oliveira, N., Vallat-Sauvain, E., and Ballif, C. *Applied Physics Letters* **90**, 142107 (2007).

[40] Matsubara, K., Fons, P., Iwata, K., Yamada, A., Sakurai, K., Tampo, H., and Niki, S. *Thin Solid Films* **431-432**, 36–372 (2003).

[41] Suzuki, A., Matsushita, T., Wada, N., Sakamoto, Y., and Okuda, M. *Japanese Journal of Applied Physics, Part 2: Letters* **35**, L56–L59 (1996).

[42] Park, K. C., Ma, D. Y., and Kim, K. H. *Thin Solid Films* **305**, 201 – 209 (1997).

[43] Sakai, N., Umeda, Y., Mitsugi, F., and Ikegami, T. *Surface and Coatings Technology* **202**, 5467 – 5470 (2008).

[44] Liu, Z. F., Shan, F. K., Li, Y. X., Shin, B. C., and Yu, Y. S. *Journal of Crystal Growth* **259**, 130–136 (2003).

[45] Major, S. and Chopra, K. *Solar Energy Materials* **17**, 319 – 327 (1988).

[46] Kumar, P. M. R., Kartha, C. S., Vijayakumar, K. P., Abe, T., Kashiwaba, Y., Singh, F., and Avasthi, D. K. *Semiconductor Science and Technology* **20**, 120 (2005).

[47] Xu, H. Y., Liu, Y. C., Mu, R., Shao, C. L., Lu, Y. M., Shen, D. Z., and Fan, X. W. *Applied Physics Letters* **86**, 123107 (2005).

[48] Kim, H., Gilmore, C. M., Horwitz, J. S., Pique, A., Murata, H., Kushto, G. P., Schlaf, R., Kafafi, Z. H., and Chrisey, D. B. *Applied Physics Letters* **76**, 259–261 (2000).

[49] Park, S.-M., Ikegami, T., Ebihara, K., and Shin, P.-K. *Applied Surface Science* **253**, 1522–1527 (2006).

[50] Ellmer, K. *Journal of Physics D: Applied Physics* **34**, 3097 (2001).

[51] Lu, J. G., Ye, Z. Z., Zeng, Y. J., Zhu, L. P., Wang, L., Yuan, J., Zhao, B. H., and Liang, Q. L. *Journal of Applied Physics* **100**, 073741 (2006).

[52] Ellmer, K. and Mientus, R. *Thin Solid Films* **516**, 4620 – 4627 (2008).

[53] Ellmer, K. and Mientus, R. *Thin Solid Films* **516**, 5829 – 5835 (2008).

[54] Bellingham, J. R., Phillips, W. A., and Adkins, C. J. *Journal of Materials Science Letters* **11**, 263–265 (1992).

[55] Vinnichenko, M., Gago, R., Cornelius, S., Shevchenko, N., Rogozin, A., Kolitsch, A., Munnik, F., and Moller, W. *Applied Physics Letters* **96**, 141907 (2010).

[56] Singh, A. V., Mehra, R. M., Yoshida, A., and Wakahara, A. *Journal of Applied Physics* **95**, 3640–3643 (2004).

[57] Liu, Y., Lü, C., Li, M., Liu, J., Zhang, L., Zhang, J., and Yang, B. *Thin Solid Films* **516**, 8507–8512 (2008).

[58] Na, J.-S., Scarel, G., and Parsons, G. N. *The Journal of Physical Chemistry C* **114**, 383–388 (2010).

[59] Park, C., Zhang, S., and Wei, S.-H. *Physical Review B - Condensed Matter and Materials Physics* **66**, 732021 (2002).

[60] Aoki, T., Hatanaka, Y., and Look, D. C. *Applied Physics Letters* **76**, 3257–3258 (2000).

[61] Brandt, M., von Wenckstern, H., Schmidt, H., Rahm, A., Biehne, G., Benndorf, G., Hochmuth, H., Lorenz, M., Meinecke, C., Butz, T., and Grundmann, M. *Journal of Applied Physics* **104**, 013708 (2008).

[62] Wang, P., Chen, N., Yin, Z., Yang, F., Peng, C., Dai, R., and Bai, Y. *Journal of Applied Physics* **100**, 043704 (2006).

[63] Liu, W., Bian, J., Hu, L., Liang, H., Zang, H., Sun, J., Zhao, Z., Liu, A., and Du, G. *Solid State Communications* **142**, 655–658 (2007).

[64] Look, D. C., Reynolds, D. C., Litton, C. W., Jones, R. L., Eason, D. B., and Cantwell, G. *Applied Physics Letters* **81**, 1830–1832 (2002).

[65] Tsukazaki, A., Ohtomo, A., Onuma, T., Ohtani, M., Makino, T., Sumiya, M., Ohtani, K., Chichibu, S. F., Fuke, S., Segawa, Y., Ohno, H., Koinuma, H., and Kawasaki, M. *Nature Materials* **4**, 42–46 (2005).

[66] Barnes, T. M., Olson, K., and Wolden, C. A. *Applied Physics Letters* **86**, 112112 (2005).

[67] Zeng, Y. J., Ye, Z. Z., Xu, W. Z., Li, D. Y., Lu, J. G., Zhu, L. P., and Zhao, B. H. *Applied Physics Letters* **88**, 062107 (2006).

[68] Lin, S., Lu, J., Ye, Z., He, H., Gu, X., Chen, L., Huang, J., and Zhao, B. *Solid State Communications* **148**, 25 – 28 (2008).

[69] Nakahara, K., Takasu, H., Fons, P., Yamada, A., Iwata, K., Matsubara, K., Hunger, R., and Niki, S. *Applied Physics Letters* **79**, 4139–4141 (2001).

[70] Yamamoto, Tetsuya, K.-Y. H. *Japanese Journal of Applied Physics, Part 2: Letters* **38**, L166–L169 (1999).

[71] Van de Walle, C. G., Laks, D. B., Neumark, G. F., and Pantelides, S. T. *Physical Review B* **47**, 9425–9434 (1993).

[72] Walukiewicz, W. *Physical Review B* **50**, 5221–5225 (1994).

[73] Mariani, G., Wong, P.-S., Katzenmeyer, A. M., Leonard, F., Shapiro, J., and Huffaker, D. L. *Nano Letters* **11**, 2490–2494 (2011).

[74] Rahm, A., Lorenz, M., Nobis, T., Zimmermann, G., Grundmann, M., Fuhrmann, B., and Syrowatka, F. *Applied Physics A: Materials Science & Processing* **88**, 31–34 (2007).

[75] Li, Y., Meng, G. W., Zhang, L. D., and Phillipp, F. *Applied Physics Letters* **76**, 2011–2013 (2000).

[76] Liu, C., Zapien, J., Yao, Y., Meng, X., Lee, C., Fan, S., Lifshitz, Y., and Lee, S. *Advanced Materials* **15**, 838–841 (2003).

[77] Smith, D. L. *Thin-Film Deposition: Principles and Practice*. McGraw-Hill Professional, New York, 1 edition, (1995).

[78] Adams, J. *Nucleation and growth of thin films*. University of Wisconsin–Madison, (1987).

[79] Markov, I. *Crystal growth for beginners: fundamentals of nucleation, crystal growth and epitaxy*. World Scientific, (2003).

[80] Venables, J. A., Spiller, G. D. T., and Hanbucken, M. *Reports on Progress in Physics* **47**, 399 (1984).

[81] Mofor, A., Bakin, A., Elshaer, A., Fuhrmann, D., Bertram, F., Hangleiter, A., Christen, J., and Waag, A. *Applied Physics A: Materials Science & Processing* **88**, 17–20 (2007).

[82] Huang, X., Li, G., Sun, G., Dou, X., Li, L., and Zheng, L. *Nanoscale Research Letters* **5**, 1057–1062 (2010).

[83] Khelladi, M., Mentar, L., Boubatra, M., and Azizi, A. *Materials Letters* **67**, 331–333 (2012).

[84] Wagner, R. S. and Ellis, W. C. *Applied Physics Letters* **4**, 89–90 (1964).

[85] Westwater, J., Gosain, D. P., Tomiya, S., Usui, S., and Ruda, H. *Journal of Vacuum Science & Technology B: Microelectronics and Nanometer Structures* **15**, 554–557 (1997).

[86] Morales, A. M. and Lieber, C. M. *Science* **279**, 208–211 (1998).

[87] Hiruma, K., Yazawa, M., Katsuyama, T., Ogawa, K., Haraguchi, K., Koguchi, M., and Kakibayashi, H. *Journal of Applied Physics* **77**, 447–462 (1995).

[88] Yazawa, M., Koguchi, M., Muto, A., Ozawa, M., and Hiruma, K. *Applied Physics Letters* **61**, 2051–2053 (1992).

[89] Ohlsson, B. J., Bjork, M. T., Magnusson, M. H., Deppert, K., Samuelson, L., and Wallenberg, L. R. *Applied Physics Letters* **79**, 3335–3337 (2001).

[90] Duan, X. and Lieber, C. M. *Advanced Materials* **12**, 298–302 (2000).

[91] Nguyen, P., Ng, H., and Meyyappan, M. *Advanced Materials* **17**, 1773–1777 (2005).

[92] Xia, Y., Yang, P., Sun, Y., Wu, Y., Mayers, B., Gates, B., Yin, Y., Kim, F., and Yan, H. *Advanced Materials* **15**, 353–389 (2003).

[93] Yanagida, T., Nagashima, K., Tanaka, H., and Kawai, T. *Applied Physics Letters* **91**, 061502 (2007).

[94] Nagashima, K., Yanagida, T., Oka, K., Tanaka, H., and Kawai, T. *Applied Physics Letters* **93**, 153103 (2008).

[95] Kamins, T. I., Williams, R. S., Basile, D. P., Hesjedal, T., and Harris, J. S. *Journal of Applied Physics* **89**, 1008–1016 (2001).

[96] Dick, K. A., Deppert, K., Martensson, T., Mandl, B., Samuelson, L., and Seifert, W. *Nano Letters* **5**, 761–764 (2005).

[97] Kirkham, M., Wang, X., Wang, Z. L., and Snyder, R. L. *Nanotechnology* **18**, 365304 (2007).

[98] Hofmann, S., Sharma, R., Wirth, C. T., Cervantes-Sodi, F., Ducati, C., Kasama, T., Dunin-Borkowski, R. E., Drucker, J., Bennett, P., and Robertson, J. *Nature Materials* **7**, 372–375 (2008).

[99] Kodambaka, S., Tersoff, J., Reuter, M. C., and Ross, F. M. *Science* **316**, 729–732 (2007).

[100] Beszeda, I., Szabó, I., and Gontier-Moya, E. *Applied Physics A: Materials Science & Processing* **78**, 1079–1084 (2004).

[101] Wacaser, B. A., Dick, K. A., Johansson, J., Borgström, M. T., Deppert, K., and Samuelson, L. *Advanced Materials* **21**, 153–165 (2008).

[102] Wen, C.-Y., Reuter, M. C., Tersoff, J., Stach, E. A., and Ross, F. M. *Nano Letters* **10**, 514–519 (2010).

[103] Wen, C.-Y., Reuter, M. C., Bruley, J., Tersoff, J., Kodambaka, S., Stach, E. A., and Ross, F. M. *Science* **326**, 1247–1250 (2009).

[104] Roest, A. L., Verheijen, M. A., Wunnicke, O., Serafin, S., Wondergem, H., and Bakkers, E. P. A. M. *Nanotechnology* **17**, S271 (2006).

[105] Allen, J. E., Hemesath, E. R., Perea, D. E., Lensch-Falk, J. L., Li, Z., Yin, F., Gass, M. H., Wang, P., Bleloch, A. L., Palmer, R. E., and Lauhon, L. J. *Nature Nanotechnology* **3**, 168–173 (2008).

[106] Dang, H. Y., Wang, J., and Fan, S. S. *Nanotechnology* **14**, 738 (2003).

[107] Cirlin, G. E., Dubrovskii, V. G., Samsonenko, Y. B., Bouravleuv, A. D., Durose, K., Proskuryakov, Y. Y., Mendes, B., Bowen, L., Kaliteevski, M. A., Abram, R. A., and Zeze, D. *Physical Review B* **82**, 035302 (2010).

[108] Bierman, M. J., Lau, Y. K. A., Kvit, A. V., Schmitt, A. L., and Jin, S. *Science* **320**, 1060–1063 (2008).

[109] Sears, G. *Acta Metallurgica* **3**, 361 – 366 (1955).

[110] Sears, G. *Acta Metallurgica* **3**, 367 – 369 (1955).

[111] Jin, S., Bierman, M. J., and Morin, S. A. *The Journal of Physical Chemistry Letters* **1**, 1472–1480 (2010).

[112] Li, Y. and Wu, Y. *Chemistry of Materials* **22**, 5537–5542 (2010).

[113] Li, C., Fang, G., Fu, Q., Su, F., Li, G., Wu, X., and Zhao, X. *Journal of Crystal Growth* **292**, 19–25 (2006).

[114] Park, W. I., Kim, D. H., Jung, S.-W., and Yi, G.-C. *Applied Physics Letters* **80**, 4232–4234 (2002).

[115] Park, D. J., Kim, D. C., Lee, J. Y., and Cho, H. K. *Nanotechnology* **17**, 5238 (2006).

[116] Li, C., Fang, G., Li, J., Ai, L., Dong, B., and Zhao, X. *The Journal of Physical Chemistry C* **112**, 990–995 (2008).

[117] Ho, S.-T., Wang, C.-Y., Liu, H.-L., and Lin, H.-N. *Chemical Physics Letters* **463**, 141–144 (2008).

[118] Amarilio-Burshtein, I., Tamir, S., and Lifshitz, Y. *Applied Physics Letters* **96**, 103104 (2010).

[119] Kim, H., Shim, S., and Lee, J. *Journal of Nanoscience and Nanotechnology* **8**, 2554–2559 (2008).

[120] Kim, D. S., Scholz, R., Gösele, U., and Zacharias, M. *Small* **4**, 1615–1619 (2008).

[121] Hartanto, A., Ning, X., Nakata, Y., and Okada, T. *Applied Physics A: Materials Science & Processing* **78**, 299–301 (2004).

[122] Lee, Y.-J., Sounart, T. L., Scrymgeour, D. A., Voigt, J. A., and Hsu, J. W. *Journal of Crystal Growth* **304**, 80–85 (2007).

[123] Greene, L. E., Law, M., Tan, D. H., Montano, M., Goldberger, J., Somorjai, G., and Yang, P. *Nano Letters* **5**, 1231–1236 (2005).

[124] Chen, H.-G., Li, Z.-W., and Lian, H.-D. *Thin Solid Films* **518**, 5520–5524 (2010).

[125] Zou, G., Li, H., Zhang, Y., Xiong, K., and Qian, Y. *Nanotechnology* **17**, S313 (2006).

[126] Hulteen, J. C. and Martin, C. *Journal of Materials Chemistry* **7**, 1075–1087 (1997).

[127] Goldberger, J., He, R., Zhang, Y., Lee, S., Yan, H., Choi, H.-J., and Yang, P. *Nature* **422**, 599–602 (2003).

[128] Zhang, Y., Jia, H., Wang, R., Chen, C., Luo, X., Yu, D., and Lee, C. *Applied Physics Letters* **83**, 4631–4633 (2003).

[129] Wu, G., Xie, T., Yuan, X., Li, Y., Yang, L., Xiao, Y., and Zhang, L. *Solid State Communications* **134**, 485 – 489 (2005).

[130] Martinson, A. B. F., Elam, J. W., Hupp, J. T., and Pellin, M. J. *Nano Letters* **7**, 2183–2187 (2007).

[131] Li, L., Pan, S., Dou, X., Zhu, Y., Huang, X., Yang, Y., Li, G., and Zhang, L. *The Journal of Physical Chemistry C* **111**, 7288–7291 (2007).

[132] Cao, G. and Liu, D. *Advances in Colloid and Interface Science* **136**, 45 – 64 (2008).

[133] Olson, D. C., Piris, J., Collins, R. T., Shaheen, S. E., and Ginley, D. S. *Thin Solid Films* **496**, 26–29 (2006).

[134] Fan, H. J., Lee, W., Hauschild, R., Alexe, M., Lehun, G., Scholz, R., Dadgar, A., Nielsch, K., Kalt, H., Krost, A., Zacharias, M., and Gösele, U. *Small* **2**, 561–568 (2006).

[135] Shang, H. M. and Cao, G. In *Springer Handbook of Nanotechnology,* Bhushan, B., editor, 169–186. Springer Berlin Heidelberg (2010).

[136] Ye, C., Fang, X., Hao, Y., Teng, X., and Zhang, L. *The Journal of Physical Chemistry B* **109**, 19758–19765 (2005).

[137] Dalal, S. H., Baptista, D. L., Teo, K. B. K., Lacerda, R. G., Jefferson, D. A., and Milne, W. I. *Nanotechnology* **17**, 4811–4818 (2006).

[138] Shin, J. H., Song, J. Y., and Park, H. M. *Materials Letters* **63**, 145–147 (2009).

[139] Song, J., Wang, X., Riedo, E., and Wang, Z. L. *The Journal of Physical Chemistry B* **109**, 9869–9872 (2005).

[140] Li, S. Y., Lee, C. Y., and Tseng, T. Y. *Journal of Crystal Growth* **247**, 357–362 (2003).

[141] Huang, M. H., Wu, Y., Feick, H., Tran, N., Weber, E., and Yang, P. *Advanced Materials* **13**, 113–116 (2001).

[142] Huang, M. H., Mao, S., Feick, H., Yan, H., Wu, Y., Kind, H., Weber, E., Russo, R., and Yang, P. *Science* **292**, 1897–1899 (2001).

[143] Nikoobakht, B., Eustis, S., and Herzing, A. *The Journal of Physical Chemistry C* **113**, 7031–7037 (2009).

[144] Jie, J., Wang, G., Chen, Y., Han, X., Wang, Q., Xu, B., and Hou, J. G. *Applied Physics Letters* **86**, 031909 (2005).

[145] Geng, C., Jiang, Y., Yao, Y., Meng, X., Zapien, J., Lee, C., Lifshitz, Y., and Lee, S. *Advanced Functional Materials* **14**, 589–594 (2004).

[146] Liu, Z., Zhang, D., Li, C., and Zhou, C. In *Nanotechnology, 2003. IEEE-NANO 2003. 2003 Third IEEE Conference on*, volume 2, 592–595 vol. 2, (2003).

[147] Sun, Y., Fuge, G. M., and Ashfold, M. N. R. *Superlattices and Microstructures* **39**, 33–40 (2006).

[148] Liu, Z. W., Ong, C. K., Yu, T., and Shen, Z. X. *Applied Physics Letters* **88**, 053110 (2006).

[149] Choopun, S., Tabata, H., and Kawai, T. *Journal of Crystal Growth* **274**, 167–172 (2005).

[150] Doherty, R., Sun, Y., Sun, Y., Warren, J., Fox, N., Cherns, D., and Ashfold, M. *Applied Physics A: Materials Science & Processing* **89**, 49–55 (2007).

[151] Zuniga-Perez, J., Rahm, A., Czekalla, C., Lenzner, J., Lorenz, M., and Grundmann, M. *Nanotechnology* **18**, 195303 (2007).

[152] Nishimura, R., Sakano, T., Okato, T., Saiki, T., and Obara, M. *Japanese Journal of Applied Physics* **47**, 4799–4802 (2008).

[153] Kawakami, M., Hartanto, A. B., Nakata, Y., and Okada, T. *Japanese Journal of Applied Physics* **42**, L33–L35 (2003).

[154] McLoughlin, C., Hough, P., Costello, J., and Mosnier, J.-P. *Applied Surface Science* **255**, 5338–5341 (2009).

[155] Park, J.-H., Hwang, I.-S., Choi, Y.-J., and Park, J.-G. *Journal of Crystal Growth* **276**, 171–176 (2005).

[156] Pierson, H. *Handbook of Chemical Vapor Deposition (CVD): Principles, Technology, and Applications*. Materials science, process technology and semiconductors. Noyes Publications/William Andrew Pub., (1999).

[157] Falyouni, F., Benmamas, L., Thiandoume, C., Barjon, J., Lusson, A., Galtier, P., and Sallet, V. *Journal of Vacuum Science & Technology B* **27**, 1662–1666 (2009).

[158] Chen, H.-G., Jian, S.-R., Li, Z.-W., Chen, K.-W., and Li, J.-C. *Journal of Alloys and Compounds* **504**, S368–S371 (2010).

[159] Park, W., Yi, G.-C., Kim, M., and Pennycook, S. *Advanced Materials* **14**, 1841–1843 (2002).

[160] Kim, D. C., Kong, B. H., Cho, H. K., Park, D. J., and Lee, J. Y. *Nanotechnology* **18**, 015603 (2007).

[161] Kwak, C.-H., Kim, B.-H., Park, S.-H., Seo, S.-Y., Park, C.-I., Kim, S.-H., and Han, S.-W. *Journal of Crystal Growth* **311**, 4491 – 4494 (2009).

[162] Maejima, K., Ueda, M., Fujita, S., and Fujita, S. *Japanese Journal of Applied Physics* **42**, 2600–2604 (2003).

[163] Liu, X., Wu, X., Cao, H., and Chang, R. P. H. *Journal of Applied Physics* **95**, 3141–3147 (2004).

[164] Park, W. I., Lee, C.-H., Chae, J. H., Lee, D. H., and Yi, G.-C. *Small* **5**, 181–184 (2009).

[165] Zhang, G., Nakamura, A., Aoki, T., Temmyo, J., and Matsui, Y. *Applied Physics Letters* **89**, 113112 (2006).

[166] Weintraub, B., Zhou, Z., Li, Y., and Deng, Y. *Nanoscale* **2**, 1573–1587 (2010).

[167] Xu, F. and Sun, L. *Energy & Environmental Science* **4**, 818–841 (2011).

[168] Vayssieres, L. *Advanced Materials* **15**, 464–466 (2003).

[169] Wang, J. and Gao, L. *Journal of Materials Chemistry* **13**, 2551–2554 (2003).

[170] Henley, S. J., Ashfold, M. N. R., Nicholls, D. P., Wheatley, P., and Cherns, D. *Applied Physics A* **79**, 1169–1173 (2004).

[171] Guo, M., Diao, P., Wang, X., and Cai, S. *Journal of Solid State Chemistry* **178**, 3210–3215 (2005).

[172] Vayssieres, L., Keis, K., Lindquist, S.-E., and Hagfeldt, A. *The Journal of Physical Chemistry B* **105**, 3350–3352 (2001).

[173] Law, M., Greene, L. E., Johnson, J. C., Saykally, R., and Yang, P. *Nature Materials* **4**, 455–459 (2005).

[174] Ma, T., Guo, M., Zhang, M., Zhang, Y., and Wang, X. *Nanotechnology* **18** (2007).

[175] Song, J. and Lim, S. *The Journal of Physical Chemistry C* **111**, 596–600 (2007).

[176] Chen, S.-W. and Wu, J.-M. *Acta Materialia* **59**, 841–847 (2011).

[177] Zheng, M., Zhang, L., Li, G., and Shen, W. *Chemical Physics Letters* **363**, 123 – 128 (2002).

[178] Wong, M. H., Berenov, A., Qi, X., Kappers, M. J., Barber, Z. H., Illy, B., Lockman, Z., Ryan, M. P., and MacManus-Driscoll, J. L. *Nanotechnology* **14**, 968 (2003).

[179] Postels, B., Bakin, A., Wehmann, H.-H., Suleiman, M., Weimann, T., Hinze, P., and Waag, A. *Applied Physics A: Materials Science & Processing* **91**, 595–599 (2008).

[180] Illy, B., Shollock, B. A., MacManus-Driscoll, J. L., and Ryan, M. P. *Nanotechnology* **16**, 320 (2005).

[181] Xu, L., Guo, Y., Liao, Q., Zhang, J., and Xu, D. *The Journal of Physical Chemistry B* **109**, 13519–13522 (2005).

[182] Wu, L., Song, F., Fang, X., Guo, Z.-X., and Liang, S. *Nanotechnology* **21**, 475502 (2010).

[183] Olson, D. C., Lee, Y.-J., White, M. S., Kopidakis, N., Shaheen, S. E., Ginley, D. S., Voigt, J. A., and Hsu, J. W. P. *The Journal of Physical Chemistry C* **111**, 16640–16645 (2007).

[184] Takanezawa, K., Hirota, K., Wei, Q.-S., Tajima, K., and Hashimoto, K. *The Journal of Physical Chemistry C* **111**, 7218–7223 (2007).

[185] Galoppini, E., Rochford, J., Chen, H., Saraf, G., Lu, Y., Hagfeldt, A., and Boschloo, G. *The Journal of Physical Chemistry B* **110**, 16159–16161 (2006).

[186] Gonzalez-Valls, I. and Lira-Cantu, M. *Energy & Environmental Science* **2**, 19–34 (2009).

[187] Zhang, Q., Dandeneau, C. S., Zhou, X., and Cao, G. *Advanced Materials* **21**, 4087–4108 (2009).

[188] Goldberger, J., Sirbuly, D. J., Law, M., and Yang, P. *The Journal of Physical Chemistry B* **109**, 9–14 (2005).

[189] Ng, H. T., Han, J., Yamada, T., Nguyen, P., Chen, Y. P., and Meyyappan, M. *Nano Letters* **4**, 1247–1252 (2004).

[190] Kälblein, D., Weitz, R. T., Böttcher, H. J., Ante, F., Zschieschang, U., Kern, K., and Klauk, H. *Nano Letters* **11**, 5309–5315 (2011).

[191] Lin, Z. and Wang. *Nano Today* **5**, 540 – 552 (2010).

[192] Fan, Z. Y., Wang, D. W., Chang, P. C., Tseng, W. Y., and Lu, J. G. *Applied Physics Letters* **85**, 5923–5925 (2004).

[193] Wan, Q., Li, Q. H., Chen, Y. J., Wang, T. H., He, X. L., Li, J. P., and Lin, C. L. *Applied Physics Letters* **84**, 3654–3656 (2004).

[194] Park, J. Y., Song, D. E., and Kim, S. S. *Nanotechnology* **19**, 105503 (2008).

[195] Rout, C. S., Krishna, S. H., Vivekchand, S., Govindaraj, A., and Rao, C. *Chemical Physics Letters* **418**, 586 – 590 (2006).

[196] Fan, Z. and Lu, J. G. *Applied Physics Letters* **86**, 123510 (2005).

[197] Choi, A., Kim, K., Jung, H.-I., and Lee, S. Y. *Sensors and Actuators B: Chemical* **148**, 577 – 582 (2010).

[198] Johnson, J. C., Yan, H., Schaller, R. D., Haber, L. H., Saykally, R. J., and Yang, P. *The Journal of Physical Chemistry B* **105**, 11387–11390 (2001).

[199] Zimmler, M. A., Capasso, F., Müller, S., and Ronning, C. *Semiconductor Science and Technology* **25**, 024001 (2010).

[200] Könenkamp, R., Word, R. C., and Schlegel, C. *Applied Physics Letters* **85**, 6004–6006 (2004).

[201] Könenkamp, R., Word, R. C., and Godinez, M. *Nano Letters* **5**, 2005–2008 (2005).

[202] Kishwar, S., ul Hasan, K., Alvi, N., Klason, P., Nur, O., and Willander, M. *Superlattices and Microstructures* **49**, 32 – 42 (2011).

[203] Özgür, U., Hofstetter, D., and Morkoç, H. *Proceedings of the IEEE* **98**, 1255 –1268 (2010).

[204] Chu, S., Wang, G., Zhou, W., Lin, Y., Chernyak, L., Zhao, J., Kong, J., Li, L., Ren, J., and Liu, J. *Nature Nanotechnology* **6**, 506–510 (2011).

[205] Wang, Z. L. *Journal of Nanoscience and Nanotechnology* **8**, 27–55 (2008).

[206] Wang, Z. L. *Materials Science and Engineering: R: Reports* **64**, 33–71 (2009).

[207] Pan, Z. W., Dai, Z. R., and Wang, Z. L. *Science* **291**, 1947–1949 (2001).

[208] Yao, B. D., Chan, Y. F., and Wang, N. *Applied Physics Letters* **81**, 757–759 (2002).

[209] Dai, Z., Pan, Z., and Wang, Z. *Advanced Functional Materials* **13**, 9–24 (2003).

[210] Borchers, C., Müller, S., Stichtenoth, D., Schwen, D., and Ronning, C. *The Journal of Physical Chemistry B* **110**, 1656–1660 (2006).

[211] Ding, Y., Gao, P. X., and Wang, Z. L. *Journal of the American Chemical Society* **126**, 2066–2072 (2004).

[212] Xing, G. Z., Fang, X. S., Zhang, Z., Wang, D. D., Huang, X., Guo, J., Liao, L., Zheng, Z., Xu, H. R., Yu, T., Shen, Z. X., Huan, C. H. A., Sum, T. C., Zhang, H., and Wu, T. *Nanotechnology* **21**, 255701 (2010).

[213] Sun, T., Qiu, J., and Liang, C. *The Journal of Physical Chemistry C* **112**, 715–721 (2008).

[214] Jie, J., Wang, G., Han, X., Yu, Q., Liao, Y., Li, G., and Hou, J. *Chemical Physics Letters* **387**, 466 – 470 (2004).

[215] Fan, H. J., Fuhrmann, B., Scholz, R., Himcinschi, C., Berger, A., Leipner, H., Dadgar, A., Krost, A., Christiansen, S., Gösele, U., and Zacharias, M. *Nanotechnology* **17**, S231 (2006).

[216] Yang, Q., Tang, K., Zuo, J., and Qian, Y. *Applied Physics A: Materials Science & Processing* **79**, 1847–1851 (2004).

[217] Kirkham, M., Wang, Z. L., and Snyder, R. L. *Nanotechnology* **19**, 445708 (2008).

[218] Wen, X., Fang, Y., Pang, Q., Yang, C., Wang, J., Ge, W., Wong, K. S., and Yang, S. *The Journal of Physical Chemistry B* **109**, 15303–15308 (2005).

[219] Zhang, X., Dai, J., Ong, H., Wang, N., Chan, H., and Choy, C. *Chemical Physics Letters* **393**, 17 – 21 (2004).

[220] Hattori, A., Ono, A., and Tanaka, H. *Nanotechnology* **22** (2011).

[221] Choopun, S., Hongsith, N., Tanunchai, S., Chairuangsri, T., Krua-in, C., Singkarat, S., Vilaithong, T., Mangkorntong, P., and Mangkorntong, N. *Journal of Crystal Growth* **282**, 365 – 369 (2005).

[222] Yang, J., Liu, G., Lu, J., Qiu, Y., and Yang, S. *Applied Physics Letters* **90**, 103109 (2007).

[223] Cheng, H., Cheng, J., Zhang, Y., and Wang, Q.-M. *Journal of Crystal Growth* **299**, 34–40 (2007).

[224] Yan, Y., Liu, P., Wen, J. G., To, B., and Al-Jassim, M. M. *The Journal of Physical Chemistry B* **107**, 9701–9704 (2003).

[225] Arnold, M. S., Avouris, P., Pan, Z. W., and Wang, Z. L. *The Journal of Physical Chemistry B* **107**, 659–663 (2003).

[226] Wang, W., Zeng, B., Yang, J., Poudel, B., Huang, J., Naughton, M., and Ren, Z. *Advanced Materials* **18**, 3275–3278 (2006).

[227] Lao, C. S., Liu, J., Gao, P., Zhang, L., Davidovic, D., Tummala, R., and Wang, Z. L. *Nano Letters* **6**, 263–266 (2006).

[228] Choopun, S., Tubtimtae, A., Santhaveesuk, T., Nilphai, S., Wongrat, E., and Hongsith, N. *Applied Surface Science* **256**, 998 – 1002 (2009).

114

[229] Cao, B. Q., Sakai, K., Nakamura, D., Palani, I. A., Gong, H. B., Xu, H. Y., Higashihata, M., and Okada, T. *The Journal of Physical Chemistry C* **115**, 1702–1707 (2011).

[230] Bando, K., Sawabe, T., Asaka, K., and Masumoto, Y. *Journal of Luminescence* **108**, 385 – 388 (2004).

[231] He, J. H., Ho, C. H., and Chen, C. Y. *Nanotechnology* **20**, 065503 (2009).

[232] Sadek, A., Choopun, S., Wlodarski, W., Ippolito, S., and Kalantar-zadeh, K. *Sensors Journal* **7**, 919–924 (2007).

[233] Choopun, S., Hongsith, N., Mangkorntong, P., and Mangkorntong, N. *Physica E: Low-dimensional Systems and Nanostructures* **39**, 53 – 56 (2007).

[234] Hughes, W. L. and Wang, Z. L. *Applied Physics Letters* **82**, 2886–2888 (2003).

[235] Yuan, B., Zheng, X. J., Chen, Y. Q., Yang, B., and Zhang, T. *Solid-State Electronics* **55**, 49 – 53 (2011).

[236] Lao, C. S., Park, M.-C., Kuang, Q., Deng, Y., Sood, A. K., Polla, D. L., and Wang, Z. L. *Journal of the American Chemical Society* **129**, 12096–12097 (2007).

[237] Ahmad, M., ud Din, R., Pan, C., and Zhu, J. *The Journal of Physical Chemistry C* **114**, 2560–2565 (2010).

[238] Zhao, M.-H., Wang, Z.-L., and Mao, S. X. *Nano Letters* **4**, 587–590 (2004).

[239] Kong, X. Y. and Wang, Z. L. *Nano Letters* **3**, 1625–1631 (2003).

[240] Kong, X. Y., Ding, Y., Yang, R., and Wang, Z. L. *Science* **303**, 1348–1351 (2004).

[241] Wu, X., Qu, F., Zhang, X., Cai, W., and Shen, G. *Journal of Alloys and Compounds* **486**, L13 – L16 (2009).

[242] Wang, Z. L. *Materials Today* **7**, 26 – 33 (2004).

[243] Fuller, M. L. *Journal of Applied Physics* **15**, 164–170 (1944).

[244] Dai, Y., Zhang, Y., Li, Q., and Nan, C. *Chemical Physics Letters* **358**, 83 – 86 (2002).

[245] Newton, M. C. and Warburton, P. A. *Materials Today* **10**, 50 – 54 (2007).

[246] Wang, F., Ye, Z., Ma, D., Zhu, L., and Zhuge, F. *Materials Letters* **59**, 560 – 563 (2005).

[247] Takeuchi, S., Iwanaga, H., and Fujii, M. *Philosophical Magazine A* **69**, 1125–1129 (1994).

[248] Khan, A., Khan, S. N., and Jadwisienczak, W. M. *Science of Advanced Materials* **2**, 572–577 (2010).

[249] Liu, F., Cao, P. J., Zhang, H. R., Li, J. Q., and Gao, H. J. *Nanotechnology* **15**, 949 (2004).

[250] Yan, Y., Zhou, L., Zou, J., and Zhang, Y. *Applied Physics A: Materials Science & Processing* **94**, 559–565 (2009).

[251] Lin, H.-F., Liao, S.-C., and Hu, C.-T. *Journal of Crystal Growth* **311**, 1378 – 1384 (2009).

[252] Chen, L., Song, W., Xie, C., Lin, L., and Wang, J. *Materials Letters* **61**, 4603 – 4605 (2007).

[253] Lupan, O., Chow, L., and Chai, G. *Sensors and Actuators B: Chemical* **141**, 511 – 517 (2009).

[254] Jiang, J., Li, Y., Tan, S., and Huang, Z. *Materials Letters* **64**, 2191 – 2193 (2010).

[255] Chiu, W.-H., Lee, C.-H., Cheng, H.-M., Lin, H.-F., Liao, S.-C., Wu, J.-M., and Hsieh, W.-F. *Energy & Environmental Science* **2**, 694–698 (2009).

[256] Xiangfeng, C., Dongli, J., Djurijic, A. B., and Leung, Y. H. *Chemical Physics Letters* **401**, 426 – 429 (2005).

[257] Wan, Q., Yu, K., Wang, T. H., and Lin, C. L. *Applied Physics Letters* **83**, 2253–2255 (2003).

[258] Li, Q. H., Wan, Q., Chen, Y. J., Wang, T. H., Jia, H. B., and Yu, D. P. *Applied Physics Letters* **85**, 636–638 (2004).

[259] Zheng, K., Shen, H., Li, J., Sun, D., Chen, G., Hou, K., Li, C., and Lei, W. *Vacuum* **83**, 261 – 264 (2008).

[260] Iijima, S. *Nature* **354**, 56–58 (1991).

[261] Kong, T., Chen, Y., Ye, Y., Zhang, K., Wang, Z., and Wang, X. *Sensors and Actuators B: Chemical* **138**, 344 – 350 (2009).

[262] Zhang, X.-H., Xie, S.-Y., Jiang, Z.-Y., Zhang, X., Tian, Z.-Q., Xie, Z.-X., Huang, R.-B., and Zheng, L.-S. *The Journal of Physical Chemistry B* **107**, 10114–10118 (2003).

[263] Kong, X. Y., Ding, Y., and Wang, Z. L. *The Journal of Physical Chemistry B* **108**, 570–574 (2004).

[264] She, G.-W., Zhang, X.-H., Shi, W.-S., Fan, X., Chang, J. C., Lee, C.-S., Lee, S.-T., and Liu, C.-H. *Applied Physics Letters* **92**, 053111 (2008).

[265] Chu, D., Masuda, Y., Ohji, T., and Kato, K. *Langmuir* **26**, 2811–2815 (2010).

[266] Sun, Y., Fuge, G., Fox, N., Riley, D., and Ashfold, M. *Advanced Materials* **17**, 2477–2481 (2005).

[267] Sun, Y., Riley, D. J., and Ashfold, M. N. R. *The Journal of Physical Chemistry B* **110**, 15186–15192 (2006).

[268] Tang, Y., Luo, L., Chen, Z., Jiang, Y., Li, B., Jia, Z., and Xu, L. *Electrochemistry Communications* **9**, 289 – 292 (2007).

[269] Mensah, S. L., Kayastha, V. K., Ivanov, I. N., Geohegan, D. B., and Yap, Y. K. *Applied Physics Letters* **90**, 113108 (2007).

[270] Xing, Y. J., Xi, Z. H., Xue, Z. Q., Zhang, X. D., Song, J. H., Wang, R. M., Xu, J., Song, Y., Zhang, S. L., and Yu, D. P. *Applied Physics Letters* **83**, 1689–1691 (2003).

[271] Kong, X., Sun, X., Li, X., and Li, Y. *Materials Chemistry and Physics* **82**, 997 – 1001 (2003).

[272] Zhang, B. P., Binh, N. T., Wakatsuki, K., Segawa, Y., Yamada, Y., Usami, N., Kawasaki, M., and Koinuma, H. *The Journal of Physical Chemistry B* **108**, 10899–10902 (2004).

[273] Chen, Y.-J., Zhu, C.-L., and Xiao, G. *Sensors and Actuators B: Chemical* **129**, 639 – 642 (2008).

[274] Jensen, R. A., Van Ryswyk, H., She, C., Szarko, J. M., Chen, L. X., and Hupp, J. T. *Langmuir* **26**, 1401–1404 (2010).

[275] Sadaf, J., Israr, M., Kishwar, S., Nur, O., and Willander, M. *Nanoscale Research Letters* **5**, 957–960 (2010).

[276] Wei, A., Sun, X. W., Xu, C. X., Dong, Z. L., Yu, M. B., and Huang, W. *Applied Physics Letters* **88**, 213102 (2006).

[277] Pan, Z. W., Mahurin, S. M., Dai, S., and Lowndes, D. H. *Nano Letters* **5**, 723–727 (2005).

[278] Park, J.-H. and Park, J.-G. *Applied Physics A: Materials Science & Processing* **80**, 43–46 (2005).

[279] Xu, C., Sun, X., Dong, Z., and Yu, M. *Journal of Crystal Growth* **270**, 498 – 504 (2004).

[280] Huang, Y., Zhang, Y., He, J., Dai, Y., Gu, Y., Ji, Z., and Zhou, C. *Ceramics International* **32**, 561 – 566 (2006).

[281] Zhang, Y., Song, X., Zheng, J., Liu, H., Li, X., and You, L. *Nanotechnology* **17**, 1916 (2006).

[282] Yan, H., He, R., Johnson, J., Law, M., Saykally, R. J., and Yang, P. *Journal of the American Chemical Society* **125**, 4728–4729 (2003).

[283] Lao, C. S., Gao, P. X., Yang, R. S., Zhang, Y., Dai, Y., and Wang, Z. L. *Chemical Physics Letters* **417**, 358 – 362 (2006).

[284] Sulieman, K. M., Huang, X., Liu, J., and Tang, M. *Materials Letters* **61**, 1756 – 1759 (2007).

[285] Zhang, Y., Liu, J., Liu, T., You, L., and Li, X. *Journal of Crystal Growth* **285**, 541 – 548 (2005).

[286] Lim, Y., Park, J., Hong, S.-T., and Kim, J. *Materials Science and Engineering: B* **129**, 100 – 103 (2006).

[287] Leung, Y., Djurijic, A., Gao, J., Xie, M., Wei, Z., Xu, S., and Chan, W. *Chemical Physics Letters* **394**, 452 – 457 (2004).

[288] Huo, K., Hu, Y., Fu, J., Wang, X., Chu, P. K., Hu, Z., and Chen, Y. *The Journal of Physical Chemistry C* **111**, 5876–5881 (2007).

[289] Chen, Y. and Chen, Y. *Optics Express* **19**, 8728–8734 (2011).

[290] Xu, F., Yu, K., Li, G., Li, Q., and Zhu, Z. *Nanotechnology* **17**, 2855–2859 (2006).

[291] Umar, A. *Nanoscale Research Letters* **4**, 1004–1008 (2009).

[292] Pandya, H., Chandra, S., and Vyas, A. *Sensors and Transducers* **134**, 85–94 (2011).

[293] Wang, J. X., Sun, X. W., Wei, A., Lei, Y., Cai, X. P., Li, C. M., and Dong, Z. L. *Applied Physics Letters* **88**, 233106 (2006).

[294] Gao, P., Ying, C., Wang, S., Ye, L., Guo, Q., and Xie, Y. *Journal of Nanoparticle Research* **8**, 131–136 (2006).

[295] Long, T., Yin, S., Takabatake, K., Zhnag, P., and Sato, T. *Nanoscale Research Letters* **4**, 247–253 (2008).

[296] Barreca, D., Ferrucci, A., Gasparotto, A., Maccato, C., Maragno, C., and Tondello, E. *Chemical Vapor Deposition* **13**, 618–625 (2007).

[297] Chen, S., Liu, Y., Shao, C., Mu, R., Lu, Y., Zhang, J., Shen, D., and Fan, X. *Advanced Materials* **17**, 586–590 (2005).

[298] Zeng, J. H., Jin, B. B., and Wang, Y. F. *Chemical Physics Letters* **472**, 90 – 95 (2009).

[299] Zhang, H., Yang, D., Li, S., Ma, X., Ji, Y., Xu, J., and Que, D. *Materials Letters* **59**, 1696 – 1700 (2005).

[300] Cao, B., Cai, W., Li, Y., Sun, F., and Zhang, L. *Nanotechnology* **16**, 1734– (2005).

[301] Chin, K. C., Poh, C. K., Chong, G. L., Lin, J., Sow, C. H., and Wee, A. T. S. *Applied Physics A: Materials Science & Processing* **90**, 623–627 (2008).

[302] Deng, Z., Rui, Q., Yin, X., Liu, H., and Tian, Y. *Analytical Chemistry* **80**, 5839–5846 (2008).

[303] Li, L., Yu, K., Peng, D., Zhang, Z., and Zhu, Z. *Applied Surface Science* **256**, 208 – 212 (2009).

[304] Wei, Q., Meng, G., An, X., Hao, Y., and Zhang, L. *Nanotechnology* **16**, 2561 (2005).

[305] Weigand, C., Bergren, M., Ladam, C., Tveit, J., Holmestad, R., Vullum, P.-E., Walmsley, J., Øystein Dahl, Furtak, T., Collins, R., Grepstad, J., and Weman, H. *Crystal Growth & Design* **11**, 5298 – 5304 (2011).

[306] Fu, M. and Zhou, J. *Journal of the Electrochemical Society* **157**, D450–D453 (2010).

[307] Huang, X., Xia, X., Yuan, Y., and Zhou, F. *Electrochimica Acta* **56**, 4960 – 4965 (2011).

[308] Cao, B., Teng, X., Heo, S. H., Li, Y., Cho, S. O., Li, G., and Cai, W. *The Journal of Physical Chemistry C* **111**, 2470–2476 (2007).

[309] Bai, W., Zhu, X., Zhu, Z., and Chu, J. *Applied Surface Science* **254**, 6483 – 6488 (2008).

[310] Sun, H., Luo, M., Weng, W., Cheng, K., Du, P., Shen, G., and Han, G. *Nanotechnology* **19**, 125603 (2008).

[311] Kar, S., Dev, A., and Chaudhuri, S. *The Journal of Physical Chemistry B* **110**, 17848–17853 (2006).

[312] Pradhan, D. and Leung, K. T. *The Journal of Physical Chemistry C* **112**, 1357–1364 (2008).

119

[313] Wang, Y., Fan, X., and Sun, J. *Materials Letters* **63**, 350 – 352 (2009).

[314] Suliman, A. E., Tang, Y., and Xu, L. *Solar Energy Materials and Solar Cells* **91**, 1658 – 1662 (2007).

[315] Min, S.-K., Mane, R. S., Joo, O.-S., Ganesh, T., Cho, B. W., and Han, S.-H. *Current Applied Physics* **9**, 492 – 495 (2009).

[316] Kim, C., Kim, Y.-J., Jang, E.-S., Yi, G.-C., and Kim, H. H. *Applied Physics Letters* **88**, 093104 (2006).

[317] Park, J.-H., Choi, H.-J., Choi, Y.-J., Sohn, S.-H., and Park, J.-G. *Journal of Materials Chemistry* **14**, 35–36 (2004).

[318] Rahm, A., Yang, G., Lorenz, M., Nobis, T., Lenzner, J., Wagner, G., and Grundmann, M. *Thin Solid Films* **486**, 191–194 (2005).

[319] Zhang, X., Zhang, J., Chen, L., Xu, J., You, L., and Yu, D. *Applied Physics A: Materials Science & Processing* **92**, 669–672 (2008).

[320] Heo, Y. W., Varadarajan, V., Kaufman, M., Kim, K., Norton, D. P., Ren, F., and Fleming, P. H. *Applied Physics Letters* **81**, 3046–3048 (2002).

[321] Zhang, C., Zhang, F., Sun, X. W., Yang, Y., Wang, J., and Xu, J. *Optics Letters* **34**, 3349–3351 (2009).

[322] Hu, J. Q., Bando, Y., Zhan, J. H., Li, Y. B., and Sekiguchi, T. *Applied Physics Letters* **83**, 4414–4416 (2003).

[323] Kakiuchi, K., Hosono, E., Kimura, T., Imai, H., and Fujihara, S. *Journal of Sol-Gel Science and Technology* **39**, 63–72 (2006).

[324] Zhang and Yanagisawa, K. *Chemistry of Materials* **19**, 2329–2334 (2007).

[325] Fu, M., Zhou, J., Xiao, Q., Li, B., Zong, R., Chen, W., and Zhang, J. *Advanced Materials* **18**, 1001–1004 (2006).

[326] Rui, Q., Komori, K., Tian, Y., Liu, H., Luo, Y., and Sakai, Y. *Analytica Chimica Acta* **670**, 57 – 62 (2010).

[327] Lu, X., Zhang, H., Ni, Y., Zhang, Q., and Chen, J. *Biosensors and Bioelectronics* **24**, 93 – 98 (2008).

[328] Lin, C.-Y., Lai, Y.-H., Chen, H.-W., Chen, J.-G., Kung, C.-W., Vittal, R., and Ho, K.-C. *Energy & Environmental Science* **4**, 3448–3455 (2011).

[329] Xu, F., Dai, M., Lu, Y., and Sun, L. *The Journal of Physical Chemistry C* **114**, 2776–2782 (2010).

[330] Barreca, D., Gasparotto, A., Maccato, C., Tondello, E., Lavrenătangar, U., and Patil, S. R. *Surface and Coatings Technology* **203**, 2041 – 2045 (2009).

[331] Ye, C., Bando, Y., Shen, G., and Golberg, D. *The Journal of Physical Chemistry B* **110**, 15146–15151 (2006).

[332] Willmott, P. R. and Huber, J. R. *Reviews of Modern Physics* **72**, 315–328 (2000).

[333] Chrisey, D. B., Pique, A., McGill, R. A., Horwitz, J. S., Ringeisen, B. R., Bubb, D. M., and Wu, P. K. *Chemical Reviews* **103**, 553–576 (2003).

[334] Cho, C.-R. and Grishin, A. *Journal of Applied Physics* **87**, 4439–4448 (2000).

[335] Eason, R. *Pulsed laser deposition of thin films: applications-led growth of functional materials*. Wiley-Interscience, (2007).

[336] Chrisey, D. and Hubler, G. *Pulsed laser deposition of thin films*. Wiley-interscience publication. J. Wiley, (1994).

[337] Lorenz, M., Kaidashev, E. M., Rahm, A., Nobis, T., Lenzner, J., Wagner, G., Spemann, D., Hochmuth, H., and Grundmann, M. *Applied Physics Letters* **86**, 143113 (2005).

[338] Zheng, H., Wang, J., Lofland, S. E., Ma, Z., Mohaddes-Ardabili, L., Zhao, T., Salamanca-Riba, L., Shinde, S. R., Ogale, S. B., Bai, F., Viehland, D., Jia, Y., Schlom, D. G., Wuttig, M., Roytburd, A., and Ramesh, R. *Science* **303**, 661–663 (2004).

[339] Duan, X. and Lieber, C. M. *Journal of the American Chemical Society* **122**, 188–189 (2000).

[340] Marcu, A., Yanagida, T., Nagashima, K., Tanaka, H., and Kawai, T. *Journal of Applied Physics* **102**, 016102 (2007).

[341] Yu, D. P., Sun, X. S., Lee, C. S., Bello, I., Lee, S. T., Gu, H. D., Leung, K. M., Zhou, G. W., Dong, Z. F., and Zhang, Z. *Applied Physics Letters* **22**, 1966–1968 (1998).

[342] Tien, L., Pearton, S., Norton, D., and Ren, F. *Journal of Materials Science* **43**, 6925–6932 (2008).

[343] Nagashima, K., Yanagida, T., Tanaka, H., and Kawai, T. *Journal of Applied Physics* **101**, 124304 (2007).

[344] Ohnishi, T., Koinuma, H., and Lippmaa, M. *Applied Surface Science* **252**, 2466–2471 (2006).

[345] Abdelli-Messaci, S., Kerdja, T., Lafane, S., and Malek, S. *Spectrochimica Acta Part B: Atomic Spectroscopy* **64**, 968 – 973 (2009).

[346] Leuchtner, R. E. *Applied Surface Science* **127-129**, 626–632 (1998).

[347] Acquaviva, S., D'Anna, E., and De Giorgi, M. L. *Journal of Applied Physics* **102**, 073109 (2007).

[348] Aubriet, F., Chaoui, N., Chety, R., Maunit, B., Millon, E., and Muller, J.-F. *Applied Surface Science* **186**, 282–287 (2002).

[349] Greer, J. *Large-Area Commercial Pulsed Laser Deposition*, 191–213. John Wiley & Sons, Inc. (2006).

[350] Goodhew, P., Humphreys, F., and Beanland, R. *Electron Microscopy and Analysis*. Taylor & Francis, (2001).

[351] Fultz, B. and Howe, J. *Transmission Electron Microscopy and Diffractometry of Materials*. Springer, (2008).

[352] Williams, D. and Carter, C. *Transmission Electron Microscopy: A Textbook for Materials Science*. Number Parts I - IV. Springer, (2009).

[353] Braga, P. and Ricci, D. *Atomic Force Microscopy: Biomedical Methods and Applications*. Methods in Molecular Biology. Humana Press, (2004).

[354] Eaton, P. and West, P. *Atomic Force Microscopy*. Oxford University Press, (2010).

[355] Giessibl, F. J. *Reviews of Modern Physics* **75**, 949–983 (2003).

[356] Bragg, W. H. and Bragg, W. L. *Proceedings of the Royal Society of London. Series A* **88**, 428–438 (1913).

[357] Birkholz, D. M. *Thin Film Analysis by X-Ray Scattering*. IHP Microelectronics GmbH, Im Technologiepark 25, 15236 Frankfurt (Oder), Germany, (2006).

[358] Yu, P. and Cardona, M. *Fundamentals of Semiconductors: Physics and Materials Properties*. Graduate Texts in Physics. Springer, (2010).

[359] van der Pauw, L. J. *Philips Research Reports* **13**, 1–9 (1958).

[360] Tompkins, H. and Irene, E. *Handbook of Ellipsometry*. William Andrew Pub., (2005).

[361] Fujiwara, H. *Spectroscopic Ellipsometry: Principles and Applications*. John Wiley & Sons, (2007).

[362] Hecht, E. *Optics*. Addison Wesley Longman, Inc. USA, 3rd edition, (1998).

[363] Klingshirn, C. *Semiconductor Optics*. Advanced texts in physics. Springer, (2006).